Towards the Accurate and Efficient Description of Excited States

Bo Peng

A dissertation submitted in partial fulfillment of
the requirements for the degree of

Doctor of Philosophy

University of Washington

2016

Reading Committee:

Xiaosong Li, Chair

Frantisek Tureček

David Masiello

Stefan Stoll

Program Authorized to Offer Degree:
Department of Chemistry

University of Washington

Abstract

Towards the Accurate and Efficient Description of Excited States

Bo Peng

Chair of the Supervisory Committee:
Professor Xiaosong Li
Department of Chemistry

The microscopic and molecular-level characterization and understanding of excited states properties and dynamics plays an important role in modern scientific research. Tremendous examples can be found in photovoltaics, photocatalysis, spintronics, and plasmonics. Over the past several decades, despite the fact that a significant progress has been achieved in the development of experimental techniques (*e.g.* crystallography and spectroscopy), it is important to realize that many chemical transformations, especially when associated with excited states, are still difficult to be precisely detected and accurately characterized in experiments. One typical example is optically forbidden (dark) states, which are experimentally barely accessible, but very often determine the excited state dynamics. Fortunately, quantum chemical calculations of such excited states are usually able to provide accurate and predictive information, and do indeed contribute to the fundamental understanding of excited state properties and dynamics.

To describe excited states properly with quantum mechanics, essentially, one needs to adopt a quantum chemical method that is able to describe electron correlations towards "chemical accuracy" (1 kcal/mol). Among all available quantum chemical methods, the density functional theory/time-dependent density functional theory (DFT/TDDFT) are extremely popular. Their favorable trade-off between accuracy and computational cost has made them standard technique in most branches of chemistry and materials science. How-

ever, DFT/TDDFT results depend on the specific exchange-correlation (XC) functional adopted. The wave-function-based *ab initio* methods, on the other hand, can be systematically improved to provide reliable results. A typical example is the coupled-cluster (CC) model, in which various correlation effects can be categorized according to the rank of excitations included in the approximate form of the cluster and excitation operators, and its accuracy can then be systematically improved by including higher excitations explicitly or perturbatively. In particular, the CC model with single and double excitations corrected by perturbative triples, *a.k.a.* CCSD(T), has been recognized as the "gold standard" for computational chemistry. However, these wave-function-based methods always suffer from very high computational cost (*e.g.* the canonical procedure of CCSD(T) scales as $\mathcal{O}(N^7)$ with N the number of basis functions representing system size), which precludes them from being applied to large systems.

The main objective of this work is to develop quantum chemical methods that provide better trade-off between accuracy and efficiency for the description of electron correlations in some electron excitation scenarios where conventional methods may encounter problems. Several newly developed approximations and algorithms based on DFT, TDDFT, and CC will be presented in the following chapters. The applications of these methods include the computations of excitation energy, excited state wave function, and excited state dynamics. The structure of this thesis is as follows.

- In Chapter 1, the theoretical background of quantum chemical methods for the study of excited states is given. The emphasis is on DFT, TDDFT and CC.

- Chapter 2 describes a guided self-consistent-field (SCF) method developed in this work. The working procedure of this method is presented within DFT framework. The application of this method to the computation of the *d*-*d* transition energies in some metal complexes is discussed.

- In Chapter 3, a factorization method is introduced to deal with states coupling driven by pure electron-electron interaction. In combination with DFT and TDDFT technique, its application in estimating the transition rate of a spin-fliped Auger process in large CdSe quantum dots is discussed.

- Chapter 4 discusses the real-time TDDFT method. The case study is focusing on the exciton dynamics in a two-silver-atomic-chain prototype system that goes beyond the capability of canonical models of electronic energy transfer.

- In Chapter 5, a variant of the equation-of-motion CC (EOM-CC) method aiming at solving interior eigenpairs of the EOM Hamiltonian matrix is discussed. A benchmark of this method is done by computing the K-edge core excitation energies of carbon, oxygen, nitrogen, and sulfur in some molecules.

TABLE OF CONTENTS

Page

LIST OF FIGURES

ABBREVIATIONS

AO: Atomic Orbitals

ALDA: Adiabatic Local Density Approximation

CASSCF: Complete Active Space SCF

CASPT2: Complete Active Space Perturbation Theory of Second Order

CC: Coupled-Cluster

CC2: Second-Order Approximation to the CC Model with Singles and Doubles

CCSD: CC Model with Singles and Doubles

CCSD(T): CC Model with Singles and Doubles Corrected by Perturbative Triples

CI: Configuration Interaction

CIS: Configuration Interaction Singles

CPP-CC: Complex Polarization Propagator Formulation of CC Response Theory

DBT: Dibenzothiophene

DFT: Density Functional Theory

DOS: Density of States

EA-EOM-CCSD: Electron-Attachment EOM-CCSD

EOM: Equation-of-Motion

EOM-MBPT2: Equation-of-Motion Second-Order Many-Body Perturbation Theory

EOM-MRCCSD: Equation-of-Motion Multi-Reference CC

ES: Energy-Specific

HF: Hartree-Fock

KS: Kohn-Sham

LR: Linear-Response

MCSCF: Multi-Configurational Self-Consistent Field

MO: Molecular Orbitals

MMUT: Modified Midpoint Unitary Transform

MR-CI: Multi-Reference Configuration Interaction

NTO: Natural Transition Orbital

REW: Restricted Excitation Window

P-EOM-MBPT2: Partitioned EOM-MBPT2

QD: Quantum Dot

RT: Real-Time

SCF: Self-Consistent Field

TDDFT: Time-Dependent Density Functional Theory

TDHF: Time-Dependent Hartree-Fock

TM: Transition Metal

XC: Exchange-Correlation

ACKNOWLEDGMENTS

I wish to express sincere appreciation to University of Washington, where I have had the opportunity to work with all the friends from the Li group.

My special appreciation goes to Prof. Xiaosong Li, who offered me a position in this group five years ago, and provided opportunities and support for me to pursue a systematic study in the area of electronic structure theory. He generously provided me a lot of guides no matter in research or in life. Only with his help has this work been done. Also, I want to give my special thanks to Prof. Frantisek Tureček for generously providing me the collaboration opportunities to work with him. I was deeply impressed by his enthusiasm in the scientific research. Besides, I want to acknowledge the following,

- Feizhi Ding and Phu Nguyen for not only reliable colleagues, but faithful friends.
- Patrick Lestrange, Joshua Goings, David Williams-Young, David Lingerfelt, and Erica Chong for fruitful discussion and kind help no matter when I am writing a paper or preparing for an interview.
- Hongbin Liu and Shichao Sun for nice discussions about science and life.
- All the committee member for the patience and the time they spent on reading through this thesis.

Finally, I would like to give my best thanks to my parents and my girlfriend for the deepest love they gave me that enriches my life.

Chapter 1

OVERVIEW

> ⋯ ***within the orbital picture, the correlated motion of interacting electrons manifests itself in virtual excitations of electrons from occupied to unoccupied spin orbitals***. ⋯
>
> – T. Helgaker et al. in *Molecular Electronic Structure Theory*[100]

1.1 Electron Correlation and Excited Electronic State

The motions of the electrons are correlated. For example, one can not find two electrons at the same points in space with parallel spins. This type of correlation is often called Fermi correlation, which is already included in the Hartree-Fock (HF) method of quantum chemistry. Beside the Fermi correlation, there are many other modes of electron correlation usually discussed in the description of electronic systems. For example, the so-called static correlation is usually discussed when a single reference determinant is not able to give a good description of an electronic configuration due to the near-degeneracy of electronic configurations. In this scenario, multi-configuration self-consistent field (MCSCF) theory can be employed.[154] On the other hand, dynamic correlation is often introduced when the description of the instantaneous correlation of electron motion arising from the electron repulsion is required. Dynamic electron correlation is known to play a key role in quantitative description of reaction barrier heights and excitation energies, and can be best accounted for by perturbation theory[162, 16] or CC theory.[77, 39] The dynamic correlation can be further categorized into long-range dynamic correlation and short-range dynamic correlation. The former is responsible for the description of dispersion forces in van der Waals interactions, while the latter is related to the Coulomb cusp in the electronic wave function, and can be treated using explicitly correlated method.[119]

Electronically excited states often display large electron correlation effects. Proper consideration of electron correlation effect in the description of excited state is as important, if not more important, than that in ground state. Inability to properly account for these effect will lead to a large deviation between calculated and experimental excitation energies for some valence excited singlet and triplet states. Typical examples are the $^1(\pi, \pi^*)$ state in ethene[152] and the E_{1u} state in benzene.[150, 183] Besides, since the dynamic correlation effect on Rydberg state is much smaller than that on some valence excited states, inability to properly account for the dynamic correlation effect may give rise to a too strong interaction between the valence state and a Rydberg state. The too strong valence-Rydberg interaction will make the valence state, and thus the electron density, too diffuse, and will bring a significant error. It has been shown that the resulting error in excitation energy for ethene and ^1B_u states in butadiene could be of the order of 0.3 eV.[190]

As mentioned above, there are several ways to properly account for the electron correlation during the excited state calculation. However, typical wave-function-based methods, such as configuration interaction (CI),[218, 226] multireference CI (MR-CI)[35, 169] or multireference Møller-Plesset,[151, 113] MCSCF,[154] complete active space SCF (CASSCF)[182] and complete active space perturbation theory of second order (CASPT2),[4] though providing very accurate results, are nevertheless too computationally expensive for molecules of medium to large size. Therefore, in terms of developing methods towards accurate and efficient description of excited states, the effort is usually on the density functional theory/time-dependent density functional theory and coupled-cluster theory. The following sections will give a brief overview of these theories.

1.2 Density Functional Theory (DFT) and Time-dependent Density Functional Theory (TDDFT)

DFT is a formally exact theory. The famous *Hohenberg-Kohn* theorems[105] ensure a one-to-one mapping between the electron density and the external potential, and guarantee the variational principle for the electron density. The electron correlation is included in the DFT through the so-called exchange-correlation (XC) functional. Since the exact XC functional is unknown, all the XC functionals used in practice are approximate XC functionals, which are fitted based on model systems such as the uniform electron gas and other known properties. Thus, the accuracy of a DFT calculation is closely related to the quality of the approximate XC functional for the system under investigation. As a single-particle theory, DFT usually aims at the precise calculation of the electronic ground state of molecules. Nevertheless, DFT can be applied for the calculation of some particular electronically excited state if some constraints are introduced during the SCF iteration to force the procedure to converge to an energetically higher solution. However, if the excited state has the same spin multiplicity or same irreducible representation of the spatial symmetry group as the ground state, as usually found in the optical spectra of large molecules, this method will break down (as will be discussed in Ch. 2). More often, the TDDFT[184] is used for the calculation of excited state of molecules of medium to large size. In analogy to Kohn-Sham (KS) DFT,[118] TDDFT is done in the time-dependent KS formalism,

$$i\frac{\partial}{\partial t}\phi_i(r,t) = \underbrace{\left(-\frac{1}{2}\nabla_i^2 + v(r,t) + \int \mathbf{d}^3r' \frac{\rho(r',t)}{|r-r'|} + \frac{\delta A_{xc}[\rho]}{\delta\rho(r,t)}\right)}_{\mathbf{F}_t^{KS}} \phi_i(r,t) \tag{1.1}$$

in which, each electron, being represented by the single-electron orbitals $\phi_i(r,t)$, is treated individually in the mean field of all others, and the election density is given as

$$\rho(r,t) = \sum_i^{N_{elec}} |\phi_i(r,t)|^2. \tag{1.2}$$

If expanding the single-electron orbitals in a manifold represented by N_{bas} basis functions, $\{\chi_1(r), \cdots, \chi_i(r), \cdots, \chi_{N_{bas}}(r)\}$,

$$\phi_i(r,t) = \sum_\mu^{N_{bas}} c_{i\mu}(t)\chi_\mu(r), \tag{1.3}$$

then the time-dependent KS equation can be expressed in a matrix form,

$$i\frac{\partial}{\partial t}\mathbf{c}_t = \mathbf{F}_t^{KS}\mathbf{c}_t, \tag{1.4}$$

where the subscript indicates the time-dependent feature. Employing the time-dependent density matrix $\mathbf{P}$, as defined by

$$P_{\mu\nu}(t) = \sum_{i}^{N_{occ}} c_{i\mu}(t) c_{i\nu}(t), \tag{1.5}$$

eventually one can reach the Dirac form of the time-dependent KS equation

$$i\frac{\partial}{\partial t}\mathbf{P}_t = [\mathbf{F}_t^{KS}, \mathbf{P}_t]. \tag{1.6}$$

Numerically, there are two different schemes to solve Eq. (1.6). The widely used scheme focuses on the linear response (LR) of the electron density to a perturbation.[41, 42] Given that electronic transitions occur for an infinitesimal perturbation, and employing the canonical orbitals, the LR-TDDFT scheme essentially deals with a non-Hermitian eigenvalue problem,

$$\begin{bmatrix} \mathbf{A} & \mathbf{B} \\ -\mathbf{B}^* & -\mathbf{A}^* \end{bmatrix} \begin{bmatrix} \mathbf{X} \\ \mathbf{Y} \end{bmatrix} = \omega \begin{bmatrix} \mathbf{X} \\ \mathbf{Y} \end{bmatrix}. \tag{1.7}$$

Here, ω denotes the transition energy, and $\mathbf{X}$ and $\mathbf{Y}$ are excitation and de-excitation operators. The elements of matrices $\mathbf{A}$ and $\mathbf{B}$ are given in Mulliken notation as

$$A_{ia,jb} = \delta_{ij}\delta_{ab}(\epsilon_a - \epsilon_i) + (ia|jb) + (ia|f_{xc}|jb), \tag{1.8}$$

$$B_{ia,jb} = (ia|bj) + (ia|f_{xc}|bj). \tag{1.9}$$

Since the exact time-dependent XC action functional ($A_{xc}[\rho]$) is not known, and supposed the electron density varies slowly with time, people then introduce the so-called adiabatic local density approximation (ALDA)[171] to use a standard local ground-state XC potential to compute $(ia|f_{xc}|jb)$ term in Eq. (1.8) and Eq. (1.9),

$$(ia|f_{xc}|jb) = \int \mathrm{d}^3r\, \mathrm{d}^3r'\, \phi_i^*(r)\phi_a(r)\frac{\delta^2 E_{xc}}{\delta\rho(r)\delta\rho(r')}\phi_j^*(r')\phi_b(r'). \tag{1.10}$$

Alternatively, one can directly propagate the time-dependent density matrix in time. This is often referred to as real-time (RT) TDDFT.[233, 148, 138, 134, 106] Standard technique can be used to numerically integrate Eq. (1.6) as long as the density matrix remains idempotent,

$\mathbf{PP} = \mathbf{P}$ (due to the constraint that MO's must remain orthonormal). One numerical propagation method will be briefly discussed in Ch. 3 and Appendix C. It is worth pointing out that, for small perturbations to the ground-state density, both LR-TDDFT and RT-TDDFT schemes are able to describe single-electron excitations from the ground state using the standard approximate ground state XC functional. If many transitions are required to model an absorption spectrum, RT-TDDFT can be more computationally affordable, since it gives the full spectrum via a single Fourier transform of the time-dependent dipole moment. More importantly, RT-TDDFT enables direct modeling of the excited state dynamics.

1.3 Coupled-Cluster (CC) Theory

In CC theory,[54, 192] the correlated motion of the electrons (within the orbital model) is taken into account by including the excitations of electrons within the clusters of different sizes. This is done by first introducing the cluster operator, which is defined in Eq. (1.11).

$$T = \sum_{\mu>0} t_\mu \tau_\mu = \sum_{\mu>0} T_\mu. \tag{1.11}$$

Here, τ_μ is the excitation operator, which can generate a substituted determinant $|\mu\rangle$ when acting on the reference determinant $|0\rangle$. Within each excitation, there is also an amplitude t_μ, representing the probability that this particular excitation will occur as a result of electron interaction. Then, the cluster operator is applied to the reference state to generate a correlated wave function. This process can be simplified via an exponential ansatz, since

$$|CC\rangle = \left[\pi_{\mu>0}(1 + T_\mu)\right]|0\rangle = \left[\pi_{\mu>0} e^{T_\mu}\right]|0\rangle = e^{\sum_{\mu>0} T_\mu}|0\rangle = e^{T}|0\rangle. \tag{1.12}$$

Note that $(T_\mu)^n|0\rangle = 0$ for $n \geq 2$. Also, since the substituted determinnant $|\mu\rangle$ is orthogonal to $|0\rangle$, it is easy to see that $\langle 0|CC\rangle = 1$, which is usually known as the intermediate normalization. Plugging the correlated wave function into the Schrödinger equation, applying the intermediate normalization, and left-projecting against the reference state, the CC energy and amplitudes can then be obtained,

$$\langle 0|H|CC\rangle = E_{cc}, \tag{1.13}$$

$$\langle \mu|H|CC\rangle = E_{cc}\langle \mu|e^{T}|0\rangle. \tag{1.14}$$

Usually, it is more convenient to express the projected CC equations in a slightly different form,

$$\langle 0|e^{-T}H|CC\rangle = \langle 0|e^{-T}He^{T}|0\rangle = E_{cc}, \tag{1.15}$$

$$\langle \mu|e^{-T}H|CC\rangle = \langle \mu|e^{-T}He^{T}|0\rangle = E_{cc}\langle \mu|e^{-T}e^{T}|0\rangle = 0. \tag{1.16}$$

where the Hamiltonian can be viewed as being similarity transformed with the T operator. Apparently, the similarity transformation leaves the energy unchanged, and yields a “neat” expression for the amplitudes.

Eq. (1.16) is usually referred to as the linked CC equation, which is superior to its unlinked analog (Eq. (1.14)) in many situations. Firstly, the linked equation simplifies the algebra of the expansion. Note that the similarity-transformed Hamiltonian can be expanded by the *Baker-Campbell-Hausdorff* expansion

$$e^{-T}He^{T} = H + [H,T] + \frac{1}{2}[[H,T],T] + \frac{1}{6}[[[H,T],T],T] + \frac{1}{24}[[[[H,T],T],T],T], \tag{1.17}$$

which naturally terminates at the fourth term since the Hamiltonian can at most be linked to four cluster operators, and all higher-order terms will contain commutators of only the cluster operators, and are therefore zero. Also, the linked equation is size-extensive term by term, and allows for a simpler control of size-extensivity upon the modification of the CC equation. Besides, the linked equations serves a starting point for the development of a CC approach for the calculation of excited states. For example, in the equation-of-motion CC (EOM-CC) model,[198, 51] the excited state can be calculated by a linear expansion in the space spanned by all states of the form

$$|\mathbf{r}\rangle = \sum_{\mu} r_{\mu}\tau_{\mu}|0\rangle. \tag{1.18}$$

The expansion parameters, which carry the excitation structure, are optimized by minimizing the energy

$$E(\mathbf{l},\mathbf{r}) = \frac{\langle \mathbf{l}|e^{-T}He^{T}|\mathbf{r}\rangle}{\langle \mathbf{l}|\mathbf{r}\rangle}. \tag{1.19}$$

Here, the similarity-transformed Hamiltonian carries the information about the correlated motion of electrons, and can significantly simplify the associated algebra (as can be seen in Ch. 5).

Chapter 2

A GUIDED SELF-CONSISTENT-FIELD (SCF) METHOD FOR EXCITED-STATE WAVE FUNCTION OPTIMIZATION

A guided SCF method is presented in this chapter. This method uses the eigenspace update-and-following idea to guide the occupation of molecular orbitals to improve the SCF method for optimizing wave functions that are higher-energy solutions to the Roothaan-Hall equations. The initial guess of excited wave function is improved with a pre-conditioning step. For testing, the guided SCF method is used to optimize ligand-field excited states of transition metal complexes, and calculate transition metal *d*-*d* transition energies. The results are compared with those obtained from orbital energy differences, LR-TDDFT, and experiments.

2.1 Introduction

Theoretical investigations of electronic excitations often require searching for excited-state wave functions while maintaining the orthogonality constraint. When wave function approximations (*e.g.* the finite basis approximation) are used, variational methods (*e.g.* the CI), can be used to obtain the upper bound of each excited state, fulfilling the bracketing theorem.[142] However, correlated electronic structure methods that satisfy both the orthogonality constraint and the bracketing theorem are of prohibitive computational cost except for systems with only a few electrons. Practical applications of excited-state calculations often use methods that avoid explicit computations of excited-state wave functions. For example, LR-TDDFT has been the workhorse for obtaining excitation energies at a very affordable computation cost.[87, 168, 40, 41, 206, 62, 42, 135] LR-TDDFT computes the first-order response of ground-state electronic density to a small external perturbation. As a result, excitation energies are obtained as the resonant frequencies of the system. This approach is computationally inexpensive because calculations of explicit excited-state wave functions are avoided.

In cases where excited-state wave functions are needed for analyzing molecular properties, the ΔSCF method[91, 110, 101, 85, 25, 78] can be used to obtain the approximate wave function of excited state. This method is based on the proof (under some assumptions) that there exist some higher-energy solutions to the Roothaan-Hall equation.[137, 201] However, these solutions do not satisfy the bracketing theorem. As a result, they are just some stationary upper bounds of the ground state. Nevertheless, with careful scrutiny of the electronic characteristics of the higher-energy solutions, the electronic excitation energies can be approximated as the difference between the ground state and the SCF-converged higher-energy states. When these two wave functions are associated with different spin-manifolds (*e.g.* singlet and triplet), this technique is rather successful in predicting the spectra and electronic transition characteristics. When the excited state of interest has the same spin symmetry as the ground state (*e.g.* S_1 vs. S_0), the excited state is approximated as a broken-spin-symmetry configuration state converged self-consistently to a higher energy solution of the Roothaan-Hall equation. However, the approximate excited state often does not satisfy the orthogonality constraint. Although the lack of constraint of orthogonality to the ground state only leads to errors in the second-order term in the wave function,[100] it gives rise to convergence difficulty.[235] Conventional SCF techniques often lead to the variational collapse to the ground state even if appropriate initial guesses of orbital occupations are used.

For electronic excitations of transition metals in ligand fields, standard ΔSCF often fails due to small energy differences between SCF solutions and the high degeneracy of *d*-orbitals. In such cases, one needs to include a constraint or guidance during the SCF procedure. Recently, controlled SCF methods using the maximum overlap approach have been used to converge the SCF procedure to charge-transfer and core-excited states.[78, 28] Inspired by the success of controlled SCF methods for optimizing excited-state wave functions, I proposed to use an eigenspace update-and-following method[133] to guide the SCF convergence to a higher-energy solution as an approximation to the excited state. The detailed discussion about the method and its robustness are presented in the Methodology section. I also apply the guided SCF method to study *d-d* transitions in a select set of transition metal complexes and compare these results with experimental values.

2.2 Methodology

Optimization of single-particle wave functions as in HF and KS DFT can be achieved by iteratively solving the Roothaan-Hall equation in the atomic orbital (AO) basis,

$$\mathbf{FC} = \mathbf{SC}\epsilon, \tag{2.1}$$

where $\mathbf{F}$, $\mathbf{C}$, $\mathbf{S}$, and ϵ are the Fock/KS matrix, molecular orbital coefficients, overlap matrix and orbital energies, respectively. For unrestricted HF and DFT, Eq. (2.1) is solved separately for α and β spins, with each of the Fock matrices constructed based on density matrices of both spins. In a conventional optimization of the ground-state wave function of an N-electron system, the N spin-orbitals $\{\phi_i\}$ with the lowest energies are chosen to be occupied as an initial guess, while the rest of orbitals are unoccupied. The Slater determinant of such wave function can be specified by an occupation number vector, $|\mathbf{n}\rangle$, such as

$$|\mathbf{n}\rangle = |1_1, 1_2, ..., 1_N, 0_{N+1}, ..., 0_K\rangle, \tag{2.2}$$

where the subscript denotes the orbital and K is the basis size. Any permutation of occupation numbers between occupied and unoccupied orbitals results in an excited configuration state, which can be used as the initial guess for the excited-state wave function. Here, I introduce a pre-conditioning step to the permuted initial guess when the subject of interest is an excited state of the same spin symmetry as the ground state (*e.g.* S_0 and S_1). Considering an initial guess for excited-state wave function is generated by orbital permutation in the α spin-manifold (*e.g.* $|\mathbf{n}\rangle_\alpha = |1_1, 1_2, ..., 0_N, 1_{N+1}, ..., 0_K\rangle_\alpha$) while the β spin remains in its ground state configuration (*e.g.* $|\mathbf{n}\rangle_\beta = |1_1, 1_2, ..., 1_N, 0_{N+1}, ..., 0_K\rangle_\beta$). The pre-conditioning step is essentially an SCF iteration applied to the β manifold only. In this step, the Fock/KS matrix corresponding to the β spin is fully diagonalized while maintaining the α spin intact. The β spin wave function is reconstructed using the pre-conditioned eigenvectors of the β Fock/KS matrix. The purpose of this pre-conditioning step is obvious. It introduces a better Coulombic potential for optimization of the permuted spin-manifold, the α spin in this example. In the presented test cases, this simple pre-conditioning step gives rise to more stable SCF convergence using the algorithm presented next.

In order to maintain the desired orbital occupation arrangement during the SCF procedure, I have implemented a guided-SCF method that combines the pre-diagonalization step and eigenspace update techniques. The algorithm is constructed in an orthonormal basis. Transformation from AO (unprimed notation, *e.g.* $\mathbf{F}$ and $\mathbf{C}$) to orthonormal basis (primed notation, *e.g.* $\mathbf{F}'$ and $\mathbf{C}'$) can be achieved using the Löwdin or the Cholesky method.[160, 130, 132] The details of this algorithm are presented in the following paragraphs.

In the i-th SCF iteration, the Fock/KS matrix $\mathbf{F}'_i$ is formed using the occupied set of MOs from the previous iteration $\mathbf{C}'_{i-1}$. Note that $\mathbf{C}'_0$ corresponds to the initial guess of excited configuration state. Then a guidance vector $\mathbf{G}_{i-1}$ is introduced with $\mathbf{G}_0 = \mathbf{C}'_0$ to pre-diagonalize the Fock/KS matrix,

$$\Delta_i = \mathbf{G}^\dagger_{i-1}\mathbf{F}'_i\mathbf{G}_{i-1} \tag{2.3}$$

The purpose of this intermediate pre-diagonalization step is to construct a diagonally dominant form of the Fock/KS matrix. The transformed Fock/KS matrix is then diagonalized by a standard eigensolver yielding the eigenvalues and eigenvectors of the intermediate matrix.

$$\epsilon_i = \mathbf{A}^\dagger_i\Delta_i\mathbf{A}_i \tag{2.4}$$

The guidance vector for the permutation of the eigenvectors of the Fock/KS matrix at the i-th iteration are then computed using the following equation,

$$\mathbf{G}_i = \mathbf{G}_{i-1}\mathbf{A}_i. \tag{2.5}$$

In terms of computational cost, this approach is advantageous in most cases since the diagonalization of a diagonal-dominant matrix (Eq. (2.4)) is less expensive than direct diagonalization of a dense matrix, $\mathbf{F'}_i$. In the context of the guided SCF method developed here, the pre-diagonalization step is used to project the current Fock/KS matrix to the guided vector space, preserving the ordering of orbital occupations. This step gives the guidance to the SCF procedure by maintaining the orbital occupations. In other words, instead of selecting the N lowest energy spin-orbitals resulting from a direct diagonalization, the SCF proceeds by inheriting the orbital occupation arrangement from the guidance vectors.

The guided SCF algorithm discussed above is implemented in the development version of the Gaussian program.[74] For all test cases, geometry optimizations were fully optimized with the T_d symmetry constraint. The metal d-orbitals are identified by population analysis and visual inspection. Initial excited configurational states are constructed by interchanging the occupation numbers of occupied and virtual orbitals, followed by wave function optimization using the guided SCF approach introduced here.

2.3 *Application to d-d Transitions in Transition-Metal Complexes*

One of the most important theories for understanding physical properties of transition metal (TM) complexes is ligand field theory. It has been successfully and widely used in the interpretation of optical, spin, and magnetic measurements of TM complexes. For ligand field theory of octahedral and tetrahedral coordinations, the central parameter describing the metal–ligand environment is the ligand field splitting energy, 10Dq, which can be readily observed in the $d-d$ spectra of TM complexes. Due to rather small excitation energies and high degeneracy of d-levels, ligand-field transitions are usually difficult to resolve. In this work, I apply the method introduced above to calculate ligand-field excitations in a select set of tetrahedral TM complexes. The first test case is $[Co(II)Cl_4]^{2-}$ (Fig. 2.1), which has been the subject of extensive experimental and theoretical studies.[129, 108, 102, 197, 43, 166, 145] The tetrahedral ligand field splits d levels into two e orbitals and three t_2 orbitals ($\epsilon_e < \epsilon_{t_2}$). $[Co(II)Cl_4]^{2-}$ is a typical high-spin complex with a ${}^4A_2(F)$ ground state and an $e^4T_2^3$ electron

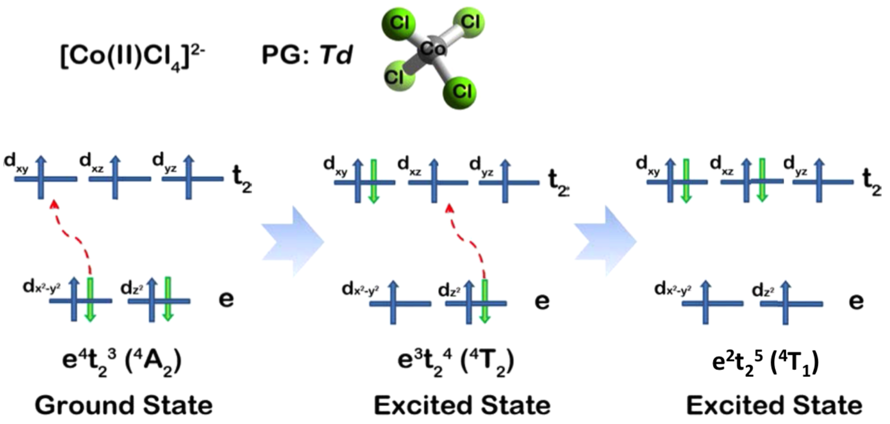

Figure 2.1: Schematic description of the electronic structure of the ground and excited states of $[Co(II)Cl_4]^{2-}$ in the T_d ligand field.

configuration. The lowest spin-allowed $d-d$ transition corresponds to the $^4A_2(F) \rightarrow {}^4T_2(F)$ (Fig. 2.1) excitation. In order to obtain the energy and wave function of the $^4T_2$ state, the initial guess of excited state is prepared by promoting an electron from the occupied $d_{x^2-y^2}$ to the unoccupied d_{xy} spin orbitals in the β manifold at the ground state geometry (*i.e.* vertical excitation). Fig. 2.2 shows the KS orbitals whose populations are manipulated to generate the $d-d$ excited states. The guided SCF method is then used to optimize the wave function of the $^4T_2(F)$ state. The energy difference between the fully optimized $^4T_2(F)$ and $^4A_2(F)$ states is the 10Dq value (*d*-*d* transition energy).

Table 2.1 compares experiments with the computed 10Dq values using the guided SCF method with various DFT functionals. I also include estimated 10Dq values using simple or-

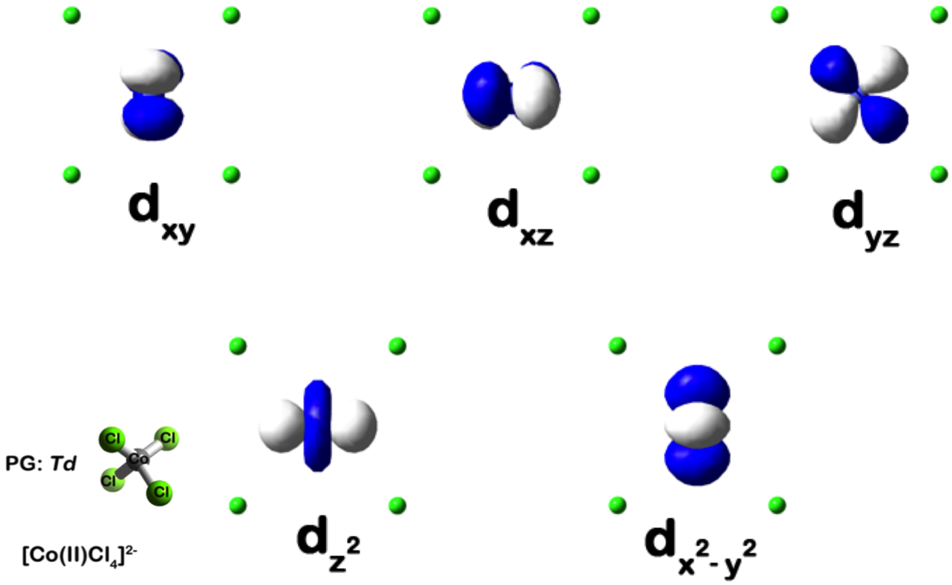

Figure 2.2: Frontier spin orbitals of $[\mathrm{Co(II)Cl_4}]^{2-}$ in the T_d ligand field.

bital energy differences, and those computed by the LR-TDDFT method. I have tested functionals at several different levels of approximation including GGA (BLYP[22, 127] and BP86), meta-GGA (TPSS[210]), hybrid GGA (B3LYP[204] and B97-2[229]), and meta hybrid GGA (TPSSh[202]) with pseudo-potential LANL2DZ,[95, 96, 220] and several full-electron basis sets. The diversity of this test set is representative of the most commonly used DFT functionals for studies of ligand field excitations. These tests assess the consistency of each method for calculating ligand field excitation energies. Table 2.1 shows that the calculated $t_2 - e$ orbital energy difference (0.01$\sim$0.07 eV) severely underestimate the experimentally determined 10Dq value ($\sim$0.39 eV) as expected. On the other hand, the LR-TDDFT results overestimate the excitation energy by about 0.25 eV. The nature of the LR theory describes one-electron excitation in the ground state electronic potential. It does not include wave function relaxation/optimization of the excited state. As a result, the LR-TDDFT method computes an upper bound of the excitation energy associated with local electronic transitions. Similar overestimation of $d - d$ transitions using LR-TDDFT has been reported for Co(III) and Rh(III) complexes.[55] In contrast, the ΔSCF results using the guided SCF method are in excellent agreement with the experimental 10Dq values.

In principle, the guided SCF technique for computing excited states and excitation energies is not restricted to single-electron excitation. I have also applied the guided SCF algorithm to calculate the wave function and excitation energy of the doubly excited state, ^{4}T$_1$(F). The procedure is similar to that for the ^{4}T$_2$(F) singly-excited state. Beginning with the ^{4}T$_2$(F) singly-excited state, a second β electron is promoted from the d_{z^2} orbital to an unoccupied orbital in the t_2 set and this state is optimized. The excitation energy for the doubly-excited state is given in Tab. 2.1. The ability of the guided SCF algorithm to isolate a state that is doubly-excited with respect to the ground state reference, exhibits an advantage of ΔSCF techniques over LR-TDDFT from which double excitations cannot be obtained. The guided SCF method can be used as a computationally inexpensive approach for optimizing doubly-excited electronic states.

Table 2.2 lists 10Dq values in various transition metal complexes in tetrahedral coordination computed at the BP86/LANL2DZ level of theory. The 10Dq values from the ΔSCF using the guided SCF method, LR-TDDFT, and experiment (where available) are compared. For all test cases, ΔSCF excitation energies are in very good agreement with experiment. For most of the cases, the deviation of the guided SCF method result from the experimental value is less than 0.1 eV, whereas the LR calculations overestimate the 10Dq values significantly.

2.4 Summary

In this chapter, I introduced a guided SCF method for obtaining higher energy solutions to the Roothaan-Hall equation as approximations to the excited states. This method uses the idea of eigenspace update-and-following to maintain the orbital occupations chosen in the initial guess while allowing the wave function to be fully optimized. A pre-conditioning

Table 2.1: Comparison of ligand field excitations in $[Co(II)Cl_4]^{2-}$. The experimental 10Dq ($^4A_2 \rightarrow\ ^4T_2(F)$) value is about 0.39 eV.[166] Two-electron $d-d$ transition $^4A_2 \rightarrow\ ^4T_1(F)$ is observed at 0.83 ± 0.16 eV.[86, 223]

	$\epsilon_{t_2} - \epsilon_e$	LR-TDDFT	ΔSCF (eV)	
	/eV	/eV	$^4A_2(F) \rightarrow\ ^4T_2(F)$	$^4A_2(F) \rightarrow\ ^4T_1(F)$
B3LYP/LANL2DZ	0.04	0.64	0.32	0.91
BLYP/LANL2DZ	0.01	0.64	0.33	0.87
TPSS/LANL2DZ	0.01	0.65	0.34	1.00
TPSSh/LANL2DZ	0.07	0.65	0.33	1.02
B97-2/LANL2DZ	0.03	0.65	0.33	0.87
BP86/LANL2DZ	0.03	0.65	0.35	0.88
BP86/6-31+G(d)	0.05	0.73	0.40	1.00
BP86/cc-pVDZ	0.00	0.73	0.36	0.96
BP86/aug-cc-pVDZ	0.00	0.73	0.39	1.01

Table 2.2: 10Dq values computed using the guided SCF method for a select set of first row transition metal complexes at the BP86/LANL2DZ level of theory.

	TM 3d Configuration	Spin Multiplicity	LR-TDDFT /eV	ΔSCF ΔE_1/eV	Exp.	Ref.
$[\mathrm{V(III)Cl_4}]^-$	e^2	3	1.57	1.47	1.30	[129]
$\mathrm{V(IV)Cl_4}$	e^1	2	1.57	1.02	1.12	[129]
$[\mathrm{V(II)(H_2O)_6}]^{2+}$	t_{2g}^3	4	1.64	1.19	1.53	[129]
$\mathrm{Cr(IV)F_4}$	e^2	3	2.20	1.34	1.25	[129]
$[\mathrm{Cr(II)Cl_4}]^{2-}$	$e^2t_2^2$	5	1.05	1.03	1.22	[129]
$\mathrm{Mn(IV)F_4}$	$e^2t_2^1$	4	1.58	1.34	1.34	[30]
$[\mathrm{Fe(VI)O_4}]^{2-}$	e^2	1	0.98	0.60	0.57	[211]
$\mathrm{Fe(CO)_4}$	$e^3t_2^3$	5	0.96	0.67		
$[\mathrm{Co(II)I_4}]^{2-}$	$e^4\mathrm{T}_2^3$	4	0.60	0.30	0.33	[129]
$\mathrm{Co(CO)_4}$	$e^4\mathrm{T}_2^3$	4	0.65	0.62		
$[\mathrm{Ni(VI)O_4}]^{2-}$	$e^2t_2^2$	5	0.60	0.77		
$[\mathrm{Ni(II)Cl_4}]^{2-}$	$e^4\mathrm{T}_2^4$	3	0.75	0.35	0.51	[129]
$[\mathrm{Ni(II)(CN)_4}]^{2-}$	$e^4\mathrm{T}_2^4$	3	0.78	0.45		
$\mathrm{Ni(CO)_4}$	$e^4\mathrm{T}_2^4$	3	0.65	0.60		
$[\mathrm{Ni(II)(H_2O)_6}]^{2+}$	$t_{2g}^6e_g^2$	2	1.31	0.81	1.05	[129]
$[\mathrm{Cu(II)(H_2O)_4}]^{2+}$	$e^4\mathrm{T}_2^5$	2	0.59	0.47	0.53	[177]

procedure is introduced to improve the initial guess generated using simple orbital permutation. This method has been applied to studies of ligand-field transitions in tetrahedral transition metal complexes. The results were compared with experiments and other widely used methods. The ΔSCF excitation energies are in excellent agreement with experiments. This is a significant improvement over orbital energy differences and LR-TDDFT, which either significantly underestimate or overestimate excitation energies. Finally, the guided SCF algorithm provides a promising approach for optimizing multi-electron excited states.

Chapter 3

THEORETICAL EVALUATION OF SPIN-DEPENDENT AUGER DE-EXCITATION

A quantitative method for analysis of fast Mn^{2+}-centered Auger processes in Mn^{2+}-doped semiconductors is introduced. Analytical expressions have been derived that describe the Coulomb ("direct") and exchange ("*sp-d*") contributions to Mn^{2+}-electron Auger de-excitation rate constants. All of the quantities in these expressions can be calculated using existing electronic structure methods without the computational expense of multi-reference approaches. Using TDDFT to generate input parameters, these expressions have been applied to calculate Auger de-excitation rate constants in Mn^{2+}-doped CdS nanocrystals. The results of these calculations agree well with experiment. Analysis reveals that the large rate constants for Auger de-excitation in Mn^{2+}-doped semiconductors are primarily attributable to effective *s-d* exchange coupling.

3.1 Introduction

Fast Auger recombination processes are ubiquitous in the photophysics of semiconductor nanocrystals (or quantum dots, QDs). Such processes have been widely examined in relation to quantum dot blinking,[66, 121, 236] multi-exciton decay,[115] and charge-controlled luminescence.[107] Recently,[227] an analogous Auger process was reported in doped semiconductor nanocrystals, in which photoexcited Mn^{2+} impurity ions were de-excited via nonradiative energy transfer to extra conduction-band electrons (e_{CB}), as illustrated in Fig. 3.1. The rate constants measured for this Mn^{2+}-electron Auger process ($\sim 2.5 \times 10^{-10}$ cm^3 s^{-1} for diameter (D) $\sim$ 4.5 nm $Cd_{1-x}Mn_xS$ nanocrystals[227]) are comparable to those measured for exciton-electron (negative trion) Auger recombination in undoped semiconductor nanocrystals (for example, $\sim 1 \times 10^{-10}$ cm^3 s^{-1} for $D \sim 6$ nm CdSe/CdS core/shell nanocrystals[107]), a remarkable result given the extreme localization and spin-forbidden nature of the Mn^{2+} *d*-*d* transition involved in the former process (Fig. 3.1). Such Auger de-excitation has long been known to limit the performance of Mn^{2+}-based thin-film electroluminescent devices made from bulk Mn^{2+}-doped semiconductors[125, 126, 90, 84] and related materials,[50, 38] and understanding its microscopic origins is therefore of both fundamental and practical importance. Whereas theoretical models have been developed to calculate exciton-electron Auger recombination rates in undoped semiconductors,[221, 46, 65] however, to date there have been no first-principles theoretical analyses of Mn^{2+}-electron Auger de-excitation in doped semiconductors, either bulk or quantum confined, largely because of the computational challenges associated with multi-electron, multi-reference, spin-flip processes.

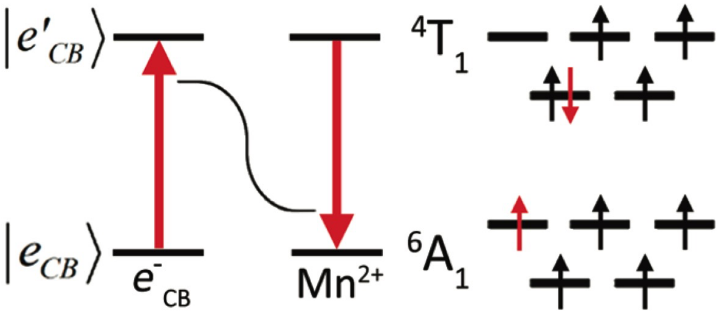

Figure 3.1: **Left**: Schematic depiction of Mn^{2+}-electron Auger de-excitation, in which energy is transferred from Mn^{2+}(^{4}T$_1$) excited state to a conduction-band-edge electron (e_{CB}) to yield a hot conduction-band electron (e'_{CB}) and Mn^{2+} in its ground state (^{6}A$_1$). **Right**: The d^5 configurations of the Mn^{2+} ^{4}T$_1$ and ^{6}A$_1$ states. The ^{4}T$_1$ → ^{6}A$_1$ relaxation involves an electron spin flip, in addition to an orbital transition.

Auger rate constants can be generally described using Fermi's Golden Rule (Eq. (3.1)).[123]

$$k_{\mathrm{Aug}} = \frac{2\pi}{h} \int |\langle \Psi_i | \hat{V}_{if} | \Psi_f \rangle|^2 \delta(E_i - E_f) \mathrm{d}R_f \tag{3.1}$$

Here, $|\langle\Psi_i|\hat{V}_{if}|\Psi_f\rangle|$ describes the coupling strength between the initial and final states of the system, Ψ_i and Ψ_f are the electronic wave functions describing these states, and $\hat{V}_{if}$ is the interaction operator. The Dirac delta function ensures energy conservation in the transition, and the integral is over all resonant final states. The integral form is used to enumerate the complete set of Ψ_f. From the perspective of electronic structure calculations, Eq. (3.1) is simply formulated but very difficult to evaluate. Explicit computation of the coupling term in Eq. (3.1) must address the fact that these are two-electron transitions and hence require multi-configurational approaches beyond the single-electron excitation scheme. Additionally, Auger de-excitation in Mn^{2+}-doped semiconductors is a spin dynamic process (see Fig. 3.1) in which an excited magnetic center undergoes a spin-flip *d*-*d* transition ($^4T_1 \rightarrow\ ^6A_1$ for Mn^{2+}) and the conduction-band electron is simultaneously excited to a higher-energy state with a different spin configuration.[227, 84, 3, 9, 19] Not only is the whole process energy conserving, but it also must obey the Wigner spin conservation rule,[228, 36] *i.e.* the total spin and its projection must be conserved. Calculating such spin-flip processes is beyond the single-reference electronic structure framework. First-principles computations of the Auger de-excitation and impact excitation processes as illustrated in Fig. 3.1 are consequently intractable except for very small systems.

In some special cases, Eq. (3.1) can be factorized into a simpler form that is easier to compute than explicit evaluation of the full coupling integral. For example, such an approach has been taken to calculate Auger de-excitation rate constants in Gd^{2+}- and Mn^{2+}-doped CdF_2, where the process was proposed to proceed through the Coulomb interaction. The calculated Auger rate constants were close to the experimental values. Application of the same approach to calculating Auger de-excitation rate constants in Mn^{2+}-doped II-VI semiconductors such as $Zn_{1-x}Mn_xS$ and $Zn_{1-x}Mn_xSe$ drastically underestimated the experimental values, however, and the difference was ascribed to contributions from kinetic (*sp*-*d*) exchange. Numerical calculation of the *sp*-*d* exchange contribution was concluded to be too difficult at that time due to the non-factorizability of the exchange integral.[3, 207] Such calculations thus remain a long-standing challenge in the electronic-structure description of multi-electron ions. It is the purpose of this work to introduce and test an analytical factorization method that can serve as an alternative to multi-reference excited-state methods for calculating spin-dependent rate constants.

Here, I introduce a general method for quantitative analysis of the rate constants of Mn^{2+}-centered Auger processes in doped semiconductors. This method is illustrated by evaluating Mn^{2+}–electron Auger de-excitation dynamics in $Cd_{1-x}Mn_xS$ nanocrystals. Analytical expressions are derived that describe the direct Coulomb and *sp-d* exchange contributions to Auger de-excitation rate constants. Using time-dependent density functional theory (TDDFT) to generate input parameters, Auger de-excitation rate constants in $Cd_{1-x}Mn_xS$ nanocrystals are calculated for comparison with experiment. The calculated rate constants agree well with those measured experimentally, validating the general methodology introduced here. From these results it is concluded that *s-d* exchange coupling is ultimately responsible for the very fast rates of Auger de-excitation in Mn^{2+}-doped semiconductors.

3.2 Methodology

Microscopically, Auger de-excitation in a $Cd_{1-x}Mn_xS$ nanocrystal involves two concerted spin-flip transitions (Fig. 3.1). In one transition, a Mn^{2+} ion undergoes the ${}^4T_1 \rightarrow {}^6A_1$ spin-flip transition. In the other transition, an e_{CB} is excited to a higher energy state while reversing its spin projection (*e.g.* from $S_z = +1/2$ to $-1/2$) to conserve the total spin of the system. To describe these processes quantum mechanically, the following notation will be used,

- ${}^6A_1$ and ${}^4T_1$ refer to the ground and first-excited states of Mn^{2+}, respectively; e_{CB} (unprimed) and e'_{CB} (primed) refer to the relaxed and excited conduction-band electron, respectively.

- $\Psi_{{}^6A_1}$ and $\Psi_{{}^4T_1}$ denote the spatial wavefunctions of the ${}^6A_1$ and ${}^4T_1$ states of Mn^{2+}; $\Psi_{e_{CB}}$ and $\Psi_{e'_{CB}}$ are the e_{CB} spatial wave functions (or Bloch functions if represented in momentum space).

- For both Mn^{2+} and e_{CB}, α and β refer to spin-up and spin-down wave functions.

- $\mathbf{r}_1$, $\mathbf{r}_1$ ... are electron position vectors; ω_1, ω_2 ... are spin variables, defining the basis functions that satisfy conditions of completeness and orthonormalization.

in the Auger de-excitation process (Fig. 3.1) are defined as in Eq. (3.2) and Eq. (3.3),

$$|\Psi_i\rangle = \frac{1}{2}\left[\Psi_{^4\mathrm{T}_1}(\mathbf{r}_1)\Psi_{e_{\mathrm{CB}}}(\mathbf{r}_2) + \Psi_{^4\mathrm{T}_1}(\mathbf{r}_2)\Psi_{e_{\mathrm{CB}}}(\mathbf{r}_1)\right]\cdot\left[\alpha(\omega_1)\beta(\omega_2) - \alpha(\omega_2)\beta(\omega_1)\right], \tag{3.2}$$

$$|\Psi_f\rangle = \frac{1}{2}\left[\Psi_{^6\mathrm{A}_1}(\mathbf{r}_1)\Psi_{e'_{\mathrm{CB}}}(\mathbf{r}_2) + \Psi_{^6\mathrm{A}_1}(\mathbf{r}_2)\Psi_{e'_{\mathrm{CB}}}(\mathbf{r}_1)\right]\cdot\left[\alpha(\omega_2)\beta(\omega_1) - \alpha(\omega_1)\beta(\omega_2)\right], \tag{3.3}$$

which represent two different reference states for the Auger de-excitation process occurring at the dopant. The Auger de-excitation process is a concerted two-electron process, and the two-electron operator $\hat{V}_{if} = 1/|\mathbf{r}_1 - \mathbf{r}_2| = 1/\mathbf{r}_{12}$ gives rise to the coupling term in Eq. (3.1). As described by Eq. (3.4), this coupling term consists of two components, $J = \langle\Psi_{^4\mathrm{T}_1}(\mathbf{r}_1)\Psi_{e_{\mathrm{CB}}}(\mathbf{r}_2)|\frac{1}{\mathbf{r}_{12}}|\Psi_{^6\mathrm{A}_1}(\mathbf{r}_1)\Psi_{e'_{\mathrm{CB}}}(\mathbf{r}_2)\rangle$ describes the Coulomb contribution to coupling between Mn^{2+} $^4\mathrm{T}_1 \rightarrow {}^6\mathrm{A}_1$ and $e_{\mathrm{CB}} \rightarrow e'_{\mathrm{CB}}$ transitions (Fig. 3.2a); $K = \langle\Psi_{^4\mathrm{T}_1}(\mathbf{r}_1)\Psi_{e_{\mathrm{CB}}}(\mathbf{r}_2)|\frac{1}{\mathbf{r}_{12}}|\Psi_{e'_{\mathrm{CB}}}(\mathbf{r}_1)\Psi_{^6\mathrm{A}_1}(\mathbf{r}_2$ describes the exchange contribution to this coupling (Fig. 3.2b).

$$\begin{aligned}
&\langle\Psi_i|\hat{V}_{if}|\Psi_f\rangle \\
&=\frac{1}{4}\langle\Psi_{^4\mathrm{T}_1}(\mathbf{r}_1)\Psi_{e_{\mathrm{CB}}}(\mathbf{r}_2) + \Psi_{^4\mathrm{T}_1}(\mathbf{r}_2)\Psi_{e_{\mathrm{CB}}}(\mathbf{r}_1)|\frac{1}{\mathbf{r}_{12}}|\Psi_{^6\mathrm{A}_1}(\mathbf{r}_1)\Psi_{e'_{\mathrm{CB}}}(\mathbf{r}_2) + \Psi_{^6\mathrm{A}_1}(\mathbf{r}_2)\Psi_{e'_{\mathrm{CB}}}(\mathbf{r}_1)\rangle\cdot \\
&\quad\langle\alpha(\omega_1)\beta(\omega_2) - \alpha(\omega_2)\beta(\omega_1)|\alpha(\omega_2)\beta(\omega_1) - \alpha(\omega_1)\beta(\omega_2)\rangle \\
&=-\frac{1}{2}\left[\begin{array}{c}
\langle\Psi_{^4\mathrm{T}_1}(\mathbf{r}_1)\Psi_{e_{\mathrm{CB}}}(\mathbf{r}_2)|\frac{1}{\mathbf{r}_{12}}|\Psi_{^6\mathrm{A}_1}(\mathbf{r}_1)\Psi_{e'_{\mathrm{CB}}}(\mathbf{r}_2)\rangle+ \\
\langle\Psi_{^4\mathrm{T}_1}(\mathbf{r}_1)\Psi_{e_{\mathrm{CB}}}(\mathbf{r}_2)|\frac{1}{\mathbf{r}_{12}}|\Psi_{^6\mathrm{A}_1}(\mathbf{r}_2)\Psi_{e'_{\mathrm{CB}}}(\mathbf{r}_1)\rangle+ \\
\langle\Psi_{^4\mathrm{T}_1}(\mathbf{r}_2)\Psi_{e_{\mathrm{CB}}}(\mathbf{r}_1)|\frac{1}{\mathbf{r}_{12}}|\Psi_{^6\mathrm{A}_1}(\mathbf{r}_1)\Psi_{e'_{\mathrm{CB}}}(\mathbf{r}_2)\rangle+ \\
\langle\Psi_{^4\mathrm{T}_1}(\mathbf{r}_2)\Psi_{e_{\mathrm{CB}}}(\mathbf{r}_1)|\frac{1}{\mathbf{r}_{12}}|\Psi_{^6\mathrm{A}_1}(\mathbf{r}_2)\Psi_{e'_{\mathrm{CB}}}(\mathbf{r}_1)\rangle
\end{array}\right] \\
&=-\left[\begin{array}{c}
\langle\Psi_{^4\mathrm{T}_1}(\mathbf{r}_1)\Psi_{e_{\mathrm{CB}}}(\mathbf{r}_2)|\frac{1}{\mathbf{r}_{12}}|\Psi_{^6\mathrm{A}_1}(\mathbf{r}_1)\Psi_{e'_{\mathrm{CB}}}(\mathbf{r}_2)\rangle+ \\
\langle\Psi_{^4\mathrm{T}_1}(\mathbf{r}_1)\Psi_{e_{\mathrm{CB}}}(\mathbf{r}_2)|\frac{1}{\mathbf{r}_{12}}|\Psi_{^6\mathrm{A}_1}(\mathbf{r}_2)\Psi_{e'_{\mathrm{CB}}}(\mathbf{r}_1)\rangle
\end{array}\right] \\
&=-J-K.
\end{aligned} \tag{3.4}$$

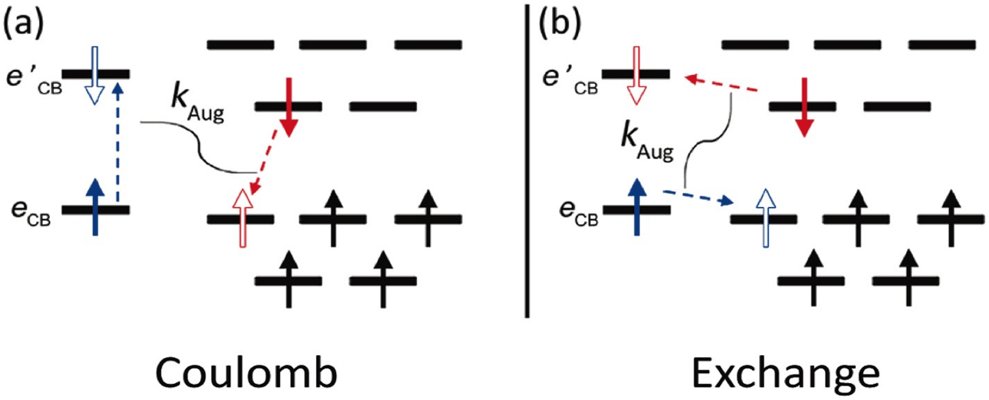

Figure 3.2: Schematic depiction of (**a**) Coulomb and (**b**) exchange contributions to Auger de-excitation in Mn^{2+}-doped semiconductors. The initial state ($Mn^{2+}(^4T_1)$, e_{CB}) is represented by the filled arrows. Auger de-excitation in each case is represented by the thin dashed arrows.

3.2.1 Coulomb Interaction

The $^4T_1 \rightarrow {}^6A_1$ transition density is confined by a small volume at the dopant site $\mathbf{r}_1$, whereas the $e_{CB} \rightarrow e'_{CB}$ transition (described by $\mathbf{r}_2$) is delocalized over the entire electron envelope function, in this case determined by the nanocrystal volume. Interaction between electron densities in this special case can be treated with a multipole-expansion technique. Using the Legendre expansion,[18] the Coulomb operator in the case of $r_2 \gg r_1$ is given by Eq. (3.5),

$$\begin{aligned}\frac{1}{|\mathbf{r}_1 - \mathbf{r}_2|} &= \frac{1}{r_1} \sum_{k=0}^{\infty} \left(\frac{r_2}{r_1}\right)^k P_k\left(\frac{\mathbf{r}_1 \cdot \mathbf{r}_2}{r_1 r_2}\right) \\ &= \frac{1}{r_1} + \frac{\mathbf{r}_1 \cdot \mathbf{r}_2}{r_1^3} + \frac{1}{2}\left(\frac{3\left[\mathbf{r}_1 \cdot \mathbf{r}_2\right]^2}{r_1^5} - \frac{r_2^2}{r_1^3}\right) + \mathrm{O}\left(\frac{r_2^3}{r_1^4}\right). \qquad (3.5)\end{aligned}$$

where P_k is the k-th Legendre polynomial and r is the norm of the vector $\mathbf{r}$. The first three terms in Eq. (3.5) are the monopole, dipole, and quadrupole terms, respectively. For the Coulomb interaction discussed here, the dominant interaction is the dipole term,[3] giving rise to Eq. (3.6),

$$J = \langle \Psi_{^4\mathrm{T}_1}(\mathbf{r}_1)\Psi_{e_{\mathrm{CB}}}(\mathbf{r}_2)|\frac{1}{\mathbf{r}_{12}}|\Psi_{^6\mathrm{A}_1}(\mathbf{r}_1)\Psi_{e'_{\mathrm{CB}}}(\mathbf{r}_2)\rangle \simeq \langle \Psi_{^4\mathrm{T}_1}|\mathbf{r}|\Psi_{^6\mathrm{A}_1}\rangle \cdot \langle \Psi_{e_{\mathrm{CB}}}|\frac{\mathbf{r}}{r^3}|\Psi_{e'_{\mathrm{CB}}}\rangle \tag{3.6}$$

The first integral on the right-hand side of Eq. (3.6) is the electric transition dipole moment for the $^4\mathrm{T}_1 \rightarrow {}^6\mathrm{A}_1$ transition, and has been attributed to the dipole-monopole interaction mechanism in Auger processes.[3] The oscillator strength for the $^4\mathrm{T}_1 \rightarrow {}^6\mathrm{A}_1$ transition is on the order of $10^{-6} \sim 10^{-5}$, corresponding to a radiative decay rate constant of about $10^2 \sim 10^3$ s^{-1}.[9, 19] Even if the oscillator strength of the $e_{\mathrm{CB}} \rightarrow e'_{\mathrm{CB}}$ transition were 1, this small Mn^{2+} oscillator strength yields a multipolar energy-transfer rate constant many orders of magnitude smaller than those measured experimentally in $\mathrm{Cd}_{1-x}\mathrm{Mn}_x\mathrm{S}$, $\mathrm{Zn}_{1-x}\mathrm{Mn}_x\mathrm{Se}$, and $\mathrm{Zn}_{1-x}\mathrm{Mn}_x\mathrm{S}$.[227, 84, 3, 9] I therefore conclude that Coulomb-type coupling makes a negligible contribution to the fast Auger de-excitation observed in Mn^{2+}-doped semiconductor nanocrystals,[227] as concluded previously for bulk materials.[3] A related conclusion also applies to exciton-to-Mn^{2+} energy transfer, which is sometimes also referred to as an Auger process.[47] Evaluation of the exchange-type coupling is thus essential to understanding the physical origin of fast Auger de-excitation in Mn^{2+}-doped semiconductors.

3.2.2 Exchange Interaction

Direct evaluation of the exchange integral is difficult. K (from Eq. (3.4)) cannot be factorized using the multipole expansion approach, and for this reason it has not been explicitly calculated to date. Here, I introduce a general method for addressing this long-standing challenge: Using the *Cauchy-Schwarz* inequality,[18] K is factorized into fundamental exchange interactions between dopants and charge carriers as shown in Eq. (3.7),

$$\begin{aligned} K^2 &= |\langle \Psi_{^4\mathrm{T}_1}(\mathbf{r}_1)\Psi_{e_{\mathrm{CB}}}(\mathbf{r}_2)|\frac{1}{\mathbf{r}_{12}}|\Psi_{^6\mathrm{A}_1}(\mathbf{r}_2)\Psi_{e'_{\mathrm{CB}}}(\mathbf{r}_1)\rangle|^2 \leq K_1 \cdot K_2 \\ K_1 &= \langle \Psi_{^4\mathrm{T}_1}(\mathbf{r}_1)\Psi_{e_{\mathrm{CB}}}(\mathbf{r}_2)|\frac{1}{\mathbf{r}_{12}}|\Psi_{^4\mathrm{T}_1}(\mathbf{r}_2)\Psi_{e_{\mathrm{CB}}}(\mathbf{r}_1)\rangle \\ K_2 &= \langle \Psi_{^6\mathrm{A}_1}(\mathbf{r}_1)\Psi_{e'_{\mathrm{CB}}}(\mathbf{r}_2)|\frac{1}{\mathbf{r}_{12}}|\Psi_{^6\mathrm{A}_1}(\mathbf{r}_2)\Psi_{e'_{\mathrm{CB}}}(\mathbf{r}_1)\rangle \end{aligned} \tag{3.7}$$

This expression gives the upper bound of the exchange-type coupling as the product of two terms, K_1 and K_2. K_1 is related to the fundamental *s*-*d* exchange interaction between a Mn^{2+} in the $^4\mathrm{T}_1$ state and e_{CB}, and K_2 is related to the *s*-*d* exchange interaction between a Mn^{2+} in the $^6\mathrm{A}_1$ state and e'_{CB}. This upper bound expression approaches equality when K_1 and K_2 become linearly dependent on each other. Appendix B presents a detailed discussion of the relationship between K_1 and K_2 in Mn^{2+}-doped semiconductors and outlines the conditions when Eq. (3.7) takes on the equality form.

I now show that Eq. (3.7) provides an effective way to evaluate exchange contributions to dopant-carrier Auger rate constants in Mn^{2+}-doped semiconductors. The $^4\mathrm{T}_1$ state has the $d^5[e(\alpha)^2 e(\beta)^1 t(\alpha)^2]$ configuration (Fig. 3.1). If e_{CB} has spin α (or β), then the coupling in the Mn^{2+}-e_{CB} system is defined as ferromagnetic (or antiferromagnetic). The total energy difference between the ferromagnetic (FM) and antiferromagnetic (AFM) states is the so-called *s*-*d* exchange splitting. Eq. (3.8) describes the relationship between K_1 and the $\mathrm{Mn}^{2+}(^4\mathrm{T}_1)$-$e_{\mathrm{CB}}$ *s*-*d* exchange splitting (see Appendix B). Following a similar procedure, K_2 is described by Eq. (3.9).

$$K_1 = \frac{4}{3} E^{s-d}_{^4\mathrm{T}_1 - e_{\mathrm{CB}}} = \frac{4}{3}\left(E^{\mathrm{AFM}}_{^4\mathrm{T}_1 - e_{\mathrm{CB}}} - E^{\mathrm{FM}}_{^4\mathrm{T}_1 - e_{\mathrm{CB}}}\right), \tag{3.8}$$

$$K_2 = E^{s-d}_{^6\mathrm{A}_1 - e'_{\mathrm{CB}}} = \left(E^{\mathrm{AFM}}_{^6\mathrm{A}_1 - e'_{\mathrm{CB}}} - E^{\mathrm{FM}}_{^6\mathrm{A}_1 - e'_{\mathrm{CB}}}\right). \tag{3.9}$$

The exchange splittings (E_{s-d}) for both the $^4\mathrm{T}_1$-e_{CB} and $^6\mathrm{A}_1$-e'_{CB} exchange interactions can be described using the *Heisenberg-Dirac-van-Vleck* Hamiltonian ($E^{s-d} = -J^{s-d} \cdot \hat{S}_1 \cdot \hat{S}_2$,[219, 209] where J^{s-d} is the exchange coupling constant), as in Eq. (3.10) and Eq. (3.11),

$$E^{s-d}_{^4\mathrm{T}_1 - e_{\mathrm{CB}}} = 4 J^{s-d}_{^4\mathrm{T}_1 - e_{\mathrm{CB}}}, \tag{3.10}$$

$$E^{s-d}_{^6\mathrm{A}_1 - e'_{\mathrm{CB}}} = 6 J^{s-d}_{^6\mathrm{A}_1 - e'_{\mathrm{CB}}}. \tag{3.11}$$

In the next section, I apply the above expressions with exchange energies K_1 and K_2 computed from density functional theory (DFT) to evaluate Auger de-excitation rates in Mn^{2+}-doped CdS nanocrystals.

3.2.3 DFT Calculations

Nearly spherical wurtzite CdS nanocrystals, $Cd_{33}S_{33}$ and $Cd_{84}S_{84}$ (Fig. 3.3), were constructed with C_{3v} symmetry using experimental lattice parameters: $a = 4.135$ Å, $c = 6.749$ Å, and u = 0.345.[232] The diameters of these nanocrystals are about 1.2 nm and 1.8 nm, respectively. Dangling bonds on the nanocrystal surfaces were passivated with pseudo-hydrogen atoms, which have modified nuclear charges of 0.5 and 1.5 to terminate surface S^{2-} and Cd^{2+} ions, respectively (see ref. [11] for detailed discussion of the surface capping scheme). All calculations were performed with the development version of the Gaussian program suite.[74] Nanocrystal electronic structures were obtained with the PBE1PBE hybrid DFT functional.[2] The Los Alamos double-ζ pseudo-core potential (LANL2DZ)[96, 95, 220] and the associated basis set were used for all atoms, with the Cd(5*s*, 4*d*), Mn(3*s*, 3*p*, 4*s*, 3*d*), and S(3*s*, 3*p*) electrons treated explicitly with basis functions. Excited-state energies were calculated with the LR-TDDFT[184, 206] at the TD-PBE1PBE/LANL2DZ level of theory. The accuracy of the model and DFT theory used in this work have been extensively validated by comparing calculated geometries, electronic structures, magnetic exchange constants, and absorption spectra of diluted magnetic semiconductor quantum dots with experimental data.[11, 167, 12, 13] For Mn^{2+}-doped CdS nanocrystals, Mn^{2+} ions were introduced substitutionally into the lattice, such that the total charge of the cluster remained neutral. Because the $Mn^{2+}(^6A_1)$ and Zn^{2+} are comparable in size and both have spherically symmetric *d*-shell orbital configurations (d^5 and d^{10}), the geometry does not change within the convergence criteria. Natural transition orbital (NTO)[149] analysis based on the calculated transition densities between the ground and excited states was used to describe the electronic characteristics of excited states. The NTO approach provides a compact representation of the electronic transitions in terms of an expansion into single-particle orbitals (electron and hole) by diagonalizing the transition density matrix associated with each excitation. For closed-shell calculations, an excitation can be described by a pair of spin-independent transition orbitals, whereas for open-shell calculations, two sets of spin-transition orbitals have to be considered for a given excitation (spin-up and spin-down manifolds). All NTOs shown in this paper were produced with an isosurface value of ± 0.02.

3.3 Application to Spin-Dependent Auger De-Excitation in Mn^{2+}-Doped Semiconductor Nanocrystals

The equations presented above provide a framework for evaluation of Mn^{2+}-e_{CB} Auger de-excitation rate constants. The key exchange integrals K_1 and K_2 are not known from experiment but can be estimated using electronic structure calculations. DFT calculations were therefore performed on Mn^{2+}-doped CdS nanocrystals.

Fig. 3.4 shows density-of-state (DOS) diagrams calculated by DFT for a $\mathrm{Cd}_{1-x}\mathrm{Mn}_x\mathrm{S}$ nanocrystal containing one Mn^{2+} ion in both its ground ($^6\mathrm{A}_1$) and first-excited ($^4\mathrm{T}_1$) states. The majority spin (α) of Mn^{2+} is defined as aligned in the spin-up direction. When the Mn^{2+} ion is in the $^4\mathrm{T}_1$ state, the $d(\beta)$ electron is located above the top edge of the CdS valence band. When the $^4\mathrm{T}_1 \rightarrow {}^6\mathrm{A}_1$ transition occurs at the Mn^{2+} center, the $d(\beta)$ electron becomes a (α) electron, and the density above the top of the valence band disappears. The $^4\mathrm{T}_1 \rightarrow {}^6\mathrm{A}_1$ transition is highly localized at the Mn^{2+}, so its energy is independent of the Mn^{2+} location within the quantum dot. DFT calculations predict an energy difference between $^4\mathrm{T}_1$ and $^6\mathrm{A}_1$ states of about 2.05 eV for all dopant positions considered here (in the absence of e_{CB}), agreeing well with the experimentally measured $^4\mathrm{T}_1 \rightarrow {}^6\mathrm{A}_1$ electronic origin energy of about 2.12 eV (585 nm) in CdS.[124, 20]

3.3.1 Mn^{2+}-e_{CB} Exchange Energies

To calculate $E^{s-d}_{^4\mathrm{T}_1-e_{\mathrm{CB}}}$ from Eq. (3.8), the quadratic convergence approach[10] was used to identify the electron configuration of the $^4\mathrm{T}_1$ state in the presence of e_{CB}. Fig. 3.5a,b show that $\Psi_{e_{\mathrm{CB}}}$ is delocalized over the volume of the quantum dot. The density distribution of the band-edge electron is reasonably reproduced using a zero-order Bessel function (Eq. (3.12)),[33] where D is the nanocrystal diameter,

$$|\Psi_{e_{\mathrm{CB}}}|^2 = \frac{\sin^2(2\pi r/D)}{r^2\pi D}. \tag{3.12}$$

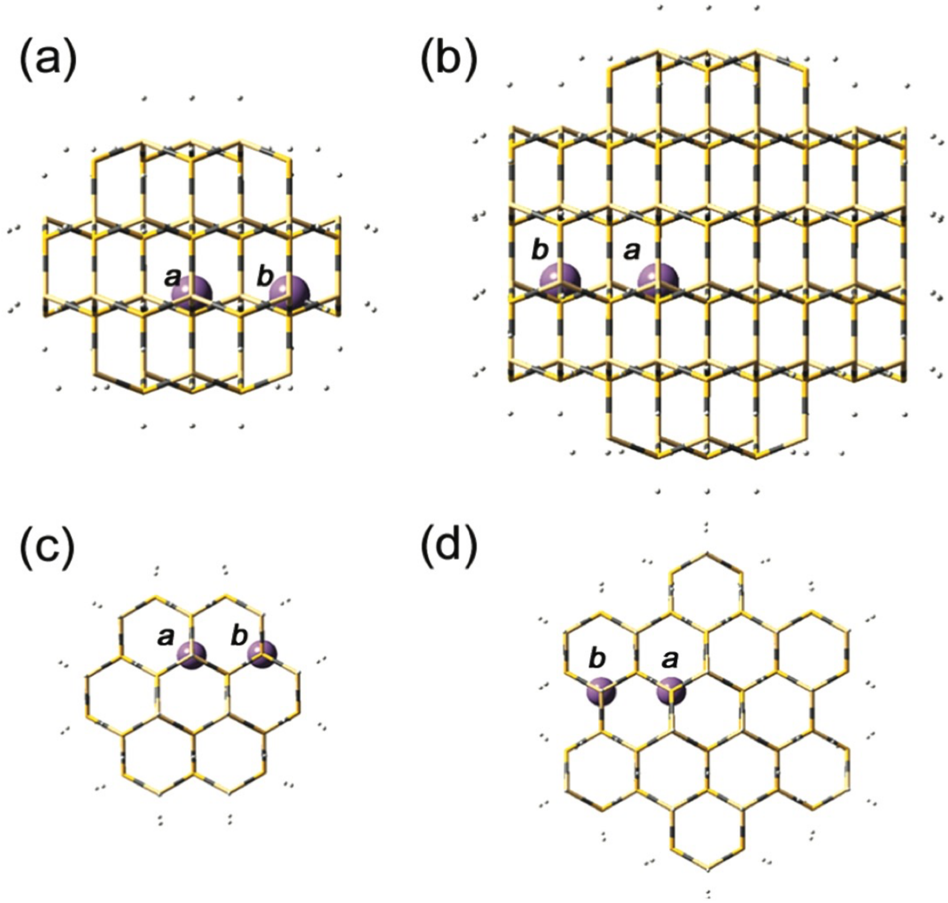

Figure 3.3: Structures of the Mn^{2+}-doped CdS nanocrystals studied here: (**a**, **c**) $Cd_{32}MnS_{33}$, with $D = 1.2$ nm. (**b**, **d**) $Cd_{83}MnS_{84}$, with $D = 1.8$ nm. The purple spheres represent the Mn^{2+} ions, and the labels a and b denote the two Mn^{2+} substitution positions indicated. The distances of the two substitution potions to the QD geometric center are 0.319 nm and 0.494 nm, respectively. (**a**) and (**b**) are side-views and (**c**) and (**d**) are top views of the nanocrystals.

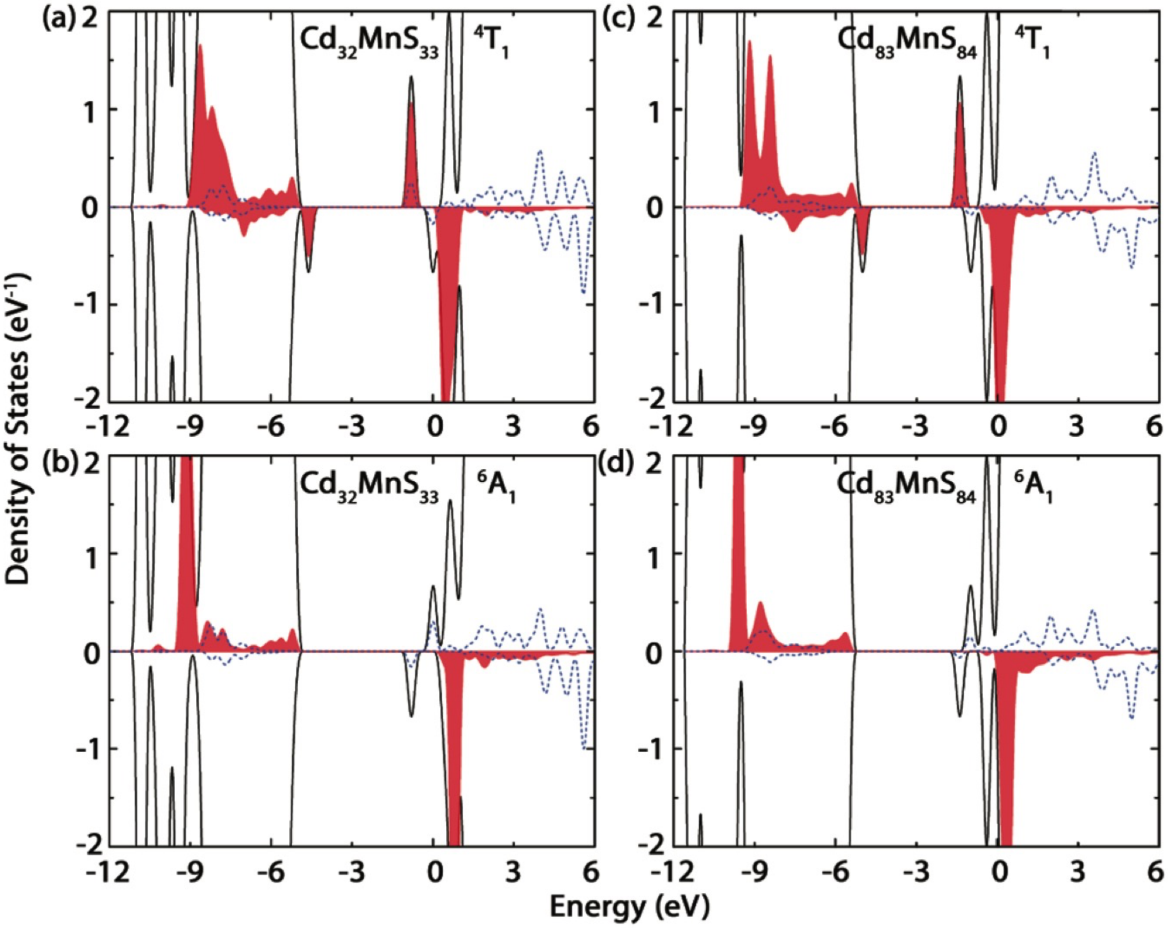

Figure 3.4: Total DOS of $\mathrm{Cd}_{1-x}\mathrm{Mn}_x\mathrm{S}$ nanocrystals (black solid lines), and partial DOS for the Mn^{2+} $3d$ levels (red, shaded) and Mn^{2+} $4s$ levels (blue dashed line). (**a**) $\mathrm{Cd}_{32}\mathrm{MnS}_{33}$ with Mn^{2+} in the $^4\mathrm{T}_1$ state. (**b**) $\mathrm{Cd}_{32}\mathrm{MnS}_{33}$ with Mn^{2+} in the $^6\mathrm{A}_1$ state. (**c**) $\mathrm{Cd}_{83}\mathrm{MnS}_{84}$ with Mn^{2+} in the $^4\mathrm{T}_1$ state. (**d**) $\mathrm{Cd}_{83}\mathrm{MnS}_{84}$ with Mn^{2+} in the $^6\mathrm{A}_1$ state.

Because the *s*-*d* exchange splitting depends on the position of the dopant relative to the center of the electron distribution,[167, 21] I consider two unique dopant positions in the present analysis, one closer to the quantum dot center (Mn^{2+}-*a*) and the other closer to the surface (Mn^{2+}-*b*) (see Fig. 3.3 for Mn^{2+} positions). Tab. 3.1 summarizes the calculated *s*-*d* exchange splittings in $\mathrm{Cd}_{1-x}\mathrm{Mn}x\mathrm{S}$ nanocrystals for both the $^6\mathrm{A}_1$ and $^4\mathrm{T}_1$ states. *s*-*d* exchange in Mn^{2+}-doped semiconductors favors parallel alignment of the Mn^{2+} *d* electron and e_{CB} spins,[76] even in small QDs,[19, 21] and this alignment is reproduced in these calculations for the $^6\mathrm{A}_1$ state and e_{CB} as shown in Tab. 3.1 ($E^{s-d}_{^6\mathrm{A}_1-e'_{\mathrm{CB}}} > 0$). Tab. 3.1 shows that ferromagnetic alignment of electron and dopant spins is also preferred when Mn^{2+} is in its $^4\mathrm{T}_1$ state. The exchange splittings are calculated to be dependent on the position of the dopant as expected, with the strongest interactions occurring when Mn^{2+} is closest to the nanocrystal center. The *s*-*d* exchange splitting decreases with increasing nanocrystal size as a result of the decreased local e_{CB} density at the dopant site (Eq. (3.12)). As seen from Tab. 3.1, the *s*-*d* exchange splitting is larger when Mn^{2+} is in its $^6\mathrm{A}_1$ state than in its $^4\mathrm{T}_1$ state. The origin of this trend is largely due to the dependence of E^{s-d} on Mn^{2+} total spin (Eq. (3.10) and Eq. (3.11)). Additionally, $\mathrm{Mn}^{2+}(4s)$-e_{CB} hybridization decreases slightly when Mn^{2+} is promoted to its $^4\mathrm{T}_1$ excited state, and because *s*-*d* exchange proceeds primarily through a $\mathrm{Mn}^{2+}(4s)$-e_{CB} orbital pathway,[19, 21] this decrease also contributes to the smaller E^{s-d} of the $^4\mathrm{T}_1$ state. From Eq. (3.10) and Eq. (3.11), $J^{s-d}_{^4\mathrm{T}_1-e_{\mathrm{CB}}}$ and $J^{s-d}_{^6\mathrm{A}_1-e'_{\mathrm{CB}}}$ can be calculated and are listed in Tab. 3.1. The calculated $J^{s-d}_{^6\mathrm{A}_1-e'_{\mathrm{CB}}}$ is on the same order of magnitude as the experimental value for the average Mn^{2+} position (mean-field value) of ∼1.1 meV.[99]

3.3.2 $\mathrm{Mn}^{2+}(^6A_1)$-e'_{CB} Magnetic Exchange

LR-TDDFT was used to compute the energies and wave functions of various e'_{CB} states, which were then evaluated to identify those most likely to be involved in the Auger de-excitation process. Two characteristic features of e'_{CB} states can be used to identify their relevance to Auger de-excitation: (i) Because Auger de-excitation conserves energy, the energy of

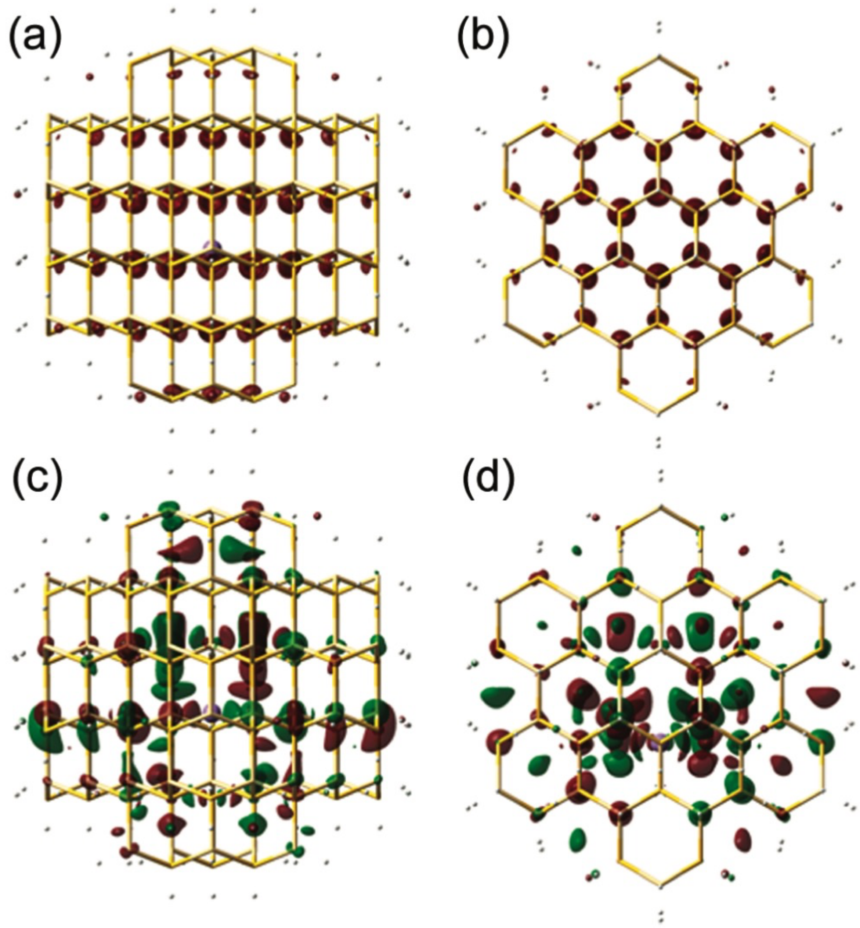

Figure 3.5: Electron wave functions in CdS nanocrystals: (**a**) side-view and (**b**) top-view of $\Psi_{e_{\mathrm{CB}}}$; (**c**) side-view and (**d**) top-view of $\Psi_{e'_{\mathrm{CB}}}$ approximately 2.05 eV above the band edge (isosurface value: ± 0.02) .

Table 3.1: Summary of the results from DFT calculations on $Cd_{1-x}Mn_xS$ nanocrystals, including Mn^{2+} $^4T_1 \rightarrow {}^6A_1$ transition energies, Mn^{2+}-electron exchange energies involving both the $^4T_1$ and $^6A_1$ states in nanocrystals containing an additional conduction-band electron (e_{CB} or e'_{CB}), and the ratio of $J^{s-d}_{^6\mathrm{A}_1-e'_{\mathrm{CB}}}$ to $J^{s-d}_{^4\mathrm{T}_1-e_{\mathrm{CB}}}$ for each nanocrystal. Dopant positions Mn-*a* and Mn-*b* are depicted in Fig. 3.3.

	Energies	$Cd_{32}MnS_{33}$		$Cd_{83}MnS_{84}$	
		Mn-*a*	Mn-*b*	Mn-*a*	Mn-*b*
$^6\mathrm{A}_1 \rightarrow {}^4\mathrm{T}_1$	$\Delta E_{\mathrm{Mn}} = E(^4\mathrm{T}_1) - E(^6\mathrm{A}_1)$ (eV)	2.0396	2.0553	2.0363	2.0372
$^6\mathrm{A}_1 \rightarrow e_{\mathrm{CB}}$	$E^{s-d}_{^6\mathrm{A}_1-e_{\mathrm{CB}}} = E^{\mathrm{AFM}}_{^6\mathrm{A}_1-e_{\mathrm{CB}}} - E^{\mathrm{FM}}_{^6\mathrm{A}_1-e_{\mathrm{CB}}}$ (meV)	34.2	14.2	20.1	8.1
	$J^{s-d}_{^6\mathrm{A}_1-e_{\mathrm{CB}}}$	5.7	2.4	3.4	1.4
$^6\mathrm{A}_1 \rightarrow e'_{\mathrm{CB}}$	$E^{s-d}_{^6\mathrm{A}_1-e'_{\mathrm{CB}}} = E^{\mathrm{AFM}}_{^6\mathrm{A}_1-e'_{\mathrm{CB}}} - E^{\mathrm{FM}}_{^6\mathrm{A}_1-e'_{\mathrm{CB}}}$ (meV)	18.8	18.4	12.0	12.0
	$J^{s-d}_{^6\mathrm{A}_1-e'_{\mathrm{CB}}}$	4.7	4.6	3.0	3.0
$^4\mathrm{T}_1 \rightarrow e_{\mathrm{CB}}$	$E^{s-d}_{^4\mathrm{T}_1-e_{\mathrm{CB}}} = E^{\mathrm{AFM}}_{^4\mathrm{T}_1-e_{\mathrm{CB}}} - E^{\mathrm{FM}}_{^4\mathrm{T}_1-e_{\mathrm{CB}}}$ (meV)	11.2	6.3	8.2	1.3
	$J^{s-d}_{^4\mathrm{T}_1-e_{\mathrm{CB}}}$	2.8	1.6	2.1	0.3
Ratio	$J^{s-d}_{^6\mathrm{A}_1-e'_{\mathrm{CB}}}/J^{s-d}_{^4\mathrm{T}_1-e_{\mathrm{CB}}}$	1.7	2.9	1.4	10.0

$|e'_{\mathrm{CB}}, ^6\mathrm{A}_1\rangle$ must be similar to that of $|e_{\mathrm{CB}}, ^4\mathrm{T}_1\rangle$. On this basis, I limit my analysis to e'_{CB} states that are close in energy to $\Delta E^{\mathrm{FM}} = E^{\mathrm{FM}}_{^4\mathrm{T}_1-e_{\mathrm{CB}}} - E^{\mathrm{FM}}_{^6\mathrm{A}_1-e_{\mathrm{CB}}}$ or $\Delta E^{\mathrm{AFM}} = E^{\mathrm{AFM}}_{^4\mathrm{T}_1-e_{\mathrm{CB}}} - E^{\mathrm{AFM}}_{^6\mathrm{A}_1-e_{\mathrm{CB}}}$; (ii) Mn^{2+}-electron exchange is dominated by spin-dependent hybridization between Mn^{2+} and electron wave functions.[19, 21] Excited states with these properties were identified in the TDDFT calculations and their energies are listed in Tab. 3.1. For the $\mathrm{Cd}_{32}\mathrm{MnS}_{33}$ QD, there is only one TDDFT-calculated e'_{CB} state that satisfies the energy conservation criterion ±25 meV. This state has 7% electron density localized on Mn^{2+}. This e'_{CB} wave function is displayed in Fig. 3.5c,d and exhibits several radial nodes, which is very different from that of e_{CB} (Fig. 3.5a,b). Radial nodes are characteristic of higher-order Bessel functions. For the larger $\mathrm{Cd}_{83}\mathrm{MnS}_{84}$ QD, there are more e'_{CB} states meeting the energy conservation criterion. The excitation energies and Mn^{2+} electron density contributions for each energetically resonant state are listed in Tab. 3.2. Because the exchange coupling is linearly proportional to the spin-dependent Mn^{2+}-electron hybridization, states with $\rho(\mathrm{Mn}^{2+}) \leq 0.1\%$ make negligible contributions to exchange-mediated Auger rate constants. As a result, one $^6\mathrm{A}_1 - e'_{\mathrm{CB}}$ state generally dominates the exchange-mediated Auger de-excitation rate constant. The only exception in Tab. 3.2 is the AFM configuration of position a, which possesses three $^6\mathrm{A}_1 - e'_{\mathrm{CB}}$ states with $> 0.1\%$ Mn^{2+} character. For this case, the average exchange coupling constant is reported in Tab. 3.1.

As shown in Appendix B, the ratio of $J^{s-d}_{^6\mathrm{A}_1-e'_{\mathrm{CB}}}$ to $J^{s-d}_{^4\mathrm{T}_1-e_{\mathrm{CB}}}$ can be used as an indicator of the quality of the factorization scheme for the exchange-type Auger coupling in Eq. (3.7). Using the calculated s-d coupling constants, the ratio of $J^{s-d}_{^6\mathrm{A}_1-e'_{\mathrm{CB}}}$ to $J^{s-d}_{^4\mathrm{T}_1-e_{\mathrm{CB}}}$ is ∼1.5 for the Mn^{2+} positions closest to the centers of each nanocrystal considered here. Although its specific value varies, this ratio is nearly constant for all calculations, suggesting that the equality form of Eq. (3.7) can be applied to factorize the exchange-type Auger coupling in Mn^{2+}-doped semiconductor nanocrystals.

Table 3.2: Mn^{2+} electron density contribution, $\rho(\mathrm{Mn}^{2+})$, in ${}^6\mathrm{A}_1 - e'_{\mathrm{CB}}$ states that satisfy the energy conservation criterion to be within ±25 meV in $\mathrm{Cd}_{83}\mathrm{MnS}_{84}$ QDs. The excitation energies, ΔE's, have been calculated using the LR-TDDFT method.

	AFM		FM			AFM		FM	
	ΔE	$\rho(\mathrm{Mn}^{2+})$	ΔE	$\rho(\mathrm{Mn}^{2+})$		ΔE	$\rho(\mathrm{Mn}^{2+})$	ΔE	$\rho(\mathrm{Mn}^{2+})$
Position *a*					Position *b*				
(1)	2.0257	0.7 %	2.0414	0.05%	(1)	2.0513	1.1 %	2.0474	0.1%
(2)	2.0336	0.6 %	2.0452	1.2%	(2)			2.0506	1.9%
(3)	2.0519	1.5 %							

3.3.3 Auger De-excitation in $Cd_{1-x}Mn_xS$ Nanocrystals

The two sections above present DFT results addressing the *s*-*d* exchange splittings, $E^{s-d}_{{}^4\mathrm{T}_1-e_{\mathrm{CB}}}$ and $E^{s-d}_{{}^6\mathrm{A}_1-e'_{\mathrm{CB}}}$. As derived in the Methodology section, these two *s*-*d* exchange interactions are closely related to the exchange-type contribution to Auger de-excitation. K_1 and K_2 from can now be calculated using Eq. (3.8) and Eq. (3.9) and the DFT results of Tab. 3.1. The results of such calculations are summarized in Tab. 3.3. Auger de-excitation rate constants are then calculated from Fermi's Golden Rule (Eq. (3.1)) using only the exchange-type coupling. Coupling to nuclear degrees of freedom is neglected at this stage.

For a given nanocrystal, k_{Aug} depends sensitively on the Mn^{2+} position within the nanocrystal because of the Bessel-like e_{CB} probability distribution (Equation (3.12)), as discussed above. k_{Aug} also depends on the nanocrystal diameter, scaling as $\sim 1/D$ for Mn^{2+} fixed at the nanocrystal center, for example. Nevertheless, all k_{Aug} values in Tab. 3.1 fall in the range of $10^{11} - 10^{12}$ s^{-1}. Using Eq. (3.12) and the position-to-center distances noted in Fig. 3.3, a simple extrapolation to nanocrystal diameters for which experimental Auger de-

Table 3.3: Exchange coupling energies, Auger de-excitation rate constants, and corresponding time constants calculated for $Cd_{1-x}Mn_xS$ nanocrystals.

	$Cd_{32}MnS_{33}$		$Cd_{83}MnS_{84}$	
	Mn-*a*	Mn-*b*	Mn-*a*	Mn-*b*
K_1 (meV)	14.9	8.4	10.9	1.7
K_2 (meV)	18.8	18.4	26.8	12.0
K (meV)	16.8	12.4	17.1	4.6
k_{Aug} (s^{-1})	2.14×10^{12}	1.48×10^{12}	2.80×10^{12}	1.99×10^{11}

excitation rate constants exist ($D \sim 4.5$ nm) yields $K \sim 1$ meV for the dopant position closest to the nanocrystal's geometric center ($r = 0.32$ nm), similar to position *a* in Fig. 3.3, and ∼0.2 meV for a dopant nearer the nanocrystal surface (r = 2.0 nm), according to Eq. (3.12). From these values, $k_{\mathrm{Aug}} \sim 4.6 \times 10^8 - 9.5 \times 10^9$ s^{-1} is calculated for the 4.5 nm nanocrystal, in excellent agreement with the experimental value of $k_{\mathrm{Aug}} \sim 2 \times 10^9$ s^{-1}.[66, 227] This agreement strongly implicates *s*-*d* exchange as the dominant factor determining Auger de-excitation rate constants in Mn^{2+}-doped CdS nanocrystals and, by extension, other Mn^{2+}-doped semiconductors.

3.4 Summary

A method for analyzing the mechanism and kinetics of Auger de-excitation in Mn^{2+}-doped semiconductors has been introduced. Mathematical expressions have been derived that allow quantitative evaluation of the Coulomb and exchange contributions to Auger de-excitation in Mn^{2+}-doped semiconductors. A key advantage of this method is that all quantities in these expressions can be calculated using existing electronic structure methods without the computational expense of multi-reference approaches. Using the results of DFT calculations as input, this method was successfully applied to compute Auger de-excitation rate constants in $\mathrm{Cd}_{1-x}\mathrm{Mn}_x\mathrm{S}$ nanocrystals. The computational results agree well with recent experimental measurements, validating the general method introduced here. Deeper analysis reveals that e'_{CB}-$^6\mathrm{A}_1$ exchange is stronger than e_{CB}-$^6\mathrm{A}_1$ exchange because of greater carrier hybridization with the $\mathrm{Mn}^{2+}(4s)$ orbital in the former. This large $\mathrm{Mn}^{2+}(4s)$-e'_{CB} hybridization is the major reason why Mn^{2+}-e_{CB} Auger de-excitation is as fast as e_{CB}-exciton Auger recombination in the corresponding undoped nanocrystals despite involving coupling of a highly localized transition with a highly delocalized transition.

Auger de-excitation in $\mathrm{Cd}_{1-x}\mathrm{Mn}_x\mathrm{S}$ nanocrystals was examined as a model system to illustrate the theoretical approach introduced here for treating concerted two-electron transitions computationally, but this approach is general and hence can in principle also be applied to describing other concerted two-electron processes. Specifically, the success of the Auger de-excitation calculations in Mn^{2+}-doped semiconductor nanocrystals is encouraging and suggests that this approach would also be useful for quantitative analysis of other Auger-type processes in Mn^{2+}-doped semiconductors such as exciton-to-Mn^{2+} energy transfer or Mn^{2+}-exciton Auger recombination, as well as for analysis of Auger-type processes in related materials or molecules. This approach could possibly even be valuable for computational design of materials with desirable Auger kinetics (either fast or slow) for various photonics or electro-optics applications.

Chapter 4

REAL-TIME TIME-DEPENDENT DENSITY FUNCTIONAL THEORY (RT-TDDFT) FOR EXCITED STATE DYNAMICS

Understanding dynamical characteristics of excited electronic states is crucial for rational design of functional nanomaterials. Using RT-TDDFT, I present a fully quantum mechanical study on the transfer and decay of an exciton in an archetypal metal nanostructure. I introduce several approaches to analyze the dipole moment's time-evolution to resolve exciton transfer rates and the pure dephasing times. These approaches are applied to studies of exciton diffusion length in a silver atomic chain array. Calculated rates of polarization-induced transfer exhibit neither Förster's "sixth-power" dependence on donor-acceptor distance nor the perfect exponential separation dependence that typifies the Dexter transfer mechanism, suggesting that the non-perturbative, *ab initio* quantum dynamics captures intricacies of exciton transfer between quantized nanosystems that are beyond the reach of the canonical models of electronic energy transfer.

4.1 Introduction

Excitons, or Coulombically bound electron-hole pairs, are well-known to chemists, physicists, and material scientists alike as the quasiparticles (or elementary excitations) that result from coherent light-matter interactions and mediate most processes that occur in electronically excited states. These excitonic processes are the underlying driving forces in solar energy-conversion and photocatalysis in inorganic[114, 212, 181, 120] and molecular[15, 208] semiconducting systems. Bound excitonic states also exist in metallic systems, but are fleetingly short-lived owing to the rapid (sub-femtosecond) onset of Coulomb screening.[67, 146] One route to prolonging the lifetime of excitonic states in conducting materials in order to enable some excitonically-promoted physical process could be to utilize the quantized nature of nanosized metal clusters. Unlike their bulk/macroscopic counterparts, metal nanocrystals (*e.g.* nanowires) do not possess a dense band of delocalized states around the Fermi level. As a result, the photoexcited electron-hole pair can be long-lived due to the smaller resonant broadening of the excited state. Some of these long-lived excited states can even form coherent molecular plasmons as shown in previous work.[89, 109, 88, 26, 122, 60]

Underlying the potential of using the long-lived exciton in metal nanocrystals for energy research is the diffusion length of the exciton, *i.e.* the distance an exciton may travel prior to its complete decay. This important property determines the feasibility of harvesting the exciton for energy-conversion and the engineering requirement of making a practical device. The exciton diffusion length is intrinsically related to the exciton transfer rate and the exciton decay time. However, due to its complex many-electron nature, calculating the exciton diffusion length from first-principles has been a challenging task. Cao *et al.* have investigated energy transfer in perfect J-aggregates by associating excitons with Bloch states.[49] The analytical expression for the transfer rate they derive goes beyond the dipolar coupling model assumed in the classical Förster equation.[72] In their recent work on the topic, Lusk and coworkers employed the *ab initio* Green's function/GWA approach to explicitly solve the excited-state electronic structure problem as it pertains to the rate of coherent exciton transfer between silicon nanocrystals.[136] Results demonstrated the breakdown of the Förster model for exciton transport at donor-acceptor distances of $\sim$ 2 nm or less. The authors argue that exchange energies could become comparable to those of direct Coulomb interactions at such small separations.

In this chapter, I study the dynamical evolution of an exciton in a two-silver atomic chain array using first-principles electronic dynamics. I will focus on resolving the exciton decay and transfer rates and building a theoretical understanding of the mechanisms. I will explore these phenomena for numerous separation distances and obtain estimated exciton diffusion lengths. The control over the atomic chains' distance allowed through the theoretical approach yields spatially resolved results that can serve as a valuable starting point for the optimization of exciton diffusion processes in organized atomic chain arrays.

4.2 Methodology

4.2.1 Real-Time Time-Dependent Density Functional Theory and Properties

In the following discussions, the density, KS, and dipole operators are expressed in both atomic orbital (AO) and orthonormal bases at various points in the procedure. I have used primed (*e.g.* $\mathbf{P}', \mathbf{K}', \mathbf{d}'$) and unprimed (*e.g.* $\mathbf{P}, \mathbf{K}, \mathbf{d}$) notations to denote the density, KS, and dipole matrices in the AO and orthonormal basis, respectively. Transformation between AO and orthonormal bases is accomplished by the Löwdin[140, 143] symmetric orthogonalization scheme in this work, but other approaches (*e.g.* Cholesky decomposition-based methods[24]) are equally appropriate.

The electronic dynamics of a superposition of mixed plasmonic-excitonic states are investigated herein using RT-TDDFT, in which the initially prepared superposition is propagated by numerical integration of the electronic equation of motion in the density matrix representation (the *Liouville-von Neuman* equation),

$$i\,\frac{\mathrm{d}\,\mathbf{P}(t)}{\mathrm{d}\,t} \;=\; [\,\mathbf{K}(t),\,\mathbf{P}(t)] \tag{4.1}$$

Eq. (4.1) is integrated using a modified midpoint unitary transformation (MMUT)[131, 106] algorithm, in which the density matrix, $\mathbf{P}(t_{n-1})$, is advanced in time through successive similarity transformation by the unitary time-evolution operator in its matrix representation, $\mathbf{U}(t_n)$,

$$\mathbf{P}(t_{n+1}) \;=\; \mathbf{U}(t_n)\cdot\mathbf{P}(t_{n-1})\cdot\mathbf{U}^{\dagger}(t_n). \tag{4.2}$$

$\mathbf{U}(t_n)$ is expressed in the eigenbasis of the KS operator at time t_n,

$$\begin{aligned}\mathbf{U}(t_n) \;&=\; \exp\left[-i\cdot 2\Delta t\cdot\mathbf{K}(t_n)\right]\\ &=\; \mathbf{C}(t_n)\cdot\exp\left[-i\cdot 2\Delta t\cdot\epsilon(t_n)\right]\cdot\mathbf{C}^{\dagger}(t_n),\end{aligned} \tag{4.3}$$

with Δt denoting the size of the discrete time step in the numerical integration.

To probe the time-dependent response of the silver atomic chain to external electric field perturbations, I apply a step-function electric field along the longitudinal direction,

$$\mathbf{E}(t) = \begin{cases} \mathbf{E}_0 & \text{for} \quad t < 0 \\ 0 & \text{for} \quad t \geq 0 \end{cases} \tag{4.4}$$

Computationally this is equivalent to preparing the initial electronic density by a SCF calculation in the presence of the static electric field $\mathbf{E}_0$. After that, I turn off the static electric field, and propagate the electronic system using the RT-TDDFT.

The total dipole moment $\vec{\mu}(t_n)$ is calculated at each time step according to,

$$\vec{\mu}(t) = \mathbf{Tr}[\mathbf{P}'(t) \cdot \mathbf{d}'], \tag{4.5}$$

where $\mathbf{d}'$ is the dipole moment integrals in AO basis. The Mulliken scheme was used to partition the electron density in order to also resolve each atomic chain's contribution to the total dipole moment,

$$\vec{\mu}_1(t) = \mathbf{Tr}[\mathbf{P}'_{11}(t) \cdot \mathbf{d}'_{11}] + \frac{1}{2}\mathbf{Tr}[\mathbf{P}'_{12}(t) \cdot \mathbf{d}'_{12}] + \frac{1}{2}\mathbf{Tr}[\mathbf{P}'_{21}(t) \cdot \mathbf{d}'_{21}], \tag{4.6}$$

where the subscripts on $\mathbf{P}'$ and $\mathbf{d}'$ designate matrix blocks corresponding to basis functions centered on atoms from the different atomic chains.

4.2.2 Simulation Details

The RT-TDDFT simulations were performed using the development version of the GAUSSIAN suite of programs.[74] In all calculations, the BP86 exchange-correlation functional and the LANL2DZ effective core potential and valence basis were used.[95, 96, 220] For real time simulations, the electronic wavepacket was evolved for at least 30 fs with an integration size of 0.05 a.u. (∼1.2 attoseconds).

In this work, I focus on longitudinal excitons in short silver atomic chains, and the decay and transfer of these states brought about by a nearby silver atomic chain in its ground state. Each of the atomic chains considered herein is comprised of six collinear silver atoms with

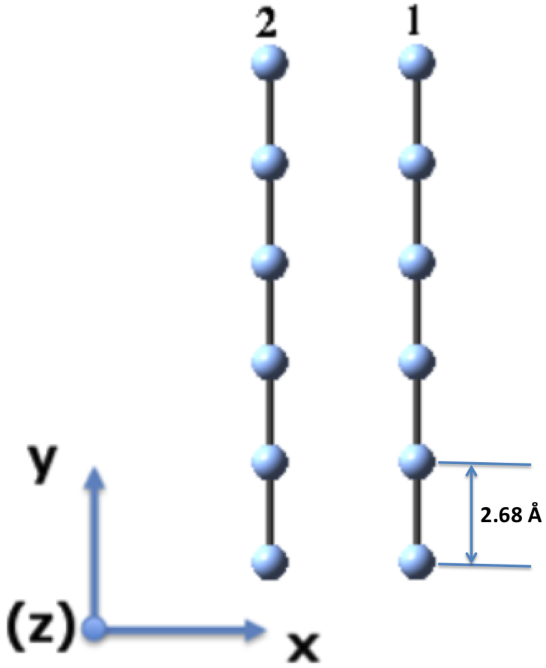

Figure 4.1: Model system: two silver atomic chains in the parallel position.

lattice constant 2.68 Å. I consider an ideal parallel alignment of the atomic chains array as illustrated in Fig. 4.1. The distance between these two atomic chains is chosen in all cases to be greater than the distance separating neighboring atoms in the atomic chain. Thus, I model herein the response of a closed system in a nonequilibrium electronic state that is suddenly exposed to an identical system in its ground (equilibrium) electronic state.

To prepare the initial electron density of the two-chain system at $t = 0$, separate SCF calculations were first carried out on the individual silver atomic chains. In one SCF calculation, a static electronic field with field strength of 0.002 a.u. ($\sim$1 V/nm) was applied to a silver atomic chain along the longitudinal (y in Fig. 4.1) direction, generating the electronic density of the first subsystem $\mathbf{P}'_1$ which is non-stationary in the absence of the external field. All (field-free) electronic eigenstates which exhibit nonzero transition moment (y-component) with the ground state potentially contribute to the field-equilibrated density. A separate

SCF calculation was then carried out to obtain the (field-free) ground-state density of a silver atomic chain, $\mathbf{P}'_2$. Special care was taken to ensure that the density matrix for the second isolated atomic chain corresponds to the orientation of interest with respect to the nuclear coordinates for the atomic chain in the first calculation.

The block-diagonal trial density matrix of the total system was then constructed using the following equation,

$$\tilde{\mathbf{P}}' = \begin{bmatrix} \mathbf{P}'_1 & \mathbf{0} \\ \mathbf{0} & \mathbf{P}'_2 \end{bmatrix} \tag{4.7}$$

This trial density $\tilde{\mathbf{P}}'$ was then transformed to the orthonormal basis $\tilde{\mathbf{P}}$ using the Löwdin orthogonalization procedure. Since $\tilde{\mathbf{P}}'$ is not an idempotent density matrix due to the overlap of orbitals from the two atomic chains, McWeeny purification[153] was applied to construct a physically meaningful initial density,

$$\tilde{\mathbf{P}} = 3\tilde{\mathbf{P}}^2 - 2\tilde{\mathbf{P}}^3. \tag{4.8}$$

Given an initial wave function of the combined system in its desired orientation, RT-TDDFT electronic dynamics described above was used to resolve the time-dependence of the combined density matrix, $\mathbf{P}(t)$, of the two-chain system. The instantaneous dipole moment for the entire system as well as each individual atomic chain's contribution to the total dipole were computed *on-the-fly* using Eqs. (4.5) to (4.6).

4.3 Application to Exciton Dynamics in Silver Atomic Chain

Figure 4.2 plots the absorption spectra as a function of inter-chain separation of silver atomic chain systems illustrated in Fig. 4.1, computed using the LR-TDDFT method.[184, 40, 206] The sharp peak at ∼1.7 eV when two atomic chains are well-separated corresponds to two independent (or uncorrelated) HOMO → LUMO excitations, referred to as the longitudinal excitation.[89, 60] As the inter-chain distance decreases, this longitudinal peak is broadened and red-shifted by the coupling between the low-energy longitudinal modes on each chain in the parallel configuration, arising from the stronger Coulombic interaction between the

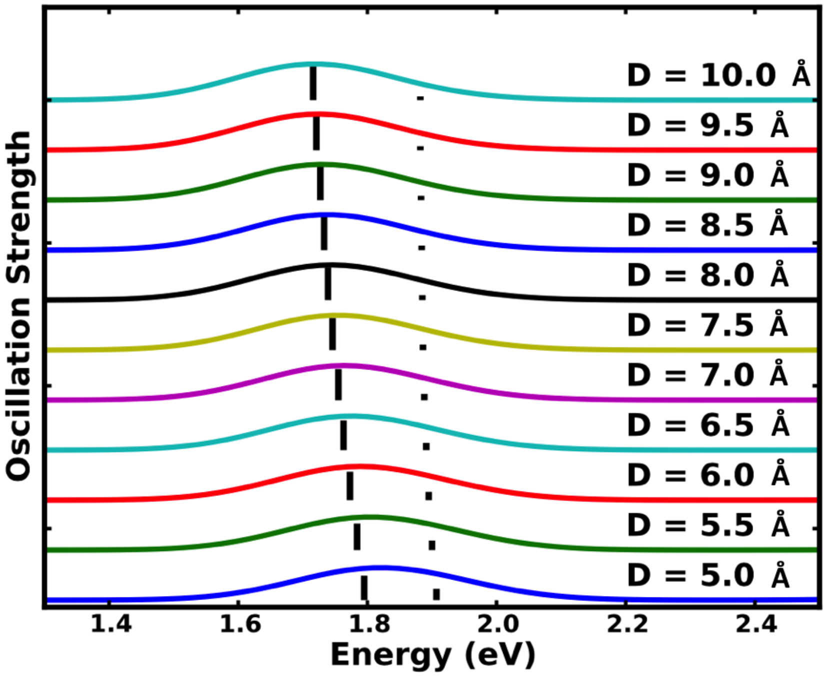

Figure 4.2: Absorption spectra of the two-wire system calculated with the LR-TDDFT. Absorption peaks are broadened with a Gaussian envelope function (FWHM = 0.28 eV).

two closer atomic chain. Figure 4.3 shows the frontier orbitals involved in the longitudinal exciton. The one-electron wave function characteristics smoothly transition from being localized on an individual atomic chain to slightly delocalized across both atomic chains as their separation is decreased. The strong delocalization is analogous to that found in parallel-aligned π-conjugated organic dyes in H-type aggregates.[161] In this work, I focus on analyzing the dynamical properties of excitons in silver atomic chain arrays, with a special emphasis on the decay and transfer characteristics of the exciton. Figure 4.4 shows the

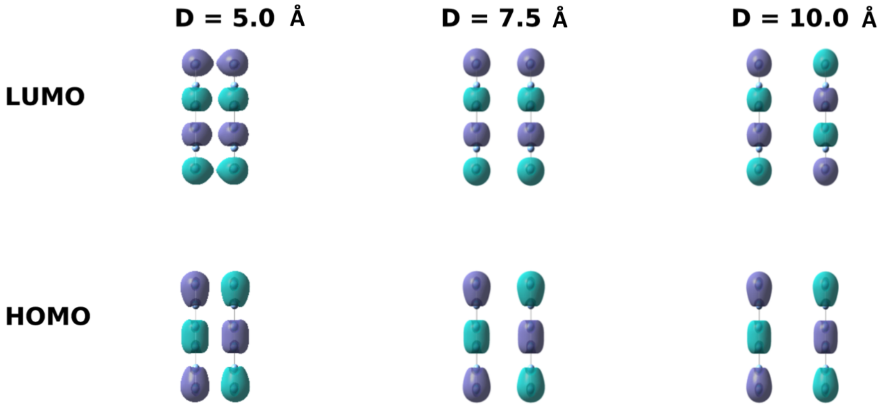

Figure 4.3: Frontier molecular orbitals of two silver atomic chains at inter-chain distances of 5.0 Å, 7.5 Å, and 10.0 Å (iso-value = ± 0.015).

time-dependent dipole moment following the excitonic transition in an isolated silver atomic chain. The time-dependent dipole exhibits persistent oscillatory behavior with no obvious fast decay. As discussed in previous studies of the dynamics of closed quantum systems, this is the expected behavior for a coherent state.[60, 131] Consider, for example, the coherent states of the quantum harmonic oscillator, which show analogous perfectly oscillatory time evolution and recover the classical behavior of a perfect pendulum from within the framework of quantum mechanics. The long-lasting coherence is an artifact of the self-contained many-electron excited state subspace neither interacting with its surroundings nor coupling to the photon field.[60] That is, the time evolution of the excitonic state remains unitary at all times.

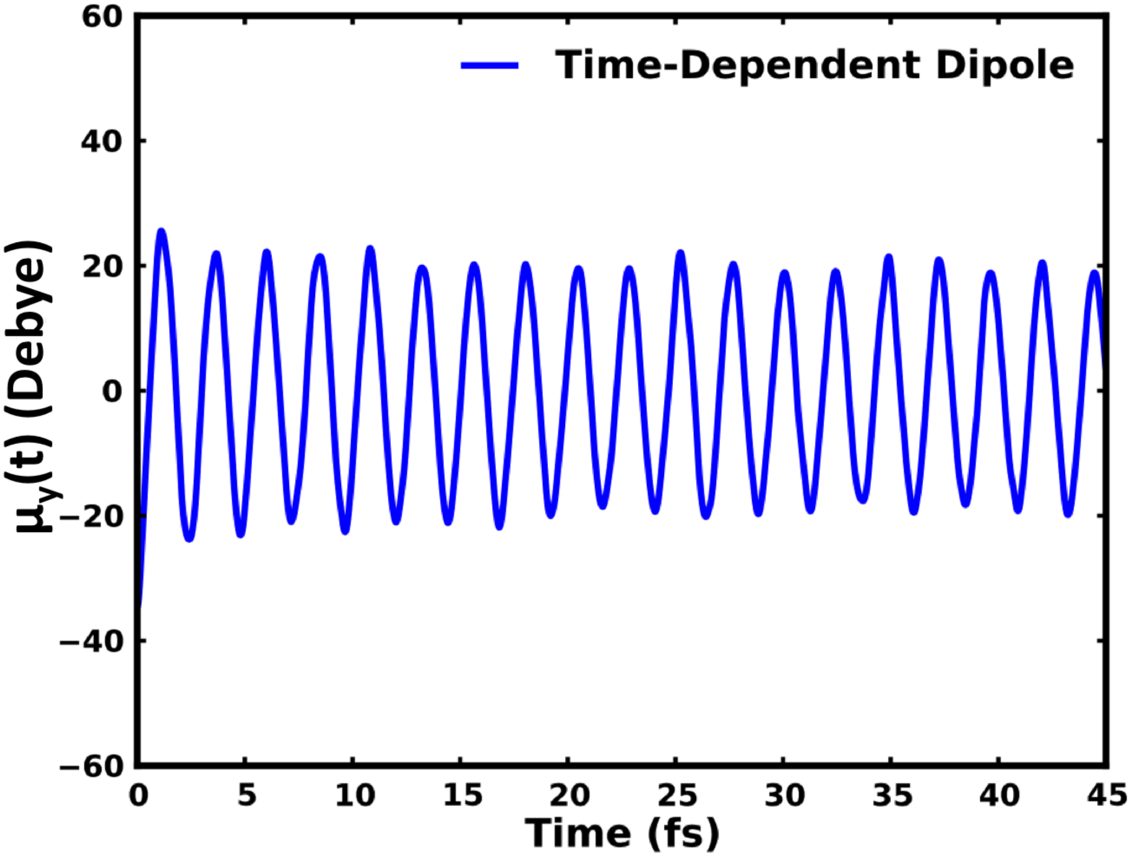

Figure 4.4: Time evolution of the dipole moment in an isolated atomic chain in an excitonic state.

In the absence of a stimulating photon field, the decay and transfer of an excited electronic state can be brought about by perturbations and interactions with other quantized systems (a second silver atomic chain). The preparation of the initial system is illustrated in the Methodology section. The model system shown in Fig. 4.1 will be used to address how the excited electronic states of one atomic chain induces the formation of an exciton in the second atomic chain (*i.e.* exciton transfer) and how their interaction mediates the exciton dephasing. These two properties will be used to estimate the exciton diffusion length in an array of silver atomic chain.

4.3.1 Exciton Transfer

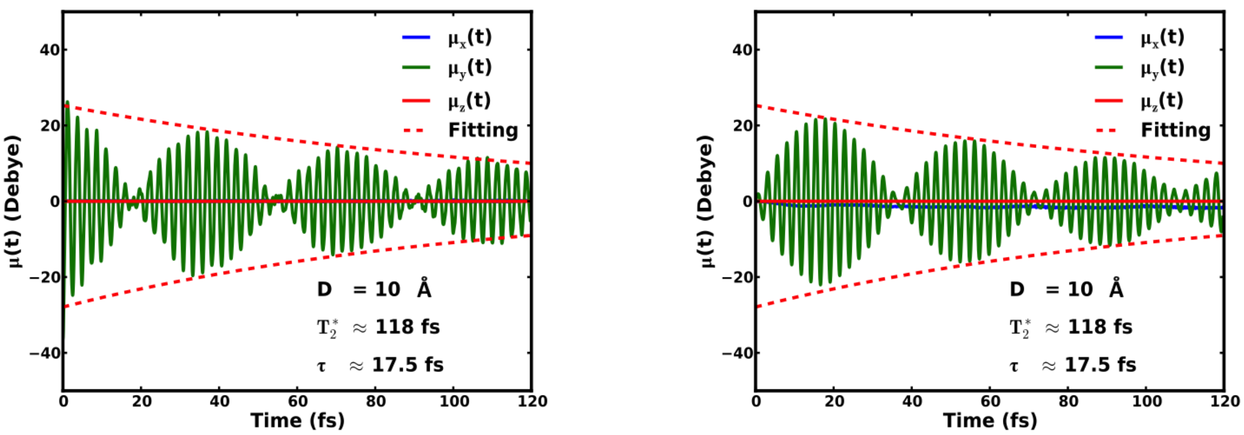

Figure 4.5: Time evolving dipole moments (Cartesian components) in the first (**left**) and second (**right**) atomic chain at an interchain separation distance of 10.0 Å.

Figure 4.5 shows the time evolution of the partial dipole moments of the two silver atomic chains in the system when only one of them is initially excited by the perturbing electric field. The inter-chain distance D is set to 10.0 Å for the simulations shown in Fig. 4.5. In contrast to the electronic dynamics in Fig. 4.4, the presence of the second silver atomic chain in its ground electronic state gives rise to exciton transfer and decay phenomena. Exciton transfer is indicated by the induced dipole oscillation in the second atomic chain whereas exciton decay is suggested by the envelope decay of the dipole oscillation amplitude. Even at such a large separation distance considered in this work, strong dipole oscillations (of equal amplitude to those in the originally excited subsystem) are induced in the second atomic chain. The out-of-phase dipole oscillations in the two atomic chains suggests that the transfer mechanism is predominantly polarization driven as supposed to charge-transfer driven. At

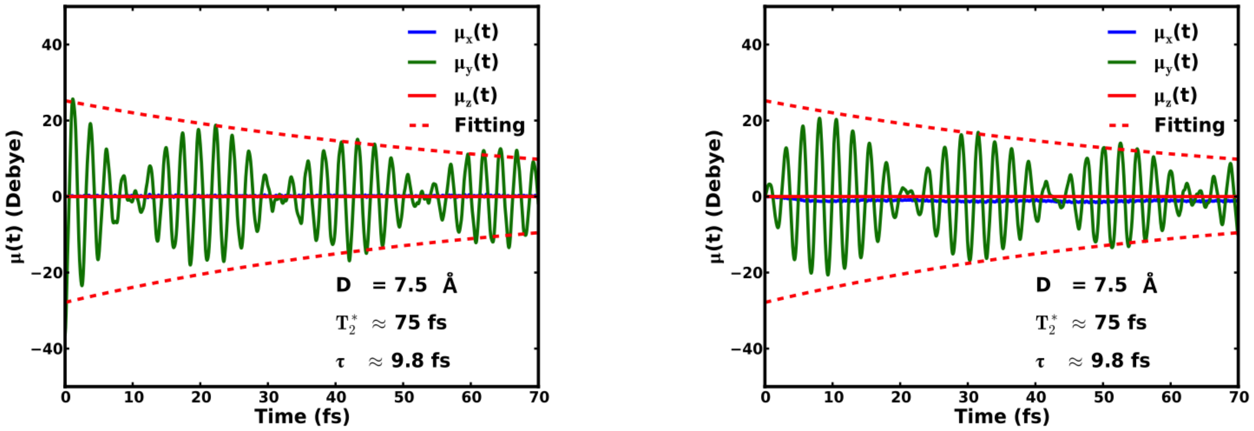

Figure 4.6: Time evolving dipole moments (Cartesian components) in the first (**left**) and second (**right**) atomic chain at an interchain separation distance of 7.5 Å.

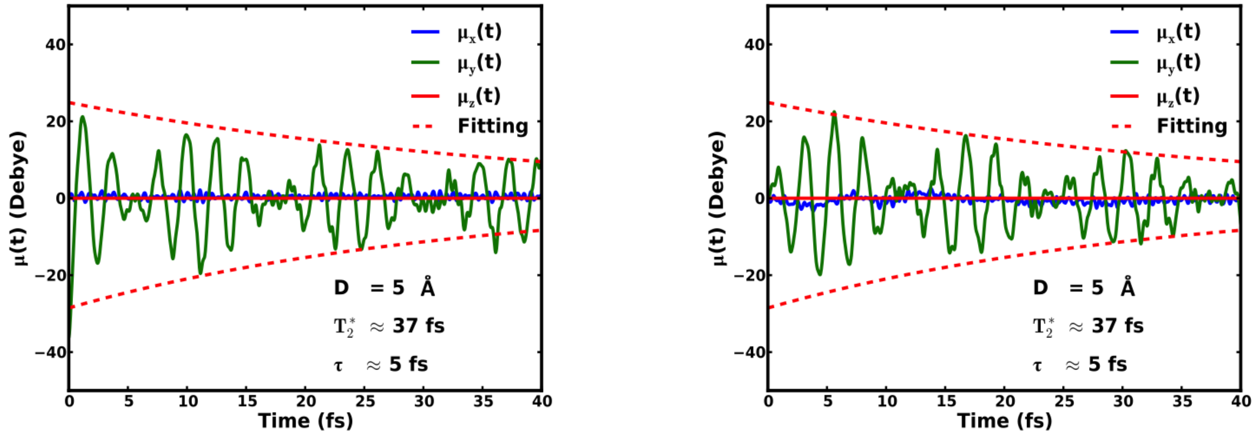

Figure 4.7: Time evolving dipole moments (Cartesian components) in the first (**left**) and second (**right**) atomic chain at an interchain separation distance of 5.0 Å.

∼17.5 fs, when the dipole oscillation in the second atomic chain reaches its peak, the exciton transfer can be considered completed. The time to reach this dipole maximum is used as the exciton transfer time τ between atomic chains to estimate the exciton diffusion length. Given the interchain distance of 10.0 Å, the exciton transfer rate can be estimated to be $r \approx 0.57$ Å/fs.

As the interchain distance decreases, the exciton transfer time also decreases arising from a stronger Coulombic interaction. At the interchain distance of 7.5 Å (Fig. 4.6), the exciton transfer time and transfer rate is estimated to be $\tau \approx 9.8$ fs, and $r \approx 0.77$ Å/fs, respectively. At the interchain distance of 5.0 Å (Fig. 4.7), the polarization induced exciton transfer shows some fine oscillatory structures in the main dipole oscillation. As suggested by the frontier orbitals (Fig. 4.3), there is a small overlap between the MOs in the two atomic chains in this region. As a result, a small amount of charge-transfer character will mix with the polarization driven exciton transfer. Although this is a very interesting region where the two different exciton transfer mechanisms are mixed, analysis of the interplay of different mechanisms is not the focus of the current work. For the interchain distance of 5.0 Å, the exciton transfer time and transfer rate obtained from the simulations are $\tau \approx 5$ fs, and $r \approx 1.0$ Å/fs, respectively.

4.3.2 Exciton Decay

When the second atomic chain is included in the quantum description of the system, the evolution of individual subsystems is no longer necessarily unitary (coherent), but rather the evolution of the system as a whole is subjected to this constraint. Thus, while the TDDFT equation implicitly conserves the coherence of the system as a whole, the constituent subsystems are free to fall out of phase with one another in this formalism.

A decay of the exciton in the initially excited atomic chain and the induced exciton in the second atomic chain is clearly observed in Figs. 4.5 to 4.7. The mechanism of this non-radiative decay can be understood from a fundamental quantum-mechanical vantage point as an instantaneous expansion in the space of electronic states. When the electronic degrees of freedom of the isolated silver atomic chain are perturbed by such a space expansion, new channels are opened for their time-evolution. If sufficient interaction between these two spaces occurs, the electronic wavepackets describing each subsystem will lose their initial phase relationship, leading to a pure dephasing[194] of the non-ground state components of the superposition, characterized by the decay time T_2^*.

The decay of the initial excited state can be interpreted in light of the two-state model problem for which the dephasing process is completely solvable.[194] Skinner and coworkers showed that the the time-evolution of the coherence (off-diagonal density matrix element) for a two-state model system is given by,[194]

$$\rho_{12}(t) = \rho_{12}(0)e^{-i\omega t}e^{-i\Delta\omega t}e^{-t/T_2^*} \tag{4.9}$$

where ω is the energy gap of the two-level system, and $\Delta\omega$ is the shift of ω due to the interaction with a bath. Equation (4.9) also suggests that the amplitude of transition density oscillation decays as an exponential form with a pure dephasing constant of T_2^*. Although the system studied in this work is an atomic chain with many electronic degrees of freedom in non-equilibrium states in the initial condition for the dynamics, the exciton dynamics involves mainly the ground state and the lowest longitudinal excited state. As a result, Eq. (4.9) can be applied to resolve the pure dephasing time constant. By fitting the decay curve observed in Fig. 4.5 to an exponential function, the decay time is estimated to be $T_2^* \approx 118$ fs. This is several orders of magnitude longer than the inverse plasma frequency for bulk silver (the time-scale of the Coulomb screening) which lends credence to the idea that excitons can be significantly longer lived in nanostructures.[164] However, these dephasing rates do not take into account all environmental effects in a realistic supported atomic chain array system. For instance, this study neglects the effects of a dielectric medium surrounding the two-atomic-chain system, as well as the coupling between electronic and nuclear degrees of freedom of the atomic chains.

For ultrafast excited state decay/dephasing phenomena, the quantum aspect of electron-electron interaction is known to dominate the decay process.[80, 81, 82, 83, 173, 57, 237] As the inter-chain distance decreases from 10.0 Å (Fig. 4.5) to 5.0 Å (Fig. 4.7), the excitonic state lifetime (in the originally excited atomic chain) also decreases, from $T_2^* \approx 118$ fs to ≈ 37

fs. This behavior is expected as the electrostatic perturbation from the external quantized system becomes stronger at closer distances. Similar behavior of the strength of plasmon resonances have also been observed in silver nanoparticle dimers.[147, 186]

4.3.3 Exciton Diffusion Length

Exciton transfer rates and lifetimes resulting from the dipole-evolution analysis outlined above are plotted in Fig. 4.8a and Fig. 4.8b. A characteristic property that is crucial for materials design is the effective diffusion length of an exciton before its complete decay to the ground state. Given the exciton transfer rate (r) and lifetime (T_2^*), the effective exciton diffusion length can be computed as $L = T_2^* \times r$. The calculated exciton diffusion length as a function of inter-chain distance is plotted in Fig. 4.8c. In the interaction region considered in this work, the exciton diffusion length increases as the inter-chain distance increases. However, this relationship is not expected to hold asymptotically, i.e. as the interchain distance approaches infinity. At the infinite separation limit, the exciton transfer rate will approach zero. That is, the exciton lifetime remains finite although the pure dephasing mechanism no longer governs the exciton decay. Nevertheless, Fig. 4.8 shows characteristics of exciton dynamics of a silver atomic chain array at intermediate inter-chain separation. The exciton diffusion length is estimated to be ~ 37 Å to ~ 67 Å for the inter-chain distance considered in this work.

4.4 Summary

In this work, I have presented a fully quantum mechanical many-electron dynamical approach to estimate the exciton diffusion length in a silver atomic chain array. This approach is based on the analysis of the exciton transfer and decay in a two silver atomic chain array using the RT-TDDFT electronic dynamics. By following the time evolution of dipole oscillations in the different atomic chains, the exciton transfer and decay rates can be calculated, and the exciton diffusion length estimated. I have studied the characteristic exciton dynamics of a two silver atomic chain array at interchain distances from 5 Å to 10 Å. The exciton

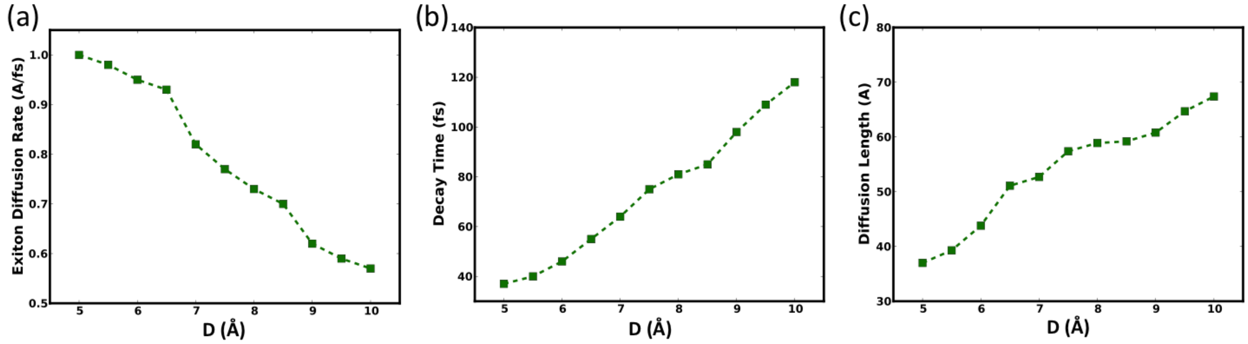

Figure 4.8: Characteristics of exciton transfer in a silver atomic chain array. (**a**) Exciton diffusion rate r as a function of interchain distance D, computed as $r = D/\tau$. (**b**) Exciton decay time T_2^* as a function of interchain distance D, obtained by fitting the dipole oscillation envelope to an exponential function Ae^{-t/T_2^*} . (**c**) Exciton diffusion length L as a function of interchain distance D, computed as $L = T_2^* \times r$.

diffusion length is estimated to be in the range of $\sim$ 37 Å to $\sim$ 67 Å for the inter-chain distances considered herein. In this work, I only considered the pure dephasing mechanism, ignoring the immensely complicated effect of phonon-exciton coupling on the exciton decay mechanism. As a result, the exciton decay time is an estimated upper bound.

Chapter 5

ENERGY-SPECIFIC EQUATION-OF-MOTION COUPLED-CLUSTER (EOM-CC) METHOD FOR HIGH-ENERGY EXCITED STATES

Single-reference techniques based on CC theory, in the forms of LR- or EOM-, are highly accurate and widely used approaches for modeling valence absorption spectra. Unfortunately, these equations with singles and doubles (LR-CCSD and EOM-CCSD) scale as $\mathcal{O}(N^6)$, which may be prohibitively expensive for the study of high-energy excited states using a conventional eigensolver. In this chapter, I present an energy-specific non-Hermitian eigensolver that is able to obtain high-energy excited states, *e.g.* XAS K-edge spectrum, at low computational cost. In addition, I also introduce an improved trial vector for iteratively solving the EOM-CCSD equation with a focus on high-energy eigenstates. The energy-specific EOM-CCSD approach and its low-scaling alternatives are applied to calculations of carbon, nitrogen, and oxygen K-edge excitations, as well as sulfur K-edge excitations. The results are compared to other implementations of CCSD for excited states, energy-specific LR-TDDFT, and experimental results with multiple statistical metrics presented and evaluated.

5.1 Introduction

Advances in laser light sources have made X-ray absorption spectroscopy (XAS) a powerful tool in modern-day chemical research. In XAS, excitations of core electrons to either weakly bound or continuum states can be used to characterize electronic and molecular structure of a chemical or material system.[205] Excitations to bound states provide information about the valence electronic structure while the scattering of the photoelectron generated by excitation to continuum states provides information about the molecular geometry. The ability to simultaneously probe both electronic and nuclear degrees of freedom has made XAS an irreplaceable tool in the fields of surface science[234, 205, 8] and inorganic catalysis.[191, 63, 45]

Due to its complexity, XAS often relies on theoretical insight for interpretation. As in lower-energy absorption spectroscopy, variants of time-dependent density functional theory (TDDFT) [40, 206, 62] are the most frequently used methods. The restricted excitation window (REW-TDDFT) [203, 176, 27, 139] and energy-specific (ES-TDDFT)[135, 139, 128] TDDFT approaches are now routinely used to model XAS. The REW-TDDFT method restricts solutions to only include transitions from orbitals deemed relevant to a particular region of the spectrum, whereas the ES-TDDFT approach searches for solutions in the full orbital space with a constraint on the eigenvalues. These two different numerical approaches have been shown to produce nearly identical X-ray K-edge spectra because excitations from the $1s$ (K-edge) orbital are rather localized in the orbital space.[5] Variations of the ΔSCF approach[14], such as the transition-potential DFT[195, 213] and the orthogonality-constrained DFT[69, 59], which require the preparation of a core-hole single determinant state, have been successfully applied to X-ray absorption spectroscopy. From the DFT kernel perspective, there has also been interest in developing short-range corrected functionals that improve the description of core correlation and reduce the self-interaction error specifically for XAS.[196, 29]

Wave function-based approaches, while more expensive, are inherently free of the self-interaction error and can be systematically improved. For example, single-reference techniques based on CC theory, in the forms of LR-[163, 116] or EOM-[198, 51], are highly accurate and widely used approaches for modeling valence absorption spectra.[54, 192] Unfortunately, these equations with singles and doubles (LR-CCSD and EOM-CCSD) scale as $\mathcal{O}(N^6)$, which may be prohibitively expensive for the study of large molecular systems. This high computational cost has prompted the development of many low-scaling approximations to EOM-CCSD and LR-CCSD. The EOM second-order many-body perturbation theory (EOM-MBPT2) equation is obtained by truncating the perturbative expansion of the cluster operator at second-order.[199, 79] This approach still scales as $\mathcal{O}(N^6)$ but with a much smaller prefactor than that of EOM-CCSD. Partitioned EOM-MBPT2 (P-EOM-MBPT2) is an iterative $\mathcal{O}(N^5)$ approach that makes the further approximation that the doubles-doubles block of the Hamiltonian can be treated as diagonal.[93, 92, 79] While these techniques have been extensively used in obtaining low-lying excited states, they have not been applied to the study of core excitations, although further approximations to these techniques have been used previously with varying success.

Beyond CC, there are other wave function- and Green's function-based methods to study high-energy excited states. The CIS(D_∞) approach can be related to P-EOM-MBPT2 by treating the singles-doubles blocks of the Hamiltonian to first-order only.[98] The second-order algebraic-diagrammatic construction approach (ADC(2)) is a symmetrized form of CIS(D_∞) that has been previously used to model XAS.[214, 215, 172] The core-valence separation approximation (CVS)[44] is employed to reduce the dimension of the problem by only including excitations from the relevant core orbitals, however, there is an estimated 0.5-1.0 eV error associated with the CVS approximation.[215] The closely related CIS(D) method applies a non-iterative doubles correction to excitation energies obtain from CIS.[71, 97] By using the REW approach, CIS(D) can be used to model core excitations, but has been known to provide qualitatively incorrect spectra in some cases.[6].

Where core excitations are concerned, direct applications of EOM-CCSD and its closely-related derivatives are computationally intractable due to the large space where the excited states of interest reside. The electron-attachment EOM-CCSD (EA-EOM-CCSD)[165] has been used previously to investigate K-edge transitions in small molecules, relying on the validity and availability of a core-hole reference state. Recently, an equation-of-motion multi-reference CC including singles and doubles (EOM-MRCCSD) has been developed to obtain core excitations in the CC framework.[31, 189, 64] The EOM-MRCCSD approach for XAS is based on construction of a core-hole reference in a select subspace spanned by active core, occupied, and unoccupied spin-orbitals of interest. Recently, a complex polarization propagator formulation of CC response theory (CPP-CC) has been applied to model X-ray absorption among other properties.[52, 73, 112] This formalism can be used for many different CC approaches truncated at different levels (CCS, CC2, CCSD, CCSD(3)). Unlike EOM-CC which solves for resonant frequencies or poles of the response function, the CPP-CC method solves a damped frequency-dependent response function. This technique is able to resolve the off-resonant response of the system, but requires the solution of many frequency-dependent problems.

In this chapter, I present an energy-specific non-Hermitian eigensolver with improved trial vectors to efficiently solve the EOM-CCSD equation for high-energy core excitations. This approach utilizes low-scaling approximations of EOM-CCSD to refine trial vectors, followed by iterative eigenvalue-screening, eigenvector-bracketing and growing window techniques to search for high-energy solutions in the full orbital space. The strategy used throughout is a non-Hermitian generalization of the previously developed energy-specific algorithm applied in TDDFT.[135] This strategy will allow these highly accurate single-reference wave function methods to be routinely applied to the study of core excitations.

5.2 Methodology

5.2.1 Brief Review of EOM-CCSD, EOM-MBPT2 and P-EOM-MBPT2

For two excellent articles of CC theory, see the review by Crawford and Schaefer[54] and the book by Shavitt and Bartlett[192]. In the present work I adopt the notation that indices i, j, k, l refer to occupied orbitals, a, b, c, d refer to virtual orbitals, and p, q, r, s refer to any orbital.

The generalized CC Schrödinger equation may be written as

$$\bar{H}\,\hat{R}(m)\,|\Phi_0\rangle = E_m\,\hat{R}(m)\,|\Phi_0\rangle, \tag{5.1}$$

where $|\Phi_0\rangle$ is the reference wave function, and $\hat{R}(m)$ is the excitation operator for the m-th excited state with energy E_m. This takes the form,

$$\hat{R}(m) = \hat{R}_1 + \hat{R}_2 + \ldots = \sum_{ia} r_i^a(m)\,a_a^\dagger a_i + \sum_{\substack{i<j\\a<b}} r_{ij}^{ab}(m)\,a_a^\dagger a_b^\dagger a_j a_i + \ldots, \tag{5.2}$$

where $a^\dagger$ and a are creation and annihilation operators. $\bar{H}$ is the similarity transformation of the bare electronic Hamiltonian $\hat{H}$,

$$\bar{H} = e^{-\hat{T}}\,\hat{H}\,e^{\hat{T}}, \tag{5.3}$$

in which the cluster operator $\hat{T}$ takes the following form,

$$\hat{T} = \hat{T}_1 + \hat{T}_2 + \ldots = \sum_{ia} t_i^a\, a_a^\dagger a_i + \frac{1}{4}\sum_{ijab} t_{ij}^{ab}\, a_a^\dagger a_b^\dagger a_j a_i + \ldots. \tag{5.4}$$

Equation (5.1) represents a right-hand eigenvalue problem, however, Eq. (5.3) makes $\bar{H}$ non-Hermitian. As a result, Eq. (5.1) is different from its associated left-hand eigenvalue problem,

$$\langle\Phi_0|\,\hat{L}(m)\,\bar{H} = \langle\Phi_0|\,\hat{L}(m)\,E_m. \tag{5.5}$$

where $\hat{L}(m)$ is the de-excitation operator defined as,

$$\hat{L}(m) = \hat{L}_1 + \hat{L}_2 + \ldots = \sum_{ia} l_a^i(m)\, a_i^\dagger a_a + \sum_{\substack{i<j\\ a<b}} l_{ab}^{ij}(m)\, a_i^\dagger a_j^\dagger a_b a_a + \ldots. \tag{5.6}$$

Note that Eq. (5.1) and Eq. (5.5) share the same eigenvalues (E_m) and the left-hand and right-hand eigenvectors are related to each other through the biorthonormality condition,

$$\langle\Phi_0|\,\hat{L}(m)\,\hat{R}(n)\,|\Phi_0\rangle = \delta_{m,n}, \quad m \neq 0 \text{ and } n \neq 0 \tag{5.7}$$

such that the generalized CC energy expression can be obtained,

$$E_m = \langle\Phi_0|\,\hat{L}(m)\,\bar{H}\,\hat{R}(m)\,|\Phi_0\rangle. \tag{5.8}$$

In order to calculate electronic excitation energies, it is convenient to define a normal-ordered Hamiltonian, $\bar{H}_N$, by

$$\bar{H}_N = \bar{H} - E_0, \tag{5.9}$$

where E_0 is the energy associated with the ground-state wave function $|\Phi_0\rangle$. Then, Eq. (5.8) can be rewritten as

$$\omega_m = \langle\Phi_0|\,\hat{L}(m)\,\bar{H}_N\,\hat{R}(m)\,|\Phi_0\rangle \tag{5.10}$$

where ω_m is the m-th excitation energy.

Within the framework of EOM-CCSD method, $\hat{L}$ and $\hat{R}$ are truncated to the second order, and the excitation energies are obtained by diagonalizing the EOM-CCSD Hamiltonian matrix,

$$\mathbf{H}_{EOM-CCSD} = \begin{bmatrix} \bar{\mathbf{H}}^{SS} & \bar{\mathbf{H}}^{SD} \\ \bar{\mathbf{H}}^{DS} & \bar{\mathbf{H}}^{DD} \end{bmatrix} \tag{5.11}$$

$$\begin{aligned} \bar{H}^{SS}_{ai,ck} &= \langle \Phi_i^a | \, \bar{H}_N \, |\Phi_k^c\rangle \\ \bar{H}^{SD}_{ai,cdkl} &= \langle \Phi_i^a | \, \bar{H}_N \, \left|\Phi_{kl}^{cd}\right\rangle \\ \bar{H}^{DS}_{abij,ck} &= \left\langle \Phi_{ij}^{ab} \right| \bar{H}_N \, |\Phi_k^c\rangle \\ \bar{H}^{DD}_{abij,cdkl} &= \left\langle \Phi_{ij}^{ab} \right| \bar{H}_N \, \left|\Phi_{kl}^{cd}\right\rangle \end{aligned}$$

where $|\Phi_k^c\rangle, \left|\Phi_{kl}^{cd}\right\rangle$ are singly and doubly excited determinants, respectively. The overall dimension of Eq. (5.11) is $OV + O^2V^2$ where O and V are the numbers of occupied and virtual orbitals. EOM-CCSD scales as $\mathcal{O}(N^6)$, and a lower-scaling approximation can be obtained by only keeping terms in the perturbative expansion of the cluster operator through second order. This gives rise to the EOM-MBPT2 Hamiltonian matrix,[199, 93, 92]

$$\mathbf{H}_{EOM-MBPT2} = \begin{bmatrix} \bar{\mathbf{H}}^{SS(2)} & \bar{\mathbf{H}}^{SD(2)} \\ \bar{\mathbf{H}}^{DS(2)} & \bar{\mathbf{H}}^{DD(2)} \end{bmatrix}, \tag{5.12}$$

where $\bar{\mathbf{H}}^{SS(2)}$ is the singles-singles block of the Hamiltonian, $\bar{\mathbf{H}}_{SS}$, through second order, and so on. This approximation neglects the numerous $\hat{T}_1$ terms, as $\hat{T}_1^{(1)}$ equals zero in the perturbative approach, and only needs the $\hat{T}_2^{(1)}$ amplitudes, which are determined through

$$t_{ij}^{ab\,(1)} = \frac{\langle i\, j \,\| a\, b\rangle}{\epsilon_i + \epsilon_j - \epsilon_a - \epsilon_b}, \tag{5.13}$$

where ϵ's are the Hartree-Fock molecular orbital energies.

EOM-MBPT2 is still a $\mathcal{O}(N^6)$ method, but with a much smaller prefactor than EOM-CCSD. Further approximation can be made by replacing $\bar{\mathbf{H}}^{DD(2)}$ with its zeroth order based on Löwdin partitioning approach[141] to give rise to an iterative $\mathcal{O}(N^5)$ method, the so-called partitioned EOM-MBPT2 (P-EOM-MBPT2).[93, 92, 141] The P-EOM-MBPT2 Hamiltonian is

$$\mathbf{H}_{P-EOM-MBPT2} = \begin{bmatrix} \bar{\mathbf{H}}^{SS(2)} & \bar{\mathbf{H}}^{SD(2)} \\ \bar{\mathbf{H}}^{DS(2)} & \bar{\mathbf{H}}^{DD(0)} \end{bmatrix}, \tag{5.14}$$

where $\bar{\mathbf{H}}^{DD(0)} = \epsilon_a + \epsilon_b - \epsilon_i - \epsilon_j$.

In practice, due to the non-Hermitian nature of Hamiltonians in Eq. (5.11), Eq. (5.12), and Eq. (5.14), and their large matrix dimension (roughly O^2V^2), the most efficient computational approach to find the lowest eigenvalues and corresponding left and right eigenvectors is a modified version of the Davidson algorithm. [56, 103, 37, 179] However, core excitations in XAS usually exhibit high excitation energies ranging from hundreds to thousands eV, and are thus far away from low-lying excited states. It is then impractical for the conventional EOM methods mentioned above to capture these high-energy excited states because ordinary solvers require that all lower-energy solutions be obtained before any higher-energy solution.

5.2.2 Improved Trial Vectors for High-Energy Excited States

Davidson-like eigensolvers usually initialize with a set of well-defined guess vectors, and the quality of these guess vectors subsequently affects the convergence speed in iterative methods for eigenvalue problems. In TDDFT, trial vectors constructed from simple occupied-to-virtual orbital transitions have proven to be quite reasonable. However, such trial vectors are usually far from the converged EOM-CCSD solution and as a result they may lead to excessive iterations with Davidson-like eigensolvers. A better and widely used trial vector scheme for EOM-CCSD in practice starts with the solution of configuration interaction singles (CIS). However, generating trial vectors for high-energy excited states using conventional CIS calculations is impractically expensive with conventional techniques. As a result, the feasibility of applying the EOM-CCSD approach for XAS calculations depends on the availability of appropriate trial vectors and efficient solvers that can obtain the high energy eigenvectors of interest. In this work, I develop a two-step strategy to generate appropriate trial vectors that aims to enable EOM-CCSD and its low-scaling approximations to study high-energy excitations such as those probed by XAS.

Assume that M excited states with energies greater than ω_0 are the subject of interest to be investigated using EOM-CCSD. In the first step, high-energy trial vectors are generated using the energy-specific eigensolvers with low-scaling excited-state methods such as CIS and P-EOM-MBPT2. For CIS, the Hermitian energy-specific algorithm[135] is used to obtain m eigenvectors ($m \geq M$, $\omega \geq \omega_0$) as trial vectors for the following calculation. As the CIS approach does not have electron correlation, their eigenvectors can be poor guesses for high-energy excited states as contributions from $\hat{T}_2$ become more important.[79] In fact, in the test cases, searching for high-energy eigenvectors in EOM-CCSD framework usually takes many more iterations compared to those for valence excitations. Any improvement to expedite solving the EOM-CCSD equations for high-energy excited states will be appreciated.

To improve the CIS vectors for high-energy EOM-CCSD calculations, I introduce a second step to refine the trial vectors using the $\mathcal{O}(N^5)$ P-EOM-MBPT2 approach with a non-Hermitian energy-specific eigensolver which will be introduced later in this paper. The refined trial vectors will be used together with the non-Hermitian energy-specific eigensolver to obtain solutions of the EOM-CCSD equation. In the following discussion, methods that utilize the energy-specific eigensolver (Hermitian or non-Hermitian) will have the "ES-" prefix in order to distinguish the results from those using conventional algorithms.

Figure 5.1 shows the effect of the quality of different trial vectors on the convergence behavior of an ES-EOM-CCSD calculation of a carbon K-edge excitation of CO. Two different tight convergence criteria, the residual norm and the change in excitation energy, are considered in this comparison. For both criteria, EOM-CCSD using the P-EOM-MBPT2 eigenvectors as trial vectors exhibits ∼20% savings in computational cost. Note that the cost of computing ES-P-EOM-MBPT2 eigenvectors is trivial compared to the cost of solving $\mathcal{O}(N^6)$ EOM-CCSD equation. This test case suggests that P-EOM-MBPT2 eigenvectors are a better choice over the CIS trial vectors for ES-EOM-CCSD calculations.

5.2.3 Non-Hermitian Energy-Specific Eigensolver

In this work, I introduce a non-Hermitian energy-specific eigensolver for EOM-CCSD and its low-scaling approximations to efficiently compute high-energy excited states. The discussion starts with a set of left $\mathbf{L} = \{L_1, \ldots, L_m\}$ and right $\mathbf{R} = \{R_1, \ldots, R_m\}$ trial vectors in the full orbital space that correspond to initial guesses of high-energy excited states generated using the two-step strategy presented above. Note that the left and right vectors are related by the biorthonormalization condition (Eq. (5.7)). The EOM Hamiltonian $\mathbf{H}$, Eq. (5.11), is projected onto the subspace spanned by the trial vectors,

$$\mathbf{h} = \mathbf{L}^{\dagger}\mathbf{H}\mathbf{R} \tag{5.15}$$

The EOM Hamiltonian in the reduced space, $\mathbf{h}$, is then diagonalized to obtain a new set of left $\mathbf{l} = \{l_1, \ldots, l_m\}$ and right $\mathbf{r} = \{r_1, \ldots, r_m\}$ eigenvectors and eigenvalues $\boldsymbol{\omega} = \{\omega_1, \ldots, \omega_m\}$. Eigenpairs in the reduced space are screened and only the ones with associated eigenvalues above the desired energy threshold ω_0 are kept. The transformation of these qualified eigenpairs from the reduced space to the full orbital space yields the new approximate eigenvectors,

$$\tilde{\mathbf{R}} = \mathbf{R}\mathbf{r}, \qquad \tilde{\mathbf{L}} = \mathbf{L}\mathbf{l}. \tag{5.16}$$

Equation (5.7) is used to ensure the new left and right eigenvectors are biorthonormalized. To test the convergence, the eigenvector residuals of states of interest are computed

$$\Delta R_k = \left(\mathbf{H} - \mathbf{I}\omega_k\right) R_k \tag{5.17}$$

$$\Delta L_k = \left(\mathbf{H}^{\dagger} - \mathbf{I}\omega_k\right) L_k \tag{5.18}$$

If some of the norms of residuals are still above the pre-defined threshold, perturbation vectors are generated using the following equation,

$$R'_k = \left(\mathbf{I}\omega_k - \mathbf{H}_D\right)^{-1} \Delta R_k \tag{5.19}$$

$$L'_k = \left(\mathbf{I}\omega_k - \mathbf{H}_D\right)^{-1} \Delta L_k \tag{5.20}$$

where $\mathbf{H}_D$ are the diagonal elements of the $\mathbf{H}$ matrix.[56, 103] In this implementation, as in previous studies,[37, 222] $\mathbf{H}_D$ is approximated by the corresponding orbital energy differences. The perturbation vectors are biorthonormalized and added to $\mathbf{R}$ and $\mathbf{L}$ to form the new subspace for the next iteration starting from Eq. (5.15). If complex eigenvalues are obtained in the intermediate iteration, the space of $\mathbf{R}$ and $\mathbf{L}$ needs to be increased. The larger number of expansion vectors can not only benefit the elimination of complex eigenvalues, but also help to accelerate the convergence.[206, 37] This process is repeated until the norm of the residuals are below the desired threshold.

The two-step calculation strategy and energy-screening and eigenvector-bracketing technique introduced above avoids the scan through low-lying excited states in EOM calculations, as well as improving the quality of trial vectors for EOM-CCSD calculation by using converged eigenvectors associated with the high excited states from low-scaling EOM calculations. This makes it possible to calculate high-energy excited states with CC theory.

5.3 Application to K-edge Core Excitations

Energy-specific variations of EOM-CCSD, EOM-MBPT2, and P-EOM-MBPT2 have been implemented and tested in a development version of the Gaussian software package.[74] For all excited-state calculations, the convergence is obtained when (i) the norm of the residual vectors is below a threshold, 10^{-5} a. u., as recommended by Stanton and Bartlett;[198] or (ii) the change in the eigenvalues is less than 10^{-7} a.u.[37] All ground state geometries were optimized at the CCSD level with the def2-TZVPD basis set.[224, 175, 70, 188] As discussed in the Method section, the energy-specific eigensolver is able to obtain the exact solutions represented in the full space. This has been verified by benchmark calculations on select excited states using the ES-EOM-CCSD method compared to those obtained by full EOM-CCSD calculations including low-lying states. In Tab. 5.1, the results from ES-EOM-CCSD and EOM-CCSD are numerically identical, suggesting that the energy-specific approach is able to obtain the exact excited states even though low-lying states are not considered in the eigenvector search algorithm. As the full EOM-CCSD calculation has to include extra low-

Table 5.1: Comparison of conventional EOM-CCSD and ES-EOM-CCSD for select low-lying excited states of carbon monoxide computed with the def2-TZVPD basis set (eV). The energy threshold for the energy-specific calculations is 11.2 eV.

State	Transition	ES-EOM-CCSD	EOM-CCSD
B $^1\Sigma^+$	$\sigma \rightarrow 3s$	11.27	11.27
C $^1\Sigma^+$	$\sigma \rightarrow 3p\sigma$	12.30	12.30
E $^1\pi$	$\sigma \rightarrow 3p\pi$	12.32	12.32
F $^1\Sigma^+$	$\sigma \rightarrow 3d\sigma$	13.53	13.53

lying states in order to locate the states in the targeted energy range, it unavoidably incurs additional two-fold computational cost compared to the ES-EOM-CCSD method in this test case. Assuming the number of excited states (i.e. the number of $\mathbf{R}$ and $\mathbf{L}$ vectors) grows linearly with respect to the excitation energy, the computational cost of each EOM-CCSD iteration will grow linearly with respect to the energy of the targeted states. For core-electron excitations, the cost of the conventional EOM-CCSD approach becomes intractable. In contrast, the computational cost of ES-EOM-CCSD is nearly constant because the search space is in principle invariant to the excitation energy range of interest.

The quality of ES-EOM-CCSD approach is also compared to other implementations and/or approximations of CC method to XAS. Table 5.2 compares oxygen K-edge excitations of H_2O obtained using ES-EOM-CCSD to those computed using multi-reference EOM-MRCCSD[31, 189, 64] method and single-reference CPP-CCSD[111] method. Table 5.3 compares K-edge excitations of a select test set obtained using ES-EOM-CCSD to another single-reference method, EA-EOM-CCSD[165]. This comparison shows that, for the limited number of test cases, ES-EOM-CCSD results are in excellent agreement with the results from other CC methods. The difference between ES-EOM-CCSD and EA-EOM-CCSD can be attributed to the different reference used in the calculation. The EA-EOM-CCSD method requires a pre-defined core-hole reference that includes a certain amount of core-hole relaxation effect. Therefore, the EA-EOM-CCSD results can be of higher accuracy, although they strongly depends on the quality of the core-hole reference.

Excitation energies of a set of 31 K-edge transitions for carbon, nitrogen, and oxygen, of seven molecules (CO, CH_2O, C_2H_4, N_2, NH_3, NO_2, H_2O) are calculated with ES-EOM-CC methods (see Tab. 5.4). The results are compared with results from gaseous XAS or inner-shell electron energy loss spectroscopy (ISEELS) experiments.[185, 178, 61, 174, 193, 1, 216] The mean absolute/signed error (MAE/MSE), root mean square (RMS) error, maximum absolute error (Max AE), and standard deviation (StDev) of the errors with respect to experimental results are statistically evaluated. Energy-specific TDDFT (ES-TDDFT)[135] results are also included for comparison. Two density functionals, BHandHLYP[23] and PBE1PBE[2, 170] were used as they have been shown to consistently perform well for predicting K-edge spectra.[128]

Table 5.5 lists error analyses of absolute and shifted K-edge excitation energies (300-500 eV for these systems) obtained with different methods and the doubly augmented Dunning basis with flexible core orbitals (d-aug-cc-pCVDZ).[230, 231] While absolute excitation energies are direct measurement of the accuracy of a method, uniform shifts are often applied to calculated XAS to account for the lack of relativistic effects and higher-order correlations.[27, 58, 75] For error analyses of shifted results, the calculated excitation energies are uniformly shifted so that the lowest-energy transition matches the corresponding experimental value. Errors are calculated using the remaining transitions.

DFT methods (BHandHLYP and PBE1PBE) consistently underestimate absolute K-edge excitation energies, whereas wave function-based methods overestimate the K-edge excitations. The ES-BHandHLYP method surprisingly outperforms even ES-EOM-CCSD. This is due to fortuitous error cancellation in BHandHLYP functional which includes 50%

of HF exchange that shifts the spectra to the opposite sign compared to those from pure functionals.[128] For details regarding the performance of ES-TDDFT on XAS calculations, I refer readers to Ref. [128].

After the K-edge excitation energies are shifted, the associated errors change significantly. All methods considered herein become more reliable with MAEs of < 1 eV with standard derivation < 0.5 eV. ES-EOM-CCSD shows the best performance in all statistical metrics. It consistently overestimates K-edge excitation energies only by 0.2-0.3 eV. The lower-scaling alternatives of ES-EOM-CCSD, as represented by ES-EOM-MBPT2 and ES-P-EOM-MBPT2, also show a consistent overestimation with slightly larger errors, yet still outperform DFT-based methods. Note that the difference between these low-scaling methods and ES-EOM-CCSD is much greater for these core excitations than for valence and Rydberg excitations.[79] Although inclusion of triples has shown to be able to improve the CPP-CCSD results to be within 0.5 eV of the experimental values for Ne, CO, and H_2O,[111] it is formally a $\mathcal{O}(N^7)$ method which is outside the consideration of this work. I also applied the energy-specific method to the calculation of the K-edge excitation of heavier elements (*e.g.* sulfur) in organic molecules. Fig. 5.2 shows the structure of an organic molecule, dibenzolthiophene, used in the test. For DBT, the sulfur K-edge X-ray absorption spectrum shows a main peak at about 2472 eV and resonance at about 2474 eV, corresponding to sulfur $1s \rightarrow 3p$ excitations.[159] Tab. 5.6 shows the calculated results obtained with different energy-specific methods. In contrast to what I have seen for small molecules, TDDFT with the as-investigated two functionals, PBE1PBE and BHandHLYP severely underestimate the excitations by 20-50 eV, while EOM-CCSD and its perturbative approximations only underestimate the experimental values no more than 2 eV. After the excitation energies are shifted, all the as-investigated energy-specific methods give close results to the experimental value, but the EOM-CCSD and its two perturbative approximations still slightly outperform TDDFT. Note that the presented calculations neglect the relativistic effect, which, in contrast to small molecules, is significant in DBT, and may bring a blue shift of as large as $\sim$7 eV to the calculated excitation energies.[159] However, this blue shift can be partially compromised by introducing larger basis set, and including triples and higher determinants in the CC method. For example, Fransson et al. [73] found that, for ethene and its fluoro derivatives, a red shift of ∼1.3 eV needs to be applied to account for basis set incompleteness for a correlation-consistent double-ζ basis set, and a red shift of about 0.5 eV for triple corrections for CCSD method.

5.4 Summary

In this work, I presented a strategy using the low-scaling P-EOM-MBPT2 approach to improve the trial vectors for solving EOM-CCSD equation with an emphasis on the high-energy excited states, *e.g.* core-electron excitations. An energy-specific non-Hermitian Davidson eigensolver, facilitated by the energy-screening, eigenvector-bracketing, and growing window techniques, has been developed to efficiently obtain high-energy solutions without scanning through low-energy states. With these advances, EOM-CCSD and its low-scaling alternatives can be directly used to compute XAS. Applications to carbon, nitrogen, and oxygen K-edge XAS of various modules show that after uniform spectral shift, ES-EOM-CCSD outperforms DFT and low-scaling alternatives in all statistical metrics with an average overestimation of only 0.2∼0.3 eV. Further application of energy-specific methods to DBT molecule shows excellent agreement with the experiment. As an extension to this research, a second-order approximation of CCSD, CC2,[48] has also been implemented and tested. Relevant information can be found in Appendix E.

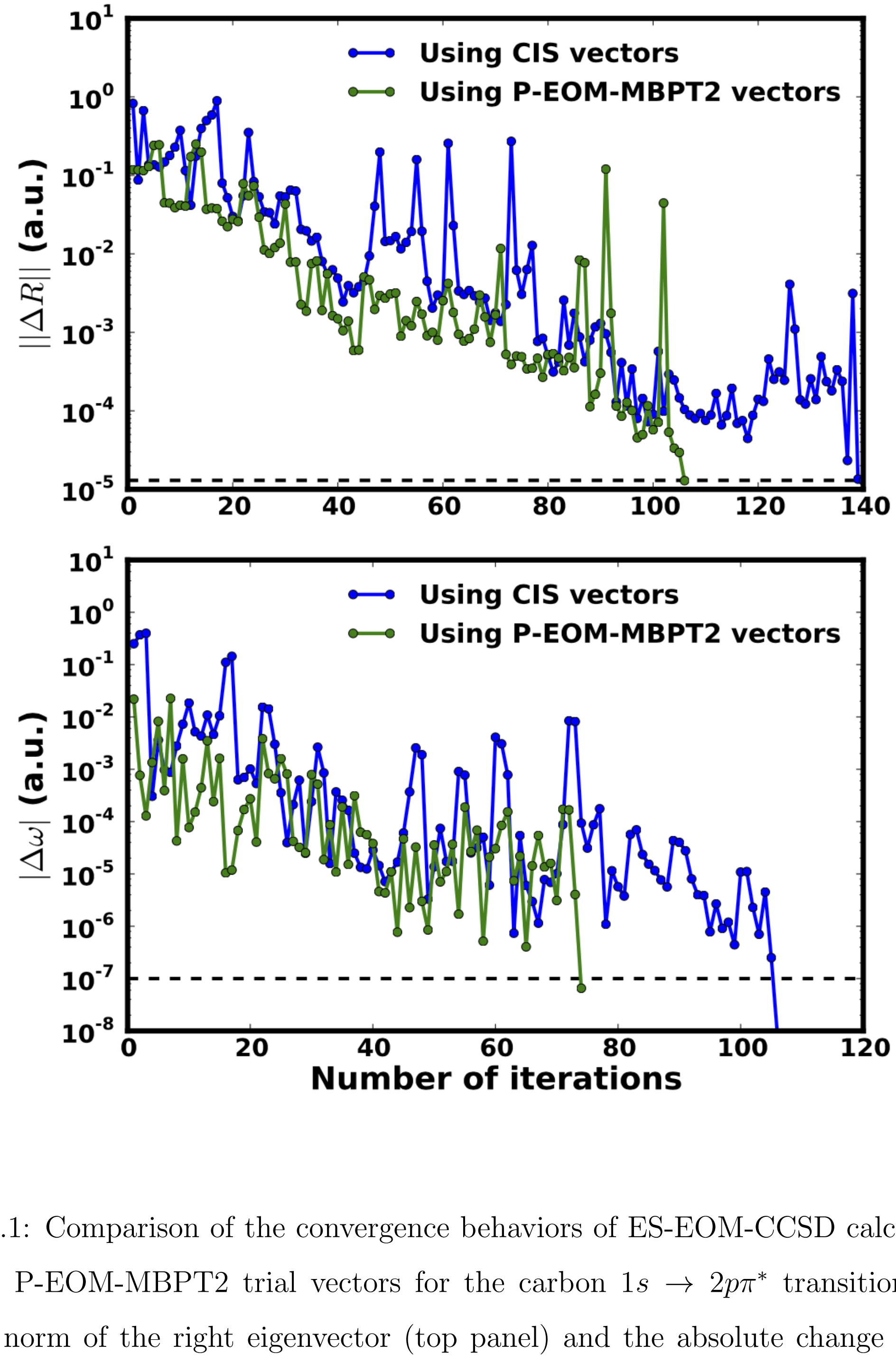

Figure 5.1: Comparison of the convergence behaviors of ES-EOM-CCSD calculations using CIS and P-EOM-MBPT2 trial vectors for the carbon $1s \rightarrow 2p\pi^*$ transition of CO. The residual norm of the right eigenvector (top panel) and the absolute change of eigenvalues (bottom panel) are plotted against the number of iterations. The basis set used is 6-311G$**$. The calculated excitation energy is 288.32 eV.

Table 5.2: Comparison of ES-EOM-CCSD with multi-reference EOM-MRCCSD[31, 189, 64] method and single-reference CPP-CCSD[111] method for select core-excitations of H_2O (in eV).

Excitation	Basis	ES-EOM-CCSD	EOM-MRCCSD	CPP-CCSD[111]	Experiment[185]
$1a_1 \rightarrow 4a_1$	6-311G**	535.72	535.76[31]	–	534.00
	cc-pVDZ	538.36	538.40[31, 189]	–	
	cc-pVTZ	535.41	535.34[189]	–	
	cc-pCVDZ	537.72	–	–	
	cc-pCVTZ	535.77	–	–	
	aug-cc-pVDZ	538.25	–	–	
	aug-cc-pVTZ	535.30	535.32[64]	–	
	aug-cc-pCVDZ	537.60	–	–	
	aug-cc-pCVTZ	535.66	–	535.68	
	d-aug-cc-pCVDZ	537.56	–	–	
$1a_1 \rightarrow 2b_1$	6-311G**	537.57	537.61[31]	–	535.90
	cc-pVDZ	540.17	540.21[31, 189]	–	
	cc-pVTZ	537.22	537.13[189]	–	
	cc-pCVDZ	539.53	–	–	
	cc-pCVTZ	537.59	–	–	
	aug-cc-pVDZ	540.05	–	–	
	aug-cc-pVTZ	537.08	537.11[64]	–	
	aug-cc-pCVDZ	539.40	–	–	
	aug-cc-pCVTZ	537.44	–	537.47	
	d-aug-cc-pCVDZ	539.36	–	–	

Table 5.3: Comparison of ES-EOM-CCSD with EA-EOM-CCSD[165] for select core-excitations. The EA-EOM-CCSD results are based on pre-defined core-hole reference states, and the latter is obtained from a so-called quasi-RHF (QRHF) calculation.[17, 180, 200] A modified Sadlej basis set is used in both calculations, where some atomic s and p functions are uncontracted from the original Sadlej basis set (see Ref. [165] for more details).

Molecule	Core	Excitation	ES-EOM-CCSD	EA-EOM-CCSD[165]	Experiment
CO	Carbon	$2\sigma \rightarrow 2\pi$	287.99	287.08	287.40[216]
	Oxygen	$1\sigma \rightarrow 2\pi$	535.52	534.15	534.21[104]
C_2H_2	Carbon	$1\sigma_u \rightarrow 1\pi_g(2p)$	286.70	286.21	285.81[144]
C_2H_4	Carbon	$1b_{1u} \rightarrow 1b_{2g}(2p)$	285.87	285.16	284.87 [144]
N_2	Nitrogen	$1\sigma_u \rightarrow 1\pi_g$	401.93	401.73	401.00[217]
CH_2O	Carbon	$2a_1 \rightarrow 2b_1(\pi^*)$	287.57	285.77	286.00[104]
	Oxygen	$1a_1 \rightarrow 2b_1(\pi^*)$	532.43	530.78	530.80[104]

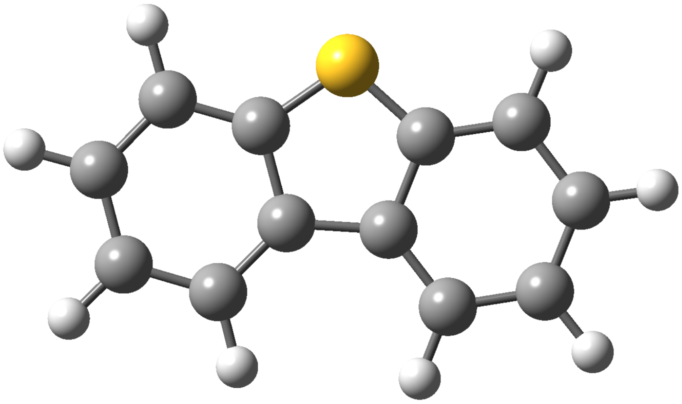

Figure 5.2: Structure of dibenzothiophene (DBT).

Table 5.4: Calculated K-edge transition energies for some small molecules. The basis set used here is d-aug-cc-pCVDZ.

Molecules	Excitation		Calculated excitation (eV)					Experimental
	energy (eV)		ES-TD-PBE1PBE	ES-TD-BHandHLYP	ES-P-EOM-MBPT2	ES-EOM-MBPT2	ES-EOM-CCSD	values (eV)
NH_3	N	1s → 3s	389.33	399.09	405.63	403.68	403.59	400.66 [185]
		1s → 3p (E)	390.57	400.45	407.07	405.35	405.26	402.33 [185]
		1s → 3p (A1)	390.84	401.17	407.53	406.02	405.90	402.86 [185]
		1s → 4s (A1)	390.96	401.68	408.22	406.70	406.60	403.57 [185]
Formaldehyde	C	1s → π^*	276.14	283.18	290.83	288.54	288.21	285.59 [178]
		1s → 3s	279.88	288.36	295.44	293.04	292.76	290.18 [178]
		1s → 3p (B2)	280.68	289.21	296.35	294.07	293.77	291.25 [178]
		1s → 3p (B1)	280.95	290.01	296.89	294.69	294.34	291.73 [178]
	O	1s → π^*	518.54	528.51	536.59	534.47	534.43	530.82 [178]
		1s → 3s	522.52	534.48	540.61	539.75	539.80	535.43 [178]
		1s → 3p	523.18	535.06	541.28	540.39	540.45	536.34 [178]
CO	C	1s → 2pπ^*	277.10	283.82	291.81	289.88	289.46	287.40 [61]
		1s → 3sσ	280.96	289.82	297.83	295.70	295.11	292.37 [61]
		1s → 3pπ	281.55	290.69	298.65	296.67	296.11	293.33 [61]
		1s → 3pσ	282.27	290.71	298.74	296.78	296.24	293.49 [61]
	O	1s → π^*	521.66	531.93	539.71	537.74	537.70	534.21 [174]
		1s → 3s	525.07	536.78	543.38	542.47	542.43	538.91 [174]
		1s → 3pπ	525.74	537.85	544.22	543.56	543.54	539.91 [174]
N_2	N	1s → 2pπ_g	390.02	398.37	406.78	404.30	403.78	401.00 [193]
		1s → 3sσ_g	393.68	404.05	411.47	409.67	409.09	406.10 [193]
		1s → 3pπ_u	394.35	405.01	412.25	410.59	410.02	407.00 [193]
N_2O	N_T	1s → 3pπ^*	390.47	399.11	407.65	405.27	404.37	401.10 [1]
		1s → 3sσ	392.97	403.40	410.66	408.57	407.55	403.90 [1]
	N_C	1s → 3pπ^*	393.79	402.17	410.94	408.63	407.83	404.70 [1]
		1s → 3pσ	396.20	406.45	414.52	412.40	411.48	407.60 [1]
Ethene	C	1s → π^*	275.41	282.81	289.89	287.43	287.36	284.67 [216]
		1s → 3s	277.34	285.93	292.20	289.95	289.77	287.24 [216]
		1s → 3pπ	277.88	286.48	292.78	290.59	290.41	287.88 [216]
H_2O	O	1s → $4a_1$/3s	520.99	531.96	538.98	537.52	537.56	534.00 [185]
		1s → $2b_1$/3p	522.45	533.43	540.61	539.34	539.36	535.90 [185]
		1s → 3p(b_2)	522.98	534.78	541.37	540.58	540.59	537.00 [185]

Table 5.5: Error analyses of 31 calculated K-edge excitation energies (eV). For error analyses of shifted energies, excitation energies are uniformly shifted so that the lowest-energy transition matches the corresponding experimental value. MAE: Mean absolute error. StDev: standard deviation. MSE: mean signed error. RMS: root mean square. Max AE: maximum absolute error. ES-TDDFT results were obtained using the method in Ref. [135] and the basis set used is d-aug-cc-pCVDZ.

	Absolute K-edge Excitations				Shifted K-edge Excitations			
	MAE (StDev)	MSE (StDev)	RMS	Max AE	MAE (StDev)	MSE (StDev)	RMS	Max AE
ES-PBE1PBE	11.68 (1.35)	-11.68 (1.35)	11.75	14.17	0.95 (0.42)	-0.95 (0.42)	1.04	1.67
ES-BHandHLYP	1.99 (0.61)	-1.99 (0.61)	2.08	3.58	0.62 (0.38)	0.45 (0.58)	0.72	1.49
ES-P-EOM-MBPT2	5.24 (0.66)	5.24 (0.66)	5.28	6.92	0.49 (0.34)	-0.18 (0.58)	0.59	1.19
ES-EOM-MBPT2	3.42 (0.57)	3.42 (0.57)	3.46	4.80	0.29 (0.29)	0.23 (0.34)	0.41	0.86
ES-EOM-CCSD	3.11 (0.53)	3.11 (0.53)	3.15	4.37	0.27 (0.26)	0.20 (0.32)	0.37	0.76

Table 5.6: Calculated sulfur $1s \rightarrow 3p$ K-edge excitation energies for dibenzothiophene (DBT) (in eV). The basis set used here is 6-311++G*.

	Absolute K-edge Excitations			Shifted K-edge Excitations	
	$1s \rightarrow 3p\pi^*$ (B2)	$1s \rightarrow 3p\sigma$ (B1)	$1s \rightarrow 3p\pi^*$ (A1)	$1s \rightarrow 3p\sigma$ (B1)	$1s \rightarrow 3p\pi^*$ (A1)
ES-PBE1PBE	2420.55	2420.63	2422.26	2472.08	2473.71
ES-BHandHLYP	2446.19	2447.73	2448.69	2473.54	2474.50
ES-P-EOM-MBPT2	2471.29	2472.96	2473.35	2473.67	2474.06
ES-EOM-MBPT2	2470.38	2472.54	2472.68	2474.16	2474.30
ES-EOM-CCSD	2470.32	2472.42	2472.56	2474.10	2474.24

BIBLIOGRAPHY

[1] J. Adachi, N. Kosugi, E. Shigemasa, and A. Yagishita. Renner–Teller Effect and Rydberg-valence Mixing in the N and O K-edge Photoabsorption Spectra of N_2O. *J. Chem. Phys.*, 102(19):7369–7376, 1995. doi: 10.1063/1.469049. URL `http://scitation.aip.org/content/aip/journal/jcp/102/19/10.1063/1.469049`.

[2] C. Adamo and V. Barone. Toward Reliable Density Functional Methods Without Adjustable Parameters: The PBE0 Model. *J. Chem. Phys.*, 110(13):6158–6170, 1999. doi: 10.1063/1.478522. URL `http://scitation.aip.org/content/aip/journal/jcp/110/13/10.1063/1.478522`.

[3] J. W. Allen. Impact Excitation and Auger Quenching of Luminescent Centres in Crystals, with Special Reference to ZnS:Mn. *J. Phys. C: Solid State Phys.*, 19(31):6287–6295, 1986. doi: 10.1088/0022-3719/19/31/021. URL `http://stacks.iop.org/0022-3719/19/i=31/a=021`.

[4] K. Andersson and B. O. Roos. *Multi-Configurational Second-Order Perturbation Theory*, volume 1 of *Advanced Series in Physical Chemistry.* World Scientific, 1995. ISBN 9789810229887.

[5] F. A. Asmuruf and N. A. Besley. Time Dependent Density Functional Theory Study of the Near Edge X-ray Absorption Fine Structure of Benzene in Gas Phase and on Metal Surfaces. *J. Chem. Phys.*, 129(6):064705, 2008. doi: 10.1063/1.2967190. URL `http://scitation.aip.org/content/aip/journal/jcp/129/6/10.1063/1.2967190`.

[6] F. A. Asmuruf and N. A. Besley. Calculation of Near Edge X-ray Absorption Fine Structure With the CIS(D) Method. *Chem. Phys. Lett.*, 463(1–3):267–271, 2008.

doi: 10.1016/j.cplett.2008.08.054. URL `http://www.sciencedirect.com/science/article/pii/S0009261408011469`.

[7] J. Autschbach, F. E. Jorge, and T. Ziegler. Density Functional Calculations on Electronic Circular Dichroism Spectra of Chiral Transition Metal Complexes. *Inorg. Chem.*, 42(9):2867–2877, 2003. doi: 10.1021/ic020580w. URL `http://dx.doi.org/10.1021/ic020580w`.

[8] U. Aygül, D. Batchelor, U. Dettinger, S. Yilmaz, S. Allard, U. Scherf, H. Peisert, and T. Chassé. Molecular Orientation in Polymer Films for Organic Solar Cells Studied by NEXAFS. *J. Phys. Chem. C*, 116(7):4870–4874, 2012. doi: 10.1021/jp205653n. URL `http://dx.doi.org/10.1021/jp205653n`.

[9] S. G. Ayling and J. W. Allen. Auger Quenching of Luminescence in ZnSe:Mn. *J. Phys. C: Solid State Phys.*, 20(26):4251–4257, 1987. doi: 10.1088/0022-3719/20/26/025. URL `http://stacks.iop.org/0022-3719/20/i=26/a=025`.

[10] G. B. Bacskay. A Quadratically Convergent Hartree-Fock (QC-SCF) Method. Application to Closed Shell Systems. *Chem. Phys.*, 61:385–404, 1981. doi: 10.1016/0301-0104(81)85156-7. URL `http://www.sciencedirect.com/science/article/pii/0301010481851567`.

[11] E. Badaeva, Y. Feng, D. R. Gamelin, and X. Li. Investigation of Pure and Co^{2+}-doped ZnO Quantum Dot Electronic Structures Using the Density Functional Theory: Choosing the Right Functional. *New J. Phys.*, 10(5):055013, 2008. doi: 10.1088/1367-2630/10/5/055013. URL `http://stacks.iop.org/1367-2630/10/i=5/a=055013`.

[12] E. Badaeva, C. M. Isborn, Y. Feng, S. T. Ochsenbein, D. R. Gamelin, and X. Li. Theoretical Characterization of Electronic Transitions in Co^{2+}- and Mn^{2+}-Doped ZnO Nanocrystals. *J. Phys. Chem. C*, 113(20):8710–8717, 2009. doi: 10.1021/jp900392j. URL `http://dx.doi.org/10.1021/jp900392j`.

[13] E. Badaeva, J. W. May, J. Ma, D. R. Gamelin, and X. Li. Characterization of Excited-State Magnetic Exchange in Mn^{2+}-Doped ZnO Quantum Dots Using Time-Dependent Density Functional Theory. *J. Phys. Chem. C*, 115(43):20986–20991, 2011. doi: 10.1021/jp206622e. URL `http://dx.doi.org/10.1021/jp206622e`.

[14] P. S. Bagus. Self-Consistent-Field Wave Functions for Hole States of Some Ne-Like and Ar-Like Ions. *Phys. Rev.*, 139:A619–A634, 1965. doi: 10.1103/PhysRev.139.A619. URL `http://link.aps.org/doi/10.1103/PhysRev.139.A619`.

[15] Christopher J. Bardeen. The Structure and Dynamics of Molecular Excitons. *Annu. Rev. Phys. Chem.*, 65(1):127–148, 2014. doi: 10.1146/annurev-physchem-040513-103654. URL `http://dx.doi.org/10.1146/annurev-physchem-040513-103654`.

[16] R. J. Bartlett. Many-Body Perturbation Theory and Coupled Cluster Theory for Electron Correlation in Molecules. *Annu. Rev. Phys. Chem.*, 32(1):359–401, 1981. doi: 10.1146/annurev.pc.32.100181.002043. URL `http://dx.doi.org/10.1146/annurev.pc.32.100181.002043`.

[17] R. J. Bartlett and J. F. Stanton. Applications of Post-Hartree-Fock Methods: A Tutorial. *Rev. Comp. Chem.*, 5:65–169, 1994. doi: 10.1002/9780470125823.ch2. URL `http://dx.doi.org/10.1002/9780470125823.ch2`.

[18] S. S. Bayin. *Mathematical Methods in Science and Engineering*. Wiley-Interscience, Hoboken, NJ, 2006.

[19] R. Beaulac and D. R. Gamelin. Two-Center Formulation of Mn^{2+}-electron *s*-*d* Exchange Coupling in Bulk and Quantum-Confined Diluted Magnetic Semiconductors. *Phys. Rev. B*, 82:224401, 2010. doi: 10.1103/PhysRevB.82.224401. URL `http://link.aps.org/doi/10.1103/PhysRevB.82.224401`.

[20] R. Beaulac, S. T. Ochsenbein, and D. R. Gamelin. *Semiconductor Quantum Dots.* CRC press, Taylor & Francis Group, Boca Raton, FL, 2nd edition, 2010. ISBN 9781420079272.

[21] R. Beaulac, Y. Feng, J. W. May, E. Badaeva, D. R. Gamelin, and X. Li. Orbital pathways for Mn^{2+}-carrier $sp-d$ exchange in diluted magnetic semiconductor quantum dots. *Phys. Rev. B*, 84:195324, 2011. doi: 10.1103/PhysRevB.84.195324. URL `http://link.aps.org/doi/10.1103/PhysRevB.84.195324`.

[22] A. D. Becke. Density-Functional Exchange-Energy Approximation With Correct Asymptotic Behavior. *Phys. Rev. A*, 38:3098–3100, 1988. doi: 10.1103/PhysRevA.38.3098. URL `http://link.aps.org/doi/10.1103/PhysRevA.38.3098`.

[23] A. D. Becke. A New Mixing of Hartree–Fock and Local Density-Functional Theories. *J. Chem. Phys.*, 98(2):1372–1377, 1993. doi: 10.1063/1.464304. URL `http://scitation.aip.org/content/aip/journal/jcp/98/2/10.1063/1.464304`.

[24] N. H. F. Beebe and J. Linderberg. Simplifications in the Generation and Transformation of Two-Electron Integrals in Molecular Calculations. *Int. J. Quant. Chem.*, 12 (4):683–705, 1977. doi: 10.1002/qua.560120408. URL `http://dx.doi.org/10.1002/qua.560120408`.

[25] J. Behler, B. Delley, K. Reuter, and M. Scheffler. Nonadiabatic Potential-Energy Surfaces By Constrained Density-Functional Theory. *Phys. Rev. B*, 75:115409–115418, 2007. doi: 10.1103/PhysRevB.75.115409. URL `http://link.aps.org/doi/10.1103/PhysRevB.75.115409`.

[26] S. Bernadotte, F. Evers, and C. R. Jacob. Plasmons in Molecules. *J. Phys. Chem. C*, 117(4):1863–1878, 2013. doi: 10.1021/jp3113073. URL `http://dx.doi.org/10.1021/jp3113073`.

[27] N. A. Besley and F. A. Asmuruf. Time-Dependent Density Functional Theory Calculations of the Spectroscopy of Core Electrons. *Phys. Chem. Chem. Phys.*, 12:12024–12039, 2010. doi: 10.1039/C002207A. URL `http://dx.doi.org/10.1039/C002207A`.

[28] N. A. Besley, A. T. B. Gilbert, and P. M. W. Gill. Self-Consistent Field Calculations of Core Excited States. *J. Chem. Phys.*, 130(12):124308–124314, 2009. doi: 10.1063/1.3092928. URL `http://scitation.aip.org/content/aip/journal/jcp/130/12/10.1063/1.3092928`.

[29] N. A. Besley, M. J. G. Peach, and D. J. Tozer. Time-dependent Density Functional Theory Calculations of Near Edge X-ray Absorption Fine Structure With Short-range Corrected Functionals. *Phys. Chem. Chem. Phys.*, 11:10350–10358, 2009. doi: 10.1039/B912718F. URL `http://dx.doi.org/10.1039/B912718F`.

[30] F. Bosi, U. Halenius, G. B. Andreozzi, H. Skogby, and S. Lucchesi. Structural Refinement and Crystal Chemistry of Mn-Doped Spinel: A Case for Tetrahedrally Coordinated Mn^{3+} in An Oxygen-Based Structure. *Am. Mineral.*, 92(1):27–33, 2007. doi: 10.2138/am.2007.2266. URL `http://ammin.geoscienceworld.org/content/92/1/27.abstract`.

[31] J. Brabec, K. Bhaskaran-Nair, N. Govind, J. Pittner, and K. Kowalski. Communication: Application of State-Specific Multireference Coupled Cluster Methods to Core-Level Excitations. *J. Chem. Phys.*, 137(17):171101, 2012. doi: 10.1063/1.4764355. URL `http://scitation.aip.org/content/aip/journal/jcp/137/17/10.1063/1.4764355`.

[32] E. Broclawik and T. Borowski. Time-Dependent DFT Study on Electronic States of Vanadium and Molybdenum Oxide Molecules. *Chem. Phys. Lett.*, 339(5–6):433–437, 2001. doi: 10.1016/S0009-2614(01)00361-X. URL `http://www.sciencedirect.com/science/article/pii/S000926140100361X`.

[33] L. E. Brus. A simple model for the ionization potential, electron affinity, and aqueous redox potentials of small semiconductor crystallites. *J. Chem. Phys.*, 79(11):5566–5571, 1983. doi: 10.1063/1.445676. URL `http://scitation.aip.org/content/aip/journal/jcp/79/11/10.1063/1.445676`.

[34] L. E. Brus. Electronic Wave Functions in Semiconductor Clusters: Experiment and Theory. *J. Phys. Chem.*, 90(12):2555–2560, 1986. doi: 10.1021/j100403a003. URL `http://dx.doi.org/10.1021/j100403a003`.

[35] R. J. Buenker, S. D. Peyerimhoff, and W. Butscher. Applicability of the Multi-Reference Double-Excitation CI (MRD-CI) Method to the Calculation of Electronic Wave Functions and Comparison with Related Techniques. *Mol. Phys.*, 35(3):771–791, 1978. doi: 10.1080/00268977800100581. URL `http://dx.doi.org/10.1080/00268977800100581`.

[36] Von J. G. Calvert and J. N. Pitts. *Photochemistry.* Wiley, New York, 1966.

[37] M. Caricato, G. W. Trucks, and M. J. Frisch. A Comparison of Three Variants of the Generalized Davidson Algorithm for the Partial Diagonalization of Large Non-Hermitian Matrices. *J. Chem. Theor. Comput.*, 6(7):1966–1970, 2010. doi: 10.1021/ct100111w. URL `http://dx.doi.org/10.1021/ct100111w`.

[38] J. Carreras, C. Bonafos, J. Montserrat, C. Domínguez, J. Arbiol, and B. Garrido. Auger Quenching-Based Modulation of Electroluminescence from Ion-Implanted Silicon Nanocrystals. *Nanotechnology*, 19(20):205201, 2008. doi: 10.1088/0957-4484/19/20/205201. URL `http://stacks.iop.org/0957-4484/19/i=20/a=205201`.

[39] P. Cársky, J. Paldus, and J. Pittner, editors. *Coupled-cluster Theory.* Springer Netherlands, 2010. ISBN 9789048128853. doi: 10.1007/978-90-481-2885-3.

[40] M. E. Casida. *Time-Dependent Density-Functional Response Theory for Molecules.* World Scientific, 1995. ISBN 9789814499729.

[41] M. E. Casida. *Time-Dependent Density Functional Response Theory of Molecular Systems: Theory, Computational Methods, and Functionals*, volume 4 of *Theoretical and Computational Chemistry*. Elsevier, 1996. doi: 10.1016/S1380-7323(96)80093-8. URL `http://www.sciencedirect.com/science/article/pii/S1380732396800938`.

[42] M. E. Casida. TIme-Dependent Density Functional Theory for Molecules and Molecular Solids. *J. Mol. Struct.: THEOCHEM*, 914(1–3):3–18, 2009. doi: 10.1016/j.theochem.2009.08.018. URL `http://www.sciencedirect.com/science/article/pii/S0166128009005363`.

[43] P. Cassam-Chenai, S. K. Wolff, G. S. Chandler, and B. N. Figgis. Ensemble-Representable Densities for Atoms and Molecules. II. Application to $\mathrm{CoCl_4}^{2-}$. *Int. J. Quant. Chem.*, 60(2):667–680, 1996. doi: 10.1002/(SICI)1097-461X(1996)60:2⟨667::AID-QUA5⟩3.0.CO;2-V. URL `http://dx.doi.org/10.1002/(SICI)1097-461X(1996)60:2<667::AID-QUA5>3.0.CO;2-V`.

[44] L. S. Cederbaum, W. Domcke, and J. Schirmer. Many-body Theory of Core Holes. *Phys. Rev. A*, 22:206–222, 1980. doi: 10.1103/PhysRevA.22.206. URL `http://link.aps.org/doi/10.1103/PhysRevA.22.206`.

[45] L. X. Chen, W. J. Jäger, G. Jennings, D. J. Gosztola, A. Munkholm, and J. P. Hessler. Capturing a Photoexcited Molecular Structure Through Time-Domain X-ray Absorption Fine Structure. *Science*, 292(5515):262–264, 2001. doi: 10.1126/science.1057063. URL `http://science.sciencemag.org/content/292/5515/262`.

[46] D. I. Chepic, A. L. Efros, A. I. Ekimov, M. G. Ivanov, V. A. Kharchenko, I. A. Kudriavtsev, and T. V. Yazeva. Auger Ionization of Semiconductor Quantum Drops in A Glass Matrix. *J. Lumin.*, 47(3):113–127, 1990. doi: 10.1016/0022-2313(90)90007-X. URL `http://www.sciencedirect.com/science/article/pii/002223139090007X`.

[47] A. V. Chernenko, A. S. Brichkin, N. A. Sobolev, and M. C. Carmo. Mechanisms of

Manganese-Assisted Non-Radiative Recombination in Cd(Mn)Se/Zn(Mn)Se Quantum Dots. *J. Phys.–Condens. Mat.*, 22(35):355306, 2010. doi: 10.1088/0953-8984/22/35/355306. URL `http://stacks.iop.org/0953-8984/22/i=35/a=355306`.

[48] O. Christiansen, H. Koch, and P. Jörgensen. The Second-Order Approximate Coupled Cluster Singles and Doubles Model CC2. *Chem. Phys. Lett.*, 243(5-6):409–418, 1995. doi: 10.1016/0009-2614(95)00841-Q. URL `http://www.sciencedirect.com/science/article/pii/000926149500841Q`.

[49] C. Chuang, J. Knoester, and J. Cao. Scaling Relations and Optimization of Excitonic Energy Transfer Rates Between One-Dimensional Molecular Aggregates. *J. Phys. Chem. B*, 118(28):7827–7834, 2014. doi: 10.1021/jp4124502. URL `http://dx.doi.org/10.1021/jp4124502`.

[50] S. Coffa, G. Franzò, and F. Priolo. High Efficiency and Fast Modulation of Er-doped Light Emitting Si Diodes. *Appl. Phys. Lett.*, 69(14):2077–2079, 1996. doi: 10.1063/1.116885. URL `http://scitation.aip.org/content/aip/journal/apl/69/14/10.1063/1.116885`.

[51] D. C. Comeau and R. J. Bartlett. The Equation-of-Motion Coupled-Cluster Method. Applications to Open-and Closed-Shell Reference States. *Chem. Phys. Lett.*, 207(4):414–423, 1993. doi: 10.1016/0009-2614(93)89023-B. URL `http://www.sciencedirect.com/science/article/pii/000926149389023B`.

[52] S. Coriani, T. Fransson, O. Christiansen, and P. Norman. Asymmetric-Lanczos-Chain-Driven Implementation of Electronic Resonance Convergent Coupled-Cluster Linear Response Theory. *J. Chem. Theor. Comput.*, 8(5):1616–1628, 2012. doi: 10.1021/ct200919e. URL `http://dx.doi.org/10.1021/ct200919e`.

[53] G. E. Cragg and A. L. Efros. Suppression of Auger Processes in Confined Structures.

Nano Lett., 10(1):313–317, 2010. doi: 10.1021/nl903592h. URL `http://dx.doi.org/10.1021/nl903592h`.

[54] T. D. Crawford and H. F. Schaefer. *An Introduction to Coupled Cluster Theory for Computational Chemists*. John Wiley & Sons, 2007. ISBN 9780470125915. doi: 10.1002/9780470125915.ch2. URL `http://dx.doi.org/10.1002/9780470125915.ch2`.

[55] B. Dai, K. M. Deng, J. L. Yang, and Q. S. Zhu. Excited States of the 3*d* Transition Metal Monoxides. *J. Chem. Phys.*, 118(21):9608–9613, 2003. doi: 10.1063/1.1570811. URL `http://scitation.aip.org/content/aip/journal/jcp/118/21/10.1063/1.1570811`.

[56] E. R. Davidson. The Iterative Calculation of a Few of the Lowest Eigenvalues and Corresponding Eigenvectors of Large Real-Symmetric Matrices. *J. Comput. Phys.*, 17(1):87–94, 1975. doi: 10.1016/0021-9991(75)90065-0. URL `http://www.sciencedirect.com/science/article/pii/0021999175900650`.

[57] F. J. G. De Abajo. Nonlocal Effects in the Plasmons of Strongly Interacting Nanoparticles, Dimers, and Waveguides. *J. Phys. Chem. C*, 112(46):17983–17987, 2008. doi: 10.1021/jp807345h. URL `http://dx.doi.org/10.1021/jp807345h`.

[58] S. DeBeer George, T. Petrenko, and F. Neese. Time-dependent Density Functional Calculations of Ligand K-edge X-ray Absorption Spectra. *Inorg. Chim. Acta*, 361(4):965–972, 2008. doi: 10.1016/j.ica.2007.05.046. URL `http://www.sciencedirect.com/science/article/pii/S0020169307003374`.

[59] W. D. Derricotte and F. A. Evangelista. Simulation of X-ray Absorption Spectra With Orthogonality Constrained Density Functional Theory. *Phys. Chem. Chem. Phys.*, 17:14360–14374, 2015. doi: 10.1039/C4CP05509H. URL `http://dx.doi.org/10.1039/C4CP05509H`.

[60] F. Ding, E. B. Guidez, C. M. Aikens, and X. Li. Quantum Coherent Plasmon in Silver Nanowires: A Real-Time TDDFT Study. *J. Chem. Phys.*, 140(24):244705, 2014. doi: 10.1063/1.4884388. URL `http://scitation.aip.org/content/aip/journal/jcp/140/24/10.1063/1.4884388`.

[61] M. Domke, C. Xue, A. Puschmann, T. Mandel, E. Hudson, D. A. Shirley, and G. Kaindl. Carbon and Oxygen K-edge Photoionization of the CO Molecule. *Chem. Phys. Lett.*, 173(1):122–128, 1990. doi: 10.1016/0009-2614(90)85314-3. URL `http://www.sciencedirect.com/science/article/pii/0009261490853143`.

[62] A. Dreuw and M. Head-Gordon. Single-Reference Ab Initio Methods for the Calculation of Excited States of Large Molecules. *Chem. Rev.*, 105(11):4009–4037, 2005. doi: 10.1021/cr0505627. URL `http://dx.doi.org/10.1021/cr0505627`.

[63] J. L. DuBois, P. Mukherjee, T. D. P. Stack, B. Hedman, E. I. Solomon, and K. O. Hodgson. A Systematic K-edge X-ray Absorption Spectroscopic Study of Cu(III) Sites. *J. Am. Chem. Soc.*, 122(24):5775–5787, 2000. doi: 10.1021/ja993134p. URL `http://dx.doi.org/10.1021/ja993134p`.

[64] A. K. Dutta, J. Gupta, N. Vaval, and S. Pal. Intermediate Hamiltonian Fock Space Multireference Coupled Cluster Approach to Core Excitation Spectra. *J. Chem. Theor. Comput.*, 10(9):3656–3668, 2014. doi: 10.1021/ct500285e. URL `http://dx.doi.org/10.1021/ct500285e`.

[65] A. L. Efros and M. Rosen. Random Telegraph Signal in the Photoluminescence Intensity of a Single Quantum Dot. *Phys. Rev. Lett.*, 78:1110–1113, 1997. doi: 10.1103/PhysRevLett.78.1110. URL `http://link.aps.org/doi/10.1103/PhysRevLett.78.1110`.

[66] A. L. Efros, E. I. Rashba, and M. Rosen. Paramagnetic Ion-Doped Nanocrystal as a Voltage-Controlled Spin Filter. *Phys. Rev. Lett.*, 87:206601, 2001. doi: 10.1103/

PhysRevLett.87.206601. URL `http://link.aps.org/doi/10.1103/PhysRevLett.87.206601`.

[67] I. Egri. Excitons and Plasmons in Metals, Semiconductors and Insulators: A Unified Approach. *Phys. Rep.*, 119(6):363–402, 1985. doi: 10.1016/0370-1573(85)90085-7. URL `http://www.sciencedirect.com/science/article/pii/0370157385900857`.

[68] M. Ehara, T. Horikawa, R. Fukuda, H. Nakatsuji, T. Tanaka, H. Kato, M. Hoshino, H. Tanaka, R. Feifel, and K. Ueda. Symmetry and Vibrationally Resolved Absorption Spectra Near the N K-edges of N_2O: Experiment and Theory. *Phys. Rev. A*, 83:062506, 2011. doi: 10.1103/PhysRevA.83.062506. URL `http://link.aps.org/doi/10.1103/PhysRevA.83.062506`.

[69] F. A. Evangelista, P. Shushkov, and J C. Tully. Orthogonality Constrained Density Functional Theory for Electronic Excited States. *J. Phys. Chem. A*, 117(32):7378–7392, 2013. doi: 10.1021/jp401323d. URL `http://dx.doi.org/10.1021/jp401323d`.

[70] D. Feller. The Role of Databases in Support of Computational Chemistry Calculations. *J. Comput. Chem.*, 17(13):1571–1586, 1996. doi: 10.1002/(SICI)1096-987X(199610)17:13⟨1571::AID-JCC9⟩3.0.CO;2-P. URL `http://dx.doi.org/10.1002/(SICI)1096-987X(199610)17:13<1571::AID-JCC9>3.0.CO;2-P`.

[71] J. B. Foresman, M. Head-Gordon, J. A. Pople, and M. J. Frisch. Toward A Systematic Molecular Orbital Theory for Excited States. *J. Phys. Chem.*, 96(1):135–149, 1992. doi: 10.1021/j100180a030. URL `http://dx.doi.org/10.1021/j100180a030`.

[72] T. Förster. Zwischenmolekulare energiewanderung und fluoreszenz. *Annalen der Physik*, 437(1–2):55–75, 1948. doi: 10.1002/andp.19484370105. URL `http://dx.doi.org/10.1002/andp.19484370105`.

[73] T. Fransson, S. Coriani, O. Christiansen, and P. Norman. Carbon X-ray Absorption Spectra of Fluoroethenes and Acetone: A Study at the Coupled Cluster, Density Func-

tional, and Static-exchange Levels of Theory. *J. Chem. Phys.*, 138(12):124311, 2013. doi: 10.1063/1.4795835. URL `http://scitation.aip.org/content/aip/journal/jcp/138/12/10.1063/1.4795835`.

[74] M. J. Frisch, G. W. Trucks, H. B. Schlegel, G. E. Scuseria, M. A. Robb, J. R. Cheeseman, G. Scalmani, V. Barone, B. Mennucci, G. A. Petersson, H. Nakatsuji, M. Caricato, X. Li, H. P. Hratchian, A. F. Izmaylov, J. Bloino, G. Zheng, J. L. Sonnenberg, W. Liang, M. Hada, M. Ehara, K. Toyota, R. Fukuda, J. Hasegawa, M. Ishida, T. Nakajima, Y. Honda, O. Kitao, H. Nakai, T. Vreven, Jr. J. A. Montgomery, J. E. Peralta, F. Ogliaro, M. Bearpark, J. J. Heyd, E. Brothers, K. N. Kudin, V. N. Staroverov, T. Keith, R. Kobayashi, J. Normand, K. Raghavachari, A. Rendell, J. C. Burant, S. S. Iyengar, J. Tomasi, M. Cossi, N. Rega, J. M. Millam, M. Klene, J. E. Knox, J. B. Cross, V. Bakken, C. Adamo, J. Jaramillo, R. Gomperts, R. E. Stratmann, O. Yazyev, A. J. Austin, R. Cammi, C. Pomelli, J. W. Ochterski, R. L. Martin, K. Morokuma, V. G. Zakrzewski, G. A. Voth, P. Salvador, J. J. Dannenberg, S. Dapprich, P. V. Parandekar, N. J. Mayhall, A. D. Daniels, Ö. Farkas, J. B. Foresman, J. V. Ortiz, J. Cioslowski, and D. J. Fox. Gaussian Development Version, 2016. Gaussian Inc., Wallingford CT.

[75] G. Fronzoni, R. De Francesco, and M. Stener. Time Dependent Density Functional Theory of X-ray Absorption Spectroscopy of Alkaline-Earth Oxides. *J. Phys. Chem. B*, 109(20):10332–10340, 2005. doi: 10.1021/jp050755y. URL `http://dx.doi.org/10.1021/jp050755y`.

[76] J. K. Furdyna. Diluted Magnetic Semiconductors. *J. Appl. Phys.*, 64(4):R29–R64, 1988. doi: 10.1063/1.341700. URL `http://scitation.aip.org/content/aip/journal/jap/64/4/10.1063/1.341700`.

[77] J. Gauss. *Coupled-cluster Theory.* John Wiley & Sons, 2002. ISBN 9780470845011. doi: 10.1002/0470845015.cca058. URL `http://dx.doi.org/10.1002/0470845015.cca058`.

[78] A. T. B. Gilbert, N. A. Besley, and P. M. W. Gill. Self-Consistent Field Calculations of Excited States Using the Maximum Overlap Method (MOM). *J. Phys. Chem. A*, 112(50):13164–13171, 2008. doi: 10.1021/jp801738f. URL `http://dx.doi.org/10.1021/jp801738f`.

[79] J. J. Goings, M. Caricato, M. J. Frisch, and X. Li. Assessment of Low-scaling Approximations to the Equation of Motion Coupled-Cluster Singles and Doubles Equations. *J. Chem. Phys.*, 141(16):164116, 2014. doi: 10.1063/1.4898709. URL `http://scitation.aip.org/content/aip/journal/jcp/141/16/10.1063/1.4898709`.

[80] D. S. Golubev and A. D. Zaikin. Intrinsic Decoherence in Mesoscopic Systems. *Phys. Rev. Lett.*, 78:3366–3369, 1997. doi: 10.1103/PhysRevLett.78.3366. URL `http://link.aps.org/doi/10.1103/PhysRevLett.78.3366`.

[81] D. S. Golubev and A. D. Zaikin. Quantum Decoherence in Disordered Mesoscopic Systems. *Phys. Rev. Lett.*, 81:1074–1077, 1998. doi: 10.1103/PhysRevLett.81.1074. URL `http://link.aps.org/doi/10.1103/PhysRevLett.81.1074`.

[82] D. S. Golubev and A. D. Zaikin. Quantum Decoherence and Weak Localization at Low Temperatures. *Phys. Rev. B*, 59:9195–9213, 1999. doi: 10.1103/PhysRevB.59.9195. URL `http://link.aps.org/doi/10.1103/PhysRevB.59.9195`.

[83] D. S. Golubev, A. D. Zaikin, and G. Schön. On Low-Temperature Dephasing by Electron-Electron Interaction. *J. Low Temp. Phys*, 126(3):1355–1376, 2002. doi: 10.1023/A:1013800304448. URL `http://dx.doi.org/10.1023/A:1013800304448`.

[84] N. T. Gordon and J. W. Allen. Auger Quenching of Luminescence in ZnS:Mn. *Solid State Commun.*, 37(5):441–443, 1981. doi: 10.1016/0038-1098(81)91224-2. URL `http://www.sciencedirect.com/science/article/pii/0038109881912242`.

[85] A. Görling. Density-Functional Theory Beyond the Hohenberg-Kohn Theorem. *Phys.*

Rev. A, 59:3359–3374, 1999. doi: 10.1103/PhysRevA.59.3359. URL `http://link.aps.org/doi/10.1103/PhysRevA.59.3359`.

[86] N. Greenwood and A. Earnshaw. *Chemistry of the Elements*. Pegamon Press, New York, 1984. ISBN 0750633654.

[87] E. K. U. Gross, J. F. Dobson, and M. Petersilka. *Density Functional Theory II: Relativistic and Time Dependent Extensions*. Springer, Heidelberg, Berlin, 1996. ISBN 978-3-540-49946-6. doi: 10.1007/BFb0016643. URL `http://dx.doi.org/10.1007/BFb0016643`.

[88] M. Grüning, A. Marini, and X. Gonze. Exciton-Plasmon States in Nanoscale Materials: Breakdown of the Tamm–Dancoff Approximation. *Nano Lett.*, 9(8):2820–2824, 2009. doi: 10.1021/nl803717g. URL `http://dx.doi.org/10.1021/nl803717g`.

[89] E. B. Guidez and C. M. Aikens. Theoretical Analysis of the Optical Excitation Spectra of Silver and Gold Nanowires. *Nanoscale*, 4:4190–4198, 2012. doi: 10.1039/C2NR30253E. URL `http://dx.doi.org/10.1039/C2NR30253E`.

[90] H. E. Gumlich. Electro- and Photoluminescence Properties of Mn^{2+} in ZnS and ZnCdS. *J. Lumin.*, 23(1):73–99, 1981. doi: 10.1016/0022-2313(81)90191-5. URL `http://www.sciencedirect.com/science/article/pii/0022231381901915`.

[91] O. Gunnarsson and B. I. Lundqvist. Exchange and Correlation in Atoms, Molecules, and Solids by the Spin-Density-Functional Formalism. *Phys. Rev. B*, 13:4274–4298, 1976. doi: 10.1103/PhysRevB.13.4274. URL `http://link.aps.org/doi/10.1103/PhysRevB.13.4274`.

[92] S. R. Gwaltney and R. J. Bartlett. Gradients for the Partitioned Equation-of-Motion Coupled-Cluster Method. *J. Chem. Phys.*, 110(1):62–71, 1999. doi: 10.1063/1.478085. URL `http://scitation.aip.org/content/aip/journal/jcp/110/1/10.1063/1.478085`.

[93] S. R. Gwaltney, M. Nooijen, and R. J. Bartlett. Simplified Methods for Equation-of-Motion Coupled-Cluster Excited State Calculations. *Chem. Phys. Lett.*, 248(3–4):189–198, 1996. doi: 10.1016/0009-2614(95)01329-6. URL `http://www.sciencedirect.com/science/article/pii/0009261495013296`.

[94] W. A. Harrison. *Electronic Structure and the Properties of Solids*. Dover Publications, Mineola, NY, 1989.

[95] P. J. Hay and W. R. Wadt. Ab initio Effective Core Potentials for Molecular Calculations. Potentials for the Transition Metal Atoms Sc to Hg. *J. Chem. Phys.*, 82(1):270–283, 1985. doi: 10.1063/1.448799. URL `http://scitation.aip.org/content/aip/journal/jcp/82/1/10.1063/1.448799`.

[96] P. J. Hay and W. R. Wadt. Ab initio Effective Core Potentials for Molecular Calculations. Potentials for K to Au Including the Outermost Core Orbitals. *J. Chem. Phys.*, 82(1):299–310, 1985. doi: 10.1063/1.448975. URL `http://scitation.aip.org/content/aip/journal/jcp/82/1/10.1063/1.448975`.

[97] M. Head-Gordon, R. J. Rico, M. Oumi, and T. J. Lee. A Doubles Correction to Electronic Excited States From Configuration Interaction in the Space of Single Substitutions. *Chem. Phys. Lett.*, 219(1):21–29, 1994. doi: 10.1016/0009-2614(94)00070-0. URL `http://www.sciencedirect.com/science/article/pii/0009261494000700`.

[98] M. Head-Gordon, M. Oumi, and D. Maurice. Quasidegenerate Second-order Perturbation Corrections to Single-excitation Configuration Interaction. *Mol. Phys.*, 96(4):593–602, 1999. doi: 10.1080/00268979909482996. URL `http://dx.doi.org/10.1080/00268979909482996`.

[99] D. Heiman, Y. Shapira, and S. Foner. Spin-Flip Raman Scattering and Magnetization Measurements on (Cd, Mn)S. *Solid State Commun.*, 45(10):899–902,

1983. doi: 10.1016/0038-1098(83)90331-9. URL `http://www.sciencedirect.com/science/article/pii/0038109883903319`.

[100] T. Helgaker, P. Jørgensen, and J. Olsen. *Molecular Electronic Structure Theory.* John Wiley & Sons, 1st edition, 2000. ISBN 9781119019558.

[101] A. Hellman, B. Razaznejad, and B. I. Lundqvist. Potential-Energy Surfaces for Excited States in Extended Systems. *J. Chem. Phys.*, 120(10):4593–4602, 2004. doi: 10.1063/1.1645787. URL `http://scitation.aip.org/content/aip/journal/jcp/120/10/10.1063/1.1645787`.

[102] K. W. Hipps and U. Mazur. $^4A_2 \rightarrow {}^4T_2$ and $^4A_2 \rightarrow {}^4T_1$ Electronic Transitions in Cobalt(II) Tetrachloride: An FT-IR and Inelastic Electron Tunneling Spectroscopy Study. *J. Am. Chem. Soc.*, 109(13):3861–3865, 1987. doi: 10.1021/ja00247a008. URL `http://dx.doi.org/10.1021/ja00247a008`.

[103] K. Hirao and H. Nakatsuji. A Generalization of the Davidson's Method to Large Nonsymmetric Eigenvalue Problems. *J. Comput. Phys.*, 45(2):246–254, 1982. doi: 10.1016/0021-9991(82)90119-X. URL `http://www.sciencedirect.com/science/article/pii/002199918290119X`.

[104] A. P. Hitchcock and C. E. Brion. K-shell Excitation Spectra of CO, N_2, and O_2. *J. Electron. Spectrosc. Relat. Phenom.*, 18(1):1–21, 1980. doi: 10.1016/0368-2048(80)80001-6. URL `http://www.sciencedirect.com/science/article/pii/0368204880800016`.

[105] P. Hohenberg and W. Kohn. Inhomogeneous Electron Gas. *Phys. Rev.*, 136:B864–B871, 1964. doi: 10.1103/PhysRev.136.B864. URL `http://link.aps.org/doi/10.1103/PhysRev.136.B864`.

[106] C. M. Isborn, X. Li, and J. C. Tully. TDDFT Ehrenfest Dynamics: Collisions Between Atomic Oxygen and Graphite Clusters. *J. Chem. Phys.*, 126(13):134307, 2007. doi:

10.1063/1.2713391. URL `http://scitation.aip.org/content/aip/journal/jcp/126/13/10.1063/1.2713391`.

[107] P. P. Jha and P. Guyot-Sionnest. Trion Decay in Colloidal Quantum Dots. *ACS Nano*, 3(4):1011–1015, 2009. doi: 10.1021/nn9001177. URL `http://dx.doi.org/10.1021/nn9001177`.

[108] H. Johansen and N. Andersen. The Spin Density and the Optical Spectrum of $CoCl_4^{2-}$. *Mol. Phys.*, 58(5):965–975, 1986. doi: 10.1080/00268978600101711. URL `http://dx.doi.org/10.1080/00268978600101711`.

[109] H. E. Johnson and C. M. Aikens. Electronic Structure and TDDFT Optical Absorption Spectra of Silver Nanorods. *J. Phys. Chem. A*, 113(16):4445–4450, 2009. doi: 10.1021/jp811075u. URL `http://dx.doi.org/10.1021/jp811075u`.

[110] R. O. Jones and O. Gunnarsson. The Density Functional Formalism, Its Applications and Prospects. *Rev. Mod. Phys.*, 61:689–746, 1989. doi: 10.1103/RevModPhys.61.689. URL `http://link.aps.org/doi/10.1103/RevModPhys.61.689`.

[111] J. Kauczor, P. Norman, O. Christiansen, and S. Coriani. Coupled-Cluster Response Theory for Near Edge X-ray Absorption Fine Structure of Atoms and Molecules. *Phys. Rev. A*, 85:022507, 2012. doi: 10.1103/PhysRevA.85.022507. URL `http://link.aps.org/doi/10.1103/PhysRevA.85.022507`.

[112] J. Kauczor, P. Norman, O. Christiansen, and S. Coriani. Communication: A Reduced-Space Algorithm for the Solution of the Complex Linear Response Equations Used in Coupled Cluster Damped Response Theory. *J. Chem. Phys.*, 139(21):211102, 2013. doi: 10.1063/1.4840275. URL `http://scitation.aip.org/content/aip/journal/jcp/139/21/10.1063/1.4840275`.

[113] A. Kerstin, P.-Å. Malmqvist, and B. O. Roos. Second-Order Perturbation Theory with A Complete Active Space Self-Consistent Field Reference Function. *J. Chem. Phys.*,

96(2):1218–1226, 1992. doi: 10.1063/1.462209. URL `http://scitation.aip.org/content/aip/journal/jcp/96/2/10.1063/1.462209`.

[114] H. Kisch. *Semiconductor Photocatalysis: Principles and Applications*. John Wiley & Sons, 2014. ISBN 9783527673339.

[115] V. I. Klimov, J. A. McGuire, R. D. Schaller, and V. I. Rupasov. Scaling of Multiexciton Lifetimes in Semiconductor Nanocrystals. *Phys. Rev. B*, 77:195324, 2008. doi: 10.1103/PhysRevB.77.195324. URL `http://link.aps.org/doi/10.1103/PhysRevB.77.195324`.

[116] H. Koch and P. Jørgensen. Coupled Cluster Response Functions. *J. Chem. Phys.*, 93(5):3333–3344, 1990. doi: 10.1063/1.458814. URL `http://scitation.aip.org/content/aip/journal/jcp/93/5/10.1063/1.458814`.

[117] W. Kohn and et al. *Reviews in Modern Quantum Chemistry: A Celebration of the Contributions of R. G. Parr*. World Scientific, 2002. ISBN 9789810248895.

[118] W. Kohn and L. J. Sham. Self-Consistent Equations Including Exchange and Correlation Effects. *Phys. Rev.*, 140:A1133–A1138, 1965. doi: 10.1103/PhysRev.140.A1133. URL `http://link.aps.org/doi/10.1103/PhysRev.140.A1133`.

[119] L. Kong, F. A. Bischoff, and E. F. Valeev. Explicitly Correlated R12/F12 Methods for Electronic Structure. *Chem. Rev.*, 112(1):75–107, 2012. doi: 10.1021/cr200204r. URL `http://dx.doi.org/10.1021/cr200204r`.

[120] G. Konstantatos and E. H. Sargent, editors. *Colloidal Quantum Dot Optoelectronics and Photovoltaics*. Cambridge University Press, 2013. ISBN 9780521198264.

[121] T. D. Krauss and J. J. Peterson. Bright Future for Fluorescence Blinking in Semiconductor Nanocrystals. *J. Phys. Chem. Lett.*, 1(9):1377–1382, 2010. doi: 10.1021/jz100321z. URL `http://dx.doi.org/10.1021/jz100321z`.

[122] C. M. Krauter, J. Schirmer, C. R. Jacob, M. Pernpointner, and A. Dreuw. Plasmons in Molecules: Microscopic Characterization Based on Orbital Transitions and Momentum Conservation. *J. Chem. Phys.*, 141(10):104101, 2014. doi: 10.1063/1.4894266. URL `http://scitation.aip.org/content/aip/journal/jcp/141/10/10.1063/1.4894266`.

[123] L. D. Landau and E. M. Lifshitz. *Quantum Mechanics: Non-Relativistic Theory*. Elsevier Science, 3rd edition, 1981. ISBN 9780080503486.

[124] D. W. Langer and H. J. Richter. Zero-Phonon Lines and Phonon Coupling of ZnSe: Mn and CdS: Mn. *Phys. Rev.*, 146:554–557, 1966. doi: 10.1103/PhysRev.146.554. URL `http://link.aps.org/doi/10.1103/PhysRev.146.554`.

[125] J. M. Langer. Where the Metal-Semiconductor Junction Emits Light. *J. Lumin.*, 23(1):141–154, 1981. doi: 10.1016/0022-2313(81)90194-0. URL `http://www.sciencedirect.com/science/article/pii/0022231381901940`.

[126] J. M. Langer, A. Lemańska-Bajorek, and A. Suchocki. A Method of Excitation Profiling in High-Field Electroluminescence. *Appl. Phys. Lett.*, 39(5):386–388, 1981. doi: 10.1063/1.92739. URL `http://scitation.aip.org/content/aip/journal/apl/39/5/10.1063/1.92739`.

[127] C. Lee, W. Yang, and R. G. Parr. Development of the Colle-Salvetti Correlation-Energy Formula into A Functional of the Electron Density. *Phys. Rev. B*, 37:785–789, 1988. doi: 10.1103/PhysRevB.37.785. URL `http://link.aps.org/doi/10.1103/PhysRevB.37.785`.

[128] P. J. Lestrange, P. D. Nguyen, and X. Li. Calibration of Energy-Specific TDDFT for Modeling K-edge XAS Spectra of Light Elements. *J. Chem. Theor. Comput.*, 11(7):2994–2999, 2015. doi: 10.1021/acs.jctc.5b00169. URL `http://dx.doi.org/10.1021/acs.jctc.5b00169`.

[129] A. B. P. Lever. *Inorganic Electronic Spectroscopy.* Elsevier, 1984. ISBN 9780444416995.

[130] X. Li, J. M. Millam, Scuseria. G. E., M. J. Frisch, and H. B. Schlegel. Density Matrix Search Using Direct Inversion in the Iterative Subspace As A Linear Scaling Alternative To Diagonalization in Electronic Structure Calculations. *J. Chem. Phys.*, 119(15):7651–7658, 2003. doi: http://dx.doi.org/10.1063/1.1607961. URL `http://scitation.aip.org/content/aip/journal/jcp/119/15/10.1063/1.1607961`.

[131] X. Li, S. M. Smith, A. N. Markevitch, D. A. Romanov, R. J. Levis, and H. B. Schlegel. A Time-dependent Hartree-Fock Approach for Studying the Electronic Optical Response of Molecules in Intense Fields. *Phys. Chem. Chem. Phys.*, 7:233–239, 2005. doi: 10.1039/B415849K. URL `http://dx.doi.org/10.1039/B415849K`.

[132] X. Li, C. L. Moss, W. Liang, and Y. Feng. Car-Parrinello Density Matrix Search with A First Principles Fictitious Electron Mass Method for Electronic Wave Function Optimization. *J. Chem. Phys.*, 130(23):234115, 2009. doi: 10.1063/1.3155082. URL `http://scitation.aip.org/content/aip/journal/jcp/130/23/10.1063/1.3155082`.

[133] W. Liang, H. Wang, J. Hung, X. Li, and M. J. Frisch. Eigenspace Update for Molecular Geometry Optimization in Nonredundant Internal Coordinate. *J. Chem. Theor. Comput.*, 6(7):2034–2039, 2010. doi: 10.1021/ct100214x. URL `http://dx.doi.org/10.1021/ct100214x`.

[134] W. Liang, C. T. Chapman, and X. Li. Efficient first-principles electronic dynamics. *J. Chem. Phys.*, 134(18):184102, 2011. doi: 10.1063/1.3589144. URL `http://scitation.aip.org/content/aip/journal/jcp/134/18/10.1063/1.3589144`.

[135] W. Liang, S. A. Fischer, M. J. Frisch, and X. Li. Energy-Specific Linear Response TDHF/TDDFT for Calculating High-Energy Excited States. *J. Chem. Theor. Comput.*, 7(11):3540–3547, 2011. doi: 10.1021/ct200485x. URL `http://dx.doi.org/10.1021/ct200485x`.

[136] Z. Lin, H. Li, A. Franceschetti, and M. T. Lusk. Efficient exciton transport between strongly quantum-confined silicon quantum dots. *ACS Nano*, 6(5):4029–4038, 2012. doi: 10.1021/nn3003407. URL `http://dx.doi.org/10.1021/nn3003407`.

[137] P.-L. Lions. Solutions of Hartree-Fock Equations for Coulomb Systems. *Commun. Math. Phys.*, 109(1):33–97, 1987. doi: 10.1007/BF01205672. URL `http://dx.doi.org/10.1007/BF01205672`.

[138] K. Lopata and N. Govind. Modeling Fast Electron Dynamics with Real-Time Time-Dependent Density Functional Theory: Application to Small Molecules and Chromophores. *J. Chem. Theor. Comput.*, 7(5):1344–1355, 2011. doi: 10.1021/ct200137z. URL `http://dx.doi.org/10.1021/ct200137z`.

[139] K. Lopata, B. E. Van Kuiken, M. Khalil, and N. Govind. Linear-Response and Real-Time Time-Dependent Density Functional Theory Studies of Core-Level Near Edge X-ray Absorption. *J. Chem. Theor. Comput.*, 8(9):3284–3292, 2012. doi: 10.1021/ct3005613. URL `http://dx.doi.org/10.1021/ct3005613`.

[140] P. O. Löwdin. On the Nonorthogonality Problem Connected with the Use of Atomic Wave Functions in the Theory of Molecules and Crystals. *J. Chem. Phys.*, 18(3):365–375, 1950. doi: 10.1063/1.1747632. URL `http://scitation.aip.org/content/aip/journal/jcp/18/3/10.1063/1.1747632`.

[141] P. O. Löwdin. Studies in Perturbation Theory: Part I. An Elementary Iteration-Variation Procedure for Solving the Schrödinger Equation by Partitioning Technique. *J. Mol. Spectrosc.*, 10(1):12–33, 1963. doi: 10.1016/0022-2852(63)90151-6. URL `http://www.sciencedirect.com/science/article/pii/0022285263901516`.

[142] P. O. Löwdin. *Proceedings of An Advanced Seminar on Perturbation Theory and Its Applications in Quantum Mechanics*. Wiley, New York, 1966.

[143] P. O. Löwdin. On the Nonorthogonality Problem. *Adv. Quantum Chem.*, 5:185–199, 1970. doi: 10.1016/S0065-3276(08)60339-1. URL `http://www.sciencedirect.com/science/article/pii/S0065327608603391`.

[144] Y. Ma, C. T. Chen, G. Meigs, K. Randall, and F. Sette. High-Resolution K-shell Photoabsorption Measurements of Simple Molecules. *Phys. Rev. A*, 44:1848–1858, 1991. doi: 10.1103/PhysRevA.44.1848. URL `http://link.aps.org/doi/10.1103/PhysRevA.44.1848`.

[145] J. M. Maestre, X. Lopez, C. Bo, and J. M. Poblet. A DFT Study of the Electronic Spectrum of the α-Keggin Anion $[\mathrm{Co}^{II}\mathrm{W}_{12}\mathrm{O}_{40}]^{6-}$. *Inorg. Chem.*, 41(7):1883–1888, 2002. doi: 10.1021/ic0110676. URL `http://dx.doi.org/10.1021/ic0110676`.

[146] G. D. Mahan. Excitons in Metals. *Phys. Rev. Lett.*, 18:448–450, 1967. doi: 10.1103/PhysRevLett.18.448. URL `http://link.aps.org/doi/10.1103/PhysRevLett.18.448`.

[147] D. C. Marinica, A. K. Kazansky, P. Nordlander, J. Aizpurua, and A. G. Borisov. Quantum Plasmonics: Nonlinear Effects in the Field Enhancement of a Plasmonic Nanoparticle Dimer. *Nano Lett.*, 12(3):1333–1339, 2012. doi: 10.1021/nl300269c. URL `http://dx.doi.org/10.1021/nl300269c`.

[148] M. A. L. Marques, A. Castro, G. F. Bertsch, and A. Rubio. Octopus: A First-Principles Tool for Excited Electron-Ion Dynamics. *Comp. Phys. Comm.*, 151(1):60–78, 2003. doi: 10.1016/S0010-4655(02)00686-0. URL `http://www.sciencedirect.com/science/article/pii/S0010465502006860`.

[149] R. L. Martin. Natural Transition Orbitals. *J. Chem. Phys.*, 118(11):4775–4777, 2003. doi: 10.1063/1.1558471. URL `http://scitation.aip.org/content/aip/journal/jcp/118/11/10.1063/1.1558471`.

[150] J. M. O. Matos, B. O. Roos, and P.-Å. Malmqvist. A CASSCF-CCI Study of the Valence and Lower Excited States of the Benzene Molecule. *J. Chem. Phys.*, 86(3): 1458–1466, 1987. doi: 10.1063/1.452235. URL `http://scitation.aip.org/content/aip/journal/jcp/86/3/10.1063/1.452235`.

[151] J. J. W. McDouall, K. Peasley, and M. A. Robb. A Simple MC SCF Perturbation Theory: Orthogonal Valence Bond Møller-Plesset 2 (OVB MP2). *Chem. Phys. Lett.*, 148(2):183–189, 1988. doi: 10.1016/0009-2614(88)80296-3. URL `http://www.sciencedirect.com/science/article/pii/0009261488802963`.

[152] L. E. McMurchie and E. R. Davidson. Configuration Interaction Calculations on the Planar $^1(\pi,\pi^*)$ State of Ethylene. *J. Chem. Phys.*, 66(7):2959–2971, 1977. doi: 10.1063/1.434364. URL `http://scitation.aip.org/content/aip/journal/jcp/66/7/10.1063/1.434364`.

[153] R. McWeeny. Some Recent Advances in Density Matrix Theory. *Rev. Mod. Phys.*, 32: 335–369, 1960. doi: 10.1103/RevModPhys.32.335. URL `http://link.aps.org/doi/10.1103/RevModPhys.32.335`.

[154] R. McWeeny and B. T. Sutcliffe. *Methods of Molecular Quantum Mechanics.* Academic Press, London, 1992. ISBN 9780124865525.

[155] I. A. Merkulov, D. R. Yakovlev, A. Keller, W. Ossau, J. Geurts, A. Waag, G. Landwehr, G. Karczewski, T. Wojtowicz, and J. Kossut. Kinetic Exchange between the Conduction Band Electrons and Magnetic Ions in Quantum-Confined Structures. *Phys. Rev. Lett.*, 83, 1999. doi: 10.1103/PhysRevLett.83.1431. URL `http://link.aps.org/doi/10.1103/PhysRevLett.83.1431`.

[156] D. A. Micha. Density Matrix Treatment of Electronic Rearrangement. *Adv. Quantum Chem.*, 35:317–337, 1999. doi: 10.1016/S0065-3276(08)60466-9. URL `http://www.sciencedirect.com/science/article/pii/S0065327608604669`.

[157] D. A. Micha. Time-Dependent Many-Electron Treatment of Electronic Energy and Charge Transfer in Atomic Collisions. *J. Phys. Chem. A*, 103(38):7562–7574, 1999. doi: 10.1021/jp9906839. URL `http://dx.doi.org/10.1021/jp9906839`.

[158] D. A. Micha and K. Runge. Time-dependent many-electron approach to slow ion-atom collisions: The coupling of electronic and nuclear motions. *Phys. Rev. A*, 50: 322–336, 1994. doi: 10.1103/PhysRevA.50.322. URL `http://link.aps.org/doi/10.1103/PhysRevA.50.322`.

[159] A. Mijovilovich, L. G. M. Pettersson, S. Mangold, M. Janousch, J. Susini, M. Salome, F. M. F. De Groot, and B. M. Weckhuysen. The Interpretation of Sulfur K-edge XANES Spectra: A Case Study on Thiophenic and Aliphatic Sulfur Compounds. *J. Phys. Chem. A*, 113(12):2750–2756, 2009. doi: 10.1021/jp806823c. URL `http://dx.doi.org/10.1021/jp806823c`.

[160] J. M. Millam and G. E. Scuseria. Linear Scaling Conjugate Gradient Matrix Search as An Alternative to Diagonalization for First Principles Electronic Structure Calculations. *J. Chem. Phys.*, 106(13):5569–5577, 1997. doi: 10.1063/1.473579. URL `http://scitation.aip.org/content/aip/journal/jcp/106/13/10.1063/1.473579`.

[161] A. Mishra, R. K. Behera, P. K. Behera, B. K. Mishra, and G. B. Behera. Cyanines During the 1990s: A Review. *Chem. Rev.*, 100(6):1973–2011, 2000. doi: 10.1021/cr990402t. URL `http://dx.doi.org/10.1021/cr990402t`.

[162] C. Møller and M. S. Plesset. The Recombination of Ions and of Ions and Electrons in Gases. *Phys. Rev.*, 34:618–634, 1934. doi: 10.1103/PhysRev.34.618. URL `http://link.aps.org/doi/10.1103/PhysRev.34.618`.

[163] H. J. Monkhorst. Calculation of Properties With the Coupled-Cluster Method. *Int. J. Quant. Chem.*, 12(S11):421–432, 1977. doi: 10.1002/qua.560120850. URL `http://dx.doi.org/10.1002/qua.560120850`.

[164] K. Murata and H. Tanaka. Surface-Wetting Effects on the Liquid–Liquid Transition of A Single-Component Molecular Liquid. *Nat. Commun.*, 1, 2010. doi: 10.1038/ncomms1015. URL `http://dx.doi.org/10.1038/ncomms1015`.

[165] M. Nooijen and R. J. Bartlett. Description of Core-excitation Spectra by the Open-Shell Electron-Attachment Equation-of-Motion Coupled Cluster Method. *J. Chem. Phys.*, 102(17):6735–6756, 1995. doi: 10.1063/1.469147. URL `http://scitation.aip.org/content/aip/journal/jcp/102/17/10.1063/1.469147`.

[166] J. Nover and H. H. Schmidtke. Low Symmetry Ligand Field Splittings in Optical Spectra of Pseudotetrahedral Co(II) Complexes with Halogenide and Chalcogenide Ligands. *Chem. Phys.*, 241(2):179–191, 1999. doi: 10.1016/S0301-0104(98)00419-4. URL `http://www.sciencedirect.com/science/article/pii/S0301010498004194`.

[167] S. T. Ochsenbein, Y. Feng, K. M. Whitaker, E. Badaeva, W. K. Liu, X. Li, and D. R. Gamelin. Charge-Controlled Magnetism in Colloidal Doped Semiconductor Nanocrystals. *Nat. Nanotechnol.*, 4:681–687, 2009. doi: 10.1038/nnano.2009.221. URL `http://dx.doi.org/10.1038/nnano.2009.221`.

[168] G. Onida, L. Reinig, and A. Rubio. Electronic Excitations: Density-Functional versus Many-Body Green's-Function Approaches. *Rev. Mod. Phys.*, 74:601–659, 2002. doi: 10.1103/RevModPhys.74.601. URL `http://link.aps.org/doi/10.1103/RevModPhys.74.601`.

[169] B. N. Otto. *Computational Theoretical Organic Chemistry.* Nato Science Series C. Springer Netherlands, 1981. ISBN 9789400984721.

[170] J. P. Perdew, K. Burke, and M. Ernzerhof. Generalized Gradient Approximation Made Simple. *Phys. Rev. Lett.*, 77:3865–3868, 1996. doi: 10.1103/PhysRevLett.77.3865. URL `http://link.aps.org/doi/10.1103/PhysRevLett.77.3865`.

[171] M. Petersilka, U. J. Gossmann, and E. K. U. Gross. Excitation Energies from Time-Dependent Density-Functional Theory. *Phys. Rev. Lett.*, 76:1212–1215, 1996. doi: 10.1103/PhysRevLett.76.1212. URL `http://link.aps.org/doi/10.1103/PhysRevLett.76.1212`.

[172] O. Plekan, V. Feyer, R. Richter, M. Coreno, M. De Simone, K. C. Prince, A. B. Trofimov, E. V. Gromov, I. L. Zaytseva, and J. Schirmer. A Theoretical and Experimental Study of the Near Edge X-ray Absorption Fine Structure (NEXAFS) and X-ray Photoelectron Spectra (XPS) of Nucleobases: Thymine and Adenine. *Chem. Phys.*, 347(1–3):360–375, 2008. doi: 10.1016/j.chemphys.2007.09.021. URL `http://www.sciencedirect.com/science/article/pii/S0301010407004302`.

[173] E. Prodan and R. Car. Tunneling Conductance of Amine-Linked Alkyl Chains. *Nano Lett.*, 8(6):1771–1777, 2008. doi: 10.1021/nl8012133. URL `http://dx.doi.org/10.1021/nl8012133`.

[174] R. Püttner, I. Dominguez, T. J. Morgan, C. Cisneros, R. F. Fink, E. Rotenberg, T. Warwick, M. Domke, G. Kaindl, and A. S. Schlachter. Vibrationally Resolved O 1s Core-Excitation Spectra of CO and NO. *Phys. Rev. A*, 59:3415–3423, 1999. doi: 10.1103/PhysRevA.59.3415. URL `http://link.aps.org/doi/10.1103/PhysRevA.59.3415`.

[175] D. Rappoport and F. Furche. Property-Optimized Gaussian Basis Sets for Molecular Response Calculations. *J. Chem. Phys.*, 133(13):134105, 2010. doi: 10.1063/1.3484283. URL `http://scitation.aip.org/content/aip/journal/jcp/133/13/10.1063/1.3484283`.

[176] K. Ray, S. DeBeer George, E. I. Solomon, K. Wieghardt, and F. Neese. Description of the Ground-State Covalencies of the Bis(dithiolato) Transition-Metal Complexes From X-ray Absorption Spectroscopy and Time-Dependent Density-Functional Calculations.

Chem. Eur. J., 13(10):2783–2797, 2007. doi: 10.1002/chem.200601425. URL `http://dx.doi.org/10.1002/chem.200601425`.

[177] R. R. S. Reddy, M. Fayazuddin, G. S. Reddy, S. L. Reddy, P. S. Rao, B. J. Redy, and F. N. Garcia. Tetrahedral Site of Fe(III) and Cu(II) in Renierite. *Cryst. Res. Technol.*, 39(3):240–244, 2004. doi: 10.1002/crat.200310177. URL `http://dx.doi.org/10.1002/crat.200310177`.

[178] G. Remmers, M. Domke, A. Puschmann, T. Mandel, C. Xue, G. Kaindl, E. Hudson, and D. A. Shirley. High-Resolution K-shell Photoabsorption in Formaldehyde. *Phys. Rev. A*, 46:3935–3944, 1992. doi: 10.1103/PhysRevA.46.3935. URL `http://link.aps.org/doi/10.1103/PhysRevA.46.3935`.

[179] S. Rettrup. An Iterative Method for Calculating Several of the Extreme Eigensolutions of Large Real Non-Symmetric Matrices. *J. Comput. Phys.*, 45(1):100–107, 1982. doi: 10.1016/0021-9991(82)90104-8. URL `http://www.sciencedirect.com/science/article/pii/0021999182901048`.

[180] M. Rittby and R. J. Bartlett. An Open-Shell Spin-Restricted Coupled Cluster Method: Application to Ionization Potentials in Nitrogen. *J. Phys. Chem.*, 92(11):3033–3036, 1988. doi: 10.1021/j100322a004. URL `http://dx.doi.org/10.1021/j100322a004`.

[181] A. Rogach, editor. *Semiconductor Nanocrystal Quantum Dots: Synthesis, Assembly, Spectroscopy and Applications*. Springer ebook collection / Chemistry and Materials Science 2005-2008. Springer, 2008. ISBN 9783211752371.

[182] B. O. Roos. *The Complete Active Space Self-Consistent Field Method and its Applications in Electronic Structure Calculations*. John Wiley & Sons, 1987. ISBN 9780470142943. doi: 10.1002/9780470142943.ch7. URL `http://dx.doi.org/10.1002/9780470142943.ch7`.

[183] B. O. Roos, K. Andersson, and M. P. Fülscher. Towards An Accurate Molecular Orbital Theory for Excited States: the Benzene Molecule. *Chem. Phys. Lett.*, 192(1): 5–13, 1992. doi: 10.1016/0009-2614(92)85419-B. URL `http://www.sciencedirect.com/science/article/pii/000926149285419B`.

[184] E. Runge and E. K. U. Gross. Density-Functional Theory for Time-Dependent Systems. *Phys. Rev. Lett.*, 52:997–1000, 1984. doi: 10.1103/PhysRevLett.52.997. URL `http://link.aps.org/doi/10.1103/PhysRevLett.52.997`.

[185] J. Schirmer, A. B. Trofimov, K. J. Randall, J. Feldhaus, A. M. Bradshaw, Y. Ma, C. T. Chen, and F. Sette. K-shell Excitation of the Water, Ammonia, and Methane Molecules Using High-Resolution Photoabsorption Spectroscopy. *Phys. Rev. A*, 47: 1136–1147, 1993. doi: 10.1103/PhysRevA.47.1136. URL `http://link.aps.org/doi/10.1103/PhysRevA.47.1136`.

[186] J. A. Scholl, A. García-Etxarri, A. L. Koh, and J. A. Doinne. Observation of Quantum Tunneling Between Two Plasmonic Nanoparticles. *Nano Lett.*, 13(2):564–569, 2013. doi: 10.1021/nl304078v. URL `http://dx.doi.org/10.1021/nl304078v`.

[187] M. Schreiber, M. R. Silva-Junior, S. P. A. Sauer, and W. Thiel. Benchmarks for Electronically Excited States: CASPT2, CC2, CCSD, and CC3. *J. Chem. Phys.*, 128(13):134110, 2008. doi: 10.1063/1.2889385. URL `http://scitation.aip.org/content/aip/journal/jcp/128/13/10.1063/1.2889385`.

[188] K. L. Schuchardt, B. T. Didier, T. Elsethagen, L. Sun, V. Gurumoorthi, J. Chase, J. Li, and T. L. Windus. Basis Set Exchange: A Community Database for Computational Sciences. *J. Chem. Inf. Model*, 47(3):1045–1052, 2007. doi: 10.1021/ci600510j. URL `http://dx.doi.org/10.1021/ci600510j`.

[189] S. Sen, A. Shee, and D. Mukherjee. A Study of the Ionisation and Excitation Energies of Core Electrons Using A Unitary Group Adapted State Universal Approach. *Mol.*

Phys., 111(16–17):2625–2639, 2013. doi: 10.1080/00268976.2013.802384. URL `http://dx.doi.org/10.1080/00268976.2013.802384`.

[190] L. Serrano-Andrés, M. Merchán, I. Nebot-Gil, R. Lindh, and B. O. Roos. Towards An Accurate Molecular Orbital Theory for Excited States: Ethene, Butadiene, and Hexatriene. *J. Chem. Phys.*, 98(4):3151–3162, 1993. doi: 10.1063/1.465071. URL `http://scitation.aip.org/content/aip/journal/jcp/98/4/10.1063/1.465071`.

[191] S. E. Shadle, B. Hedman, K. O. Hodgson, and E. I. Solomon. Ligand K-edge X-ray Absorption Spectroscopic Studies: Metal-Ligand Covalency in A Series of Transition Metal Tetrachlorides. *J. Am. Chem. Soc.*, 117(8):2259–2272, 1995. doi: 10.1021/ja00113a015. URL `http://dx.doi.org/10.1021/ja00113a015`.

[192] I. Shavitt and R. J. Bartlett. *Many-Body Methods in Chemistry and Physics*. MBPT and Coupled-Cluster Theory. Cambridge University Press, 2009. ISBN 9780521818322.

[193] E. Shigemasa, K. Ueda, Y. Sato, T. Sasaki, and A. Yagishita. Symmetry-Resolved K-shell Photoabsorption Spectra of Free N_2 Molecules. *Phys. Rev. A*, 45:2915–2921, 1992. doi: 10.1103/PhysRevA.45.2915. URL `http://link.aps.org/doi/10.1103/PhysRevA.45.2915`.

[194] J. L. Skinner and D. Hsu. Pure Dephasing of A Two-Level System. *J. Phys. Chem.*, 90 (21):4931–4938, 1986. doi: 10.1021/j100412a013. URL `http://dx.doi.org/10.1021/j100412a013`.

[195] J. C. Slater and K. H. Johnson. Self-Consistent-Field $X\alpha$ Cluster Method for Polyatomic Molecules and Solids. *Phys. Rev. B*, 5:844–853, 1972. doi: 10.1103/PhysRevB.5.844. URL `http://link.aps.org/doi/10.1103/PhysRevB.5.844`.

[196] J.-W. Song, M. A. Watson, A. Nakata, and K. Hirao. Core-excitation Energy Calculations With a Long-range Corrected Hybrid Exchange-correlation Functional Including A Short-range Gaussian Attenuation (LCgau-BOP). *J. Chem. Phys.*, 129(18):

184113, 2008. doi: 10.1063/1.3010372. URL `http://scitation.aip.org/content/aip/journal/jcp/129/18/10.1063/1.3010372`.

[197] A. V. Soudackov, A. L. Tchougreeff, and Y. A. Misurkin. Electronic Structure and Optical Spectra of Transition Metal Complexes by the Effective Hamiltonian Method. *Theor. Chem. Acc.*, 83(5):389–416, 1992. doi: 10.1007/BF01113064. URL `http://dx.doi.org/10.1007/BF01113064`.

[198] J. F. Stanton and R. J. Bartlett. The Equation of Motion Coupled-Cluster Method. A Systematic Biorthogonal Approach to Molecular Excitation Energies, Transition Probabilities, and Excited State Properties. *J. Chem. Phys.*, 98(9):7029–7039, 1993. doi: 10.1063/1.464746. URL `http://scitation.aip.org/content/aip/journal/jcp/98/9/10.1063/1.464746`.

[199] J. F. Stanton and J. Gauss. Perturbative Treatment of the Similarity Transformed Hamiltonian in Equation-of-Motion Coupled-Cluster Approximations. *J. Chem. Phys.*, 103(3):1064–1076, 1995. doi: 10.1063/1.469817. URL `http://scitation.aip.org/content/aip/journal/jcp/103/3/10.1063/1.469817`.

[200] J. F. Stanton, J. Gauss, and R. J. Bartlett. On the Choice of Orbitals for Symmetry Breaking Problems with Application to Nitrogen Oxide (NO_3). *J. Chem. Phys.*, 97(8):5554–5559, 1992. doi: 10.1063/1.463762. URL `http://scitation.aip.org/content/aip/journal/jcp/97/8/10.1063/1.463762`.

[201] R. E. Stanton. Multiple Solutions to the Hartree-Fock Problem. I. General Treatment of Two-Electron Closed-Shell Systems. *J. Chem. Phys.*, 48(1):257–262, 1968. doi: 10.1063/1.1667913. URL `http://scitation.aip.org/content/aip/journal/jcp/48/1/10.1063/1.1667913`.

[202] V. N. Staroverov, G. E. Scuseria, J. Tao, and J. P. Perdew. Comparative Assessment of A New Nonempirical Density Functional: Molecules and Hydrogen-Bonded Complexes.

J. Chem. Phys., 119(23):12129–12135, 2003. doi: 10.1063/1.1626543. URL `http://scitation.aip.org/content/aip/journal/jcp/119/23/10.1063/1.1626543`.

[203] M. Stener, G. Fronzoni, and M. De Simone. Time Dependent Density Functional Theory of Core Electrons Excitations. *Chem. Phys. Lett.*, 373(1–2):115–123, 2003. doi: 10.1016/S0009-2614(03)00543-8. URL `http://www.sciencedirect.com/science/article/pii/S0009261403005438`.

[204] P. J. Stephens, F. J. Devlin, C. F. Chabalowski, and M. J. Frisch. Ab Initio Calculation of Vibrational Absorption and Circular Dichroism Spectra Using Density Functional Force Fields. *J. Phys. Chem.*, 98(45):11623–11627, 1994. doi: 10.1021/j100096a001. URL `http://dx.doi.org/10.1021/j100096a001`.

[205] J. Stöhr. *NEXAFS Spectroscopy.* Springer Series in Surface Sciences. Springer-Verlag, 1st edition, 1992. ISBN 9783540544224.

[206] R E Stratmann, G E Scuseria, and M J Frisch. An Efficient Implementation of Time-Dependent Density-Functional Theory for the Calculation of Excitation Energies of Large Molecules. *J. Chem. Phys.*, 109(19):8218–8224, 1998. doi: 10.1063/1.477483. URL `http://scitation.aip.org/content/aip/journal/jcp/09/19/10.1063/1.477483`.

[207] A. Suchocki and J. M. Langer. Auger Effect in the Mn^{2+} Luminescence of CdF_2:(Mn,Y) Crystals. *Phys. Rev. B*, 39:7905–7916, 1989. doi: 10.1103/PhysRevB.39.7905. URL `http://link.aps.org/doi/10.1103/PhysRevB.39.7905`.

[208] S. S. Sun and N. S. Sariciftci, editors. *Organic Photovoltaics: Mechanisms, Materials, and Devices.* Optical Science and Engineering. CRC Press, 2010. ISBN 9781420026351.

[209] A. Szabo and N. S. Ostlund. *Modern Quantum Chemistry: Introduction to Advanced Electronic Structure Theory.* Dover Publications, Mineola, NY, 1996.

[210] J. Tao, J. P. Perdew, V. N. Staroverov, and G. E. Scuseria. Climbing the Density Functional Ladder: Nonempirical Meta-Generalized Gradient Approximation Designed for Molecules and Solids. *Phys. Rev. Lett.*, 91:146401, 2003. doi: 10.1103/PhysRevLett.91.146401. URL `http://link.aps.org/doi/10.1103/PhysRevLett.91.146401`.

[211] M. N. Taran and G. R. Rossman. Optical Spectroscopic Study of Tuhualite and A Re-examination of the Beryl, Cordierite, and Osumilite Spectra. *Am. Mineral.*, 86(9): 973–980, 2001. doi: 10.2138/am-2001-8-903. URL `http://ammin.geoscienceworld.org/content/86/9/973.abstract`.

[212] T. K. Townsend. *Inorganic Metal Oxide Nanocrystal Photocatalysts for Solar Fuel Generation from Water.* Springer, 2014. ISBN 9783319052427.

[213] L. Triguero, O. Plashkevych, L. G. M. Pettersson, and H. Ågren. Separate State vs. Transition State Kohn-Sham Calculations of X-ray Photoelectron Binding Energies and Chemical Shifts. *J. Electron. Spectrosc. Relat. Phenom.*, 104(1–3):195–207, 1999. doi: 10.1016/S0368-2048(99)00008-0. URL `http://www.sciencedirect.com/science/article/pii/S0368204899000080`.

[214] A. B. Trofimov and J. Schirmer. An Efficient Polarization Propagator Approach to Valence Electron Excitation Spectra. *J. Phys. B*, 28(12):2299–2324, 1995. URL `http://stacks.iop.org/0953-4075/28/i=12/a=003`.

[215] A. B. Trofimov, T. E. Moskovskaya, E. V. Gromov, N. M. Vitkovskaya, and J. Schirmer. Core-Level Electronic Spectra in ADC(2) Approximation for Polarization Propagator: Carbon Monoxide and Nitrogen Molecules. *J. Struct. Chem.*, 41(3):483–494, 2000. doi: 10.1007/BF02742009. URL `http://dx.doi.org/10.1007/BF02742009`.

[216] M. Tronc, G. C. King, and F. H. Read. Carbon K-shell Excitation in Small Molecules by High-Resolution Electron Impact. *J. Phys. B*, 12(1):137–157, 1979. URL `http://stacks.iop.org/0022-3700/12/i=1/a=020`.

[217] M. Tronc, G. C. King, and F. H. Read. Nitrogen K-shell Excitation in N_2, NO and N_2O by High-Resolution Electron Energy-Loss Spectroscopy. *J. Phys. B*, 13(5):999–1008, 1980. URL `http://stacks.iop.org/0022-3700/13/i=5/a=025`.

[218] P. Čársky. *Configuration Interaction*. John Wiley & Sons, 2002. ISBN 9780470845011. doi: 10.1002/0470845015.cca036. URL `http://dx.doi.org/10.1002/0470845015.cca036`.

[219] J. H. Van Vleck. The Dirac Vector Model in Complex Spectra. *Phys. Rev.*, 45:405–419, 1934. doi: 10.1103/PhysRev.45.405. URL `http://link.aps.org/doi/10.1103/PhysRev.45.405`.

[220] W. R. Wadt and P. J. Hay. Ab initio Effective Core Potentials for Molecular Calculations. Potentials for Main Group Elements Na to Bi. *J. Chem. Phys.*, 82(1): 284–298, 1985. doi: 10.1063/1.448800. URL `http://scitation.aip.org/content/aip/journal/jcp/82/1/10.1063/1.448800`.

[221] L. W. Wang, M. Califno, A. Zunger, and A. Franceschetti. Pseudopotential Theory of Auger Processes in CdSe Quantum Dots. *Phys. Rev. Lett.*, 91:056404, 2003. doi: 10.1103/PhysRevLett.91.056404. URL `http://link.aps.org/doi/10.1103/PhysRevLett.91.056404`.

[222] Z. Wang, Z. Tu, and F. Wang. Equation-of-Motion Coupled-Cluster Theory for Excitation Energies of Closed-Shell Systems With Spin!Orbit Coupling. *J. Chem. Theor. Comput.*, 10(12):5567–5576, 2014. doi: 10.1021/ct500854m. URL `http://dx.doi.org/10.1021/ct500854m`.

[223] H. A. Weakliem. Optical Spectra of Ni^{2+}, Co^{2+}, and Cu^{2+} in Tetrahedral Sites in Crystals. *J. Chem. Phys.*, 36(8):2117–2140, 1962. doi: 10.1063/1.1732840. URL `http://scitation.aip.org/content/aip/journal/jcp/36/8/10.1063/1.1732840`.

[224] F. Weigend and R. Ahlrichs. Balanced Basis Sets of Split Valence, Triple Zeta Valence and Quadruple Zeta Valence Quality for H to Rn: Design and Assessment of Accuracy. *Phys. Chem. Chem. Phys.*, 7:3297–3305, 2005. doi: 10.1039/B508541A. URL `http://dx.doi.org/10.1039/B508541A`.

[225] H. Weihe and H. U. Güdel. Quantitative Interpretation of the Goodenough-Kanamori Rules: A Critical Analysis. *Inorg. Chem.*, 36(17):3632–3639, 1997. doi: 10.1021/ic961502+. URL `http://dx.doi.org/10.1021/ic961502+`.

[226] W. Werner Kutzelnigg. Present and Future Trends in Quantum Chemical Calculations. *J. Mol. Struct.: THEOCHEM*, 181(1):33–54, 1988. doi: 10.1016/0166-1280(88)80028-9. URL `http://www.sciencedirect.com/science/article/pii/0166128088800289`.

[227] M. A. White, A. L. Weaver, R. Beaulac, and D. R. Gamelin. Electrochemically Controlled Auger Quenching of Mn^{2+} Photoluminescence in Doped Semiconductor Nanocrystals. *ACS Nano*, 5(5):4158–4168, 2011. doi: 10.1021/nn200889q. URL `http://dx.doi.org/10.1021/nn200889q`.

[228] E. P. Wigner. Über die Erhaltungssätze in der Quantenmechanik. (German) [On Conservation in Quantum Mechanics]. *Nachr. Akad. Wiss. Gttingen, Math.-Phys. Kl.*, IIa: 375–381, 1927.

[229] P. J. Wilson, T. J. Bradley, and D. J. Tozer. Hybrid Exchange-Correlation Functional Determined From Thermochemical Data and Ab Initio Potentials. *J. Chem. Phys.*, 115(20):9233–9242, 2001. doi: 10.1063/1.1412605. URL `http://scitation.aip.org/content/aip/journal/jcp/115/20/10.1063/1.1412605`.

[230] D. E. Woon and T. H. Dunning. Gaussian Basis Sets for Use in Correlated Molecular Calculations. IV. Calculation of Static Electrical Response Properties. *J. Chem. Phys.*,

100(4):2975–2988, 1994. doi: 10.1063/1.466439. URL `http://scitation.aip.org/content/aip/journal/jcp/100/4/10.1063/1.466439`.

[231] D. E. Woon and T. H. Dunning. Gaussian Basis Sets for Use in Correlated Molecular Calculations. V. Core-Valence Basis Sets for Boron Through Neon. *J. Chem. Phys.*, 103(11):4572–4585, 1995. doi: 10.1063/1.470645. URL `http://scitation.aip.org/content/aip/journal/jcp/103/11/10.1063/1.470645`.

[232] R. W. G. Wyckoff. *Crystal Structures.* R. E. Krieger, Malabar, FL, 1982.

[233] K. Yabana and G. F. Bertsch. Time-dependent local-density approximation in real time. *Phys. Rev. B*, 54:4484–4487, 1996. doi: 10.1103/PhysRevB.54.4484. URL `http://link.aps.org/doi/10.1103/PhysRevB.54.4484`.

[234] P. Yannoulis, R. Dudde, K. H. Frank, and E. E. Koch. Orientation of Aromatic Hydrocarbons on Metal Surfaces as Determined by NEXAFS. *Surf. Sci.*, 189:519–528, 1987. doi: 10.1016/S0039-6028(87)80476-4. URL `http://www.sciencedirect.com/science/article/pii/S0039602887804764`.

[235] D. C. Young. *Computational Chemistry: A Practical Guide for Applying Techniques to Real World Problems.* John Wiley & Sons, 2001. ISBN 9780471333685.

[236] J. Zhao, G. Nair, B. R. Fisher, and M. G. Bawendi. Challenge to the Charging Model of Semiconductor-Nanocrystal Fluorescence Intermittency from Off-State Quantum Yields and Multiexciton Blinking. *Phys. Rev. Lett.*, 104:157403, 2010. doi: 10.1103/PhysRevLett.104.157403. URL `http://link.aps.org/doi/10.1103/PhysRevLett.104.157403`.

[237] J. Zuloaga, E. Prodan, and P. Nordlander. Quantum Description of the Plasmon Resonances of a Nanoparticle Dimer. *Nano Lett.*, 9(2):887–891, 2009. doi: 10.1021/nl803811g. URL `http://dx.doi.org/10.1021/nl803811g`.

Appendix A

PROPERTIES OF THE EIGENVALUES AND EIGENVECTORS IN A NONLINEAR VARIATIONAL PROBLEM

Consider a reference N-electron Slater determinant Φ_0:

$$\Phi_0 = \hat{A} \prod_i \phi_i^0(i) \tag{A.1}$$

where $\hat{A}$ is the antisymmetrizer and ϕ_i^0 occupied spin orbitals of the reference state. Here I label i, j, k, l as occupied orbital indices, a, b, c, d as unoccupied orbital indices, and p, q, r, s as all orbital indices.

The SCF procedure can be recast in the formalism of orbital rotation as a unitary transformation of all the spin orbitals:

$$\phi_p = \sum_q \phi_q^0 U_{qp} \tag{A.2}$$

where the unitary matrix $\mathbf{U}$ may be written in terms of an anti-Hermitian matrix $\mathbf{C}$

$$\mathbf{U} = \exp(-\mathbf{C}), \qquad \mathbf{C}^\dagger = -\mathbf{C} \tag{A.3}$$

$\mathbf{C}$ is also called the orbital rotation matrix, and it satisfies:

$$c_{ij} = c_{ab} = 0, \qquad \text{for all } i, j, a, b \tag{A.4}$$

It can be shown that the new Slater determinant that consists of the transformed orbitals can be expressed as

$$\Phi = \Phi_0 + \sum_{ia} c_{ia} \Phi_i^a + \frac{1}{2} \sum_{iajb} c_{ia} c_{jb} \Phi_{ij}^{ab} + \cdots \tag{A.5}$$

where $\Phi_i^a, \Phi_{ij}^{ab}, \ldots$ are the singly, doubly, $\ldots$ excited determinants with respect to the reference state Φ_0. Note that Eq. (A.5) is not the conventional CI type expansion. It has constraints on the expansion coefficients as products of rotational matrix elements.

To simplify the following equations, a change of notations can be made here, replacing ia index with I, K_{ia} as c_I, Φ_i^a as Φ_I and Φ_{ij}^{ab} as Φ_{IJ}, etc, then Eq. (A.5) can be rewritten as

$$\Phi = \Phi_0 + \sum_I c_I \Phi_I + \frac{1}{2} \sum_{IJ} c_I c_J \Phi_{IJ} + \cdots \, . \tag{A.6}$$

In the variational approach for the optimized determinant Φ, consider the energy functional

$$E[\Phi] = \frac{\langle \Phi | \hat{H} | \Phi \rangle}{\langle \Phi | \Phi \rangle} \tag{A.7}$$

Substituting Eq. (A.5) into the above expression gives

$$E(\mathbf{c}) = \frac{H_{00} + 2\mathbf{c}^\dagger \mathbf{S} + \mathbf{c}^\dagger \mathbf{D} \mathbf{c} + \cdots}{1 + \mathbf{c}^\dagger \mathbf{c} + \cdots} \tag{A.8}$$

where

$$H_{00} = \langle \Phi_0 | \, \hat{H} \, | \Phi_0 \rangle \, , \tag{A.9}$$

$$S_I = \langle \Phi_0 | \, \hat{H} \, | \Phi_I \rangle \, , \tag{A.10}$$

$$D_{IJ} = \langle \Phi_I | \, \hat{H} \, | \Phi_J \rangle + \langle \Phi_0 | \, \hat{H} \, | \Phi_{IJ} \rangle \, . \tag{A.11}$$

The existence of higher order terms in Eq. (A.8) indicates that the variation of $E(\mathbf{c})$ with respect to $\mathbf{c}$ is nonlinear. Mathematically, stationery points of Eq. (A.8) are usually characterized by their first and second order properties. If the energy functional is truncated up to second order in $\mathbf{c}$, Eq. (A.8) becomes

$$E(\mathbf{c}) \simeq \frac{H_{00} + 2\mathbf{c}^\dagger \mathbf{S} + \mathbf{c}^\dagger \mathbf{D} \mathbf{c}}{1 + \mathbf{c}^\dagger \mathbf{c}} = \frac{\begin{pmatrix} 1 & \mathbf{c}^\dagger \end{pmatrix} \begin{pmatrix} H_{00} & \mathbf{S}^\dagger \\ \mathbf{S} & \mathbf{D} \end{pmatrix} \begin{pmatrix} 1 \\ \mathbf{c} \end{pmatrix}}{1 + \mathbf{c}^\dagger \mathbf{c}}$$

The stationary point of the truncated energy functional occurs when the gradient $\mathbf{g}$ vanishes:

$$\mathbf{g} = \frac{\partial E}{\partial \mathbf{c}} = \frac{2 \begin{pmatrix} H_{00} & \mathbf{S}^\dagger \\ \mathbf{S} & \mathbf{D} \end{pmatrix} \begin{pmatrix} 1 \\ \mathbf{c} \end{pmatrix} - 2E \begin{pmatrix} 1 \\ \mathbf{c} \end{pmatrix}}{1 + \mathbf{c}^\dagger \mathbf{c}} = 0 \tag{A.12}$$

which leads to the usual eigenvalue problem

$$\tilde{\mathbf{H}}\mathbf{x} = E\mathbf{x} \tag{A.13}$$

where

$$\tilde{\mathbf{H}} = \begin{pmatrix} H_{00} & \mathbf{S}^\dagger \\ \mathbf{S} & \mathbf{D} \end{pmatrix} \tag{A.14}$$

$$\mathbf{x} = \begin{pmatrix} 1 \\ \mathbf{c} \end{pmatrix} \tag{A.15}$$

Therefore, the solutions of the variational Schrödinger equation amounts to the stationary points of the energy functional which has $N + 1$ number of roots where N is the dimension of $\mathbf{c}$.

The characteristics of these stationary points can be verified by evaluating the second derivatives, Hessian $\mathbf{h}$ given by

$$\mathbf{h} = \frac{\partial^2 E}{\partial \mathbf{c}^2} = -\frac{4(\tilde{\mathbf{H}}\mathbf{x} - E\mathbf{x})\mathbf{x}^\dagger}{(\mathbf{x}^\dagger\mathbf{x})^2} + \frac{2(\tilde{\mathbf{H}} - E\mathbf{I} + \mathbf{g}\mathbf{x}^\dagger)}{\mathbf{x}^\dagger\mathbf{x}} \tag{A.16}$$

where $\mathbf{I}$ is the identity matrix. In deriving Eq. (A.12) and Eq. (A.16) the usual convention for matrix/vector differentiations have been used.

At stationary points, the Hessian becomes:

$$\mathbf{h}|_{\mathbf{g}=0} = \frac{2(\tilde{\mathbf{H}} - E\mathbf{I})}{\mathbf{x}^\dagger\mathbf{x}} \tag{A.17}$$

When expressed in the normalized eigenspace of the matrix $\tilde{\mathbf{H}}$, the Hessian becomes:

$$\mathbf{h}'|_{\mathbf{g}=0} = \begin{pmatrix} E_0 - E & 0 & \cdots & 0 \\ 0 & E_1 - E & \cdots & 0 \\ \vdots & \vdots & \ddots & \vdots \\ 0 & \cdots & 0 & E_M - E \end{pmatrix} \tag{A.18}$$

where E_0 stands for the ground state energy, E_i the i-th excited state energy. It is easy to see that at the ground state (i.e. when $E = E_0$) all the diagonal elements of the Hessian are non-negative, which implies a minimum, whereas at i-th excited state (i.e. when $E = E_i$) there are i negative diagonal elements in the Hessian, indicating an i-th saddle point.

Appendix B

RELATIONSHIP BETWEEN TWO TYPES OF EXCHANGE INTERACTIONS IN MN^{2+}-DOPED SEMICONDUCTORS

The initial state of the system under consideration consists of one e_{CB} and a Mn^{2+} center in the $^4\mathrm{T}_1$ configuration, which has two spin-up Mn^{2+}-3d electrons with t_2 symmetry, two spin-up Mn^{2+}-3d electrons with e symmetry and one spin-down d electron, also in the e-subshell (Mn^{2+} $d^5[e(\alpha)^2 e(\beta)^1 t(\alpha)^2]$). When e_{CB} is in the $\alpha(\beta)$ state and parallel (anti-parallel) to the majority spin at the Mn^{2+} center, the total energy of the ferromagnetic (anti-ferromagnetic) state is

$$\begin{aligned}
E^{\mathrm{FM}}_{^4\mathrm{T}_1 - e_{\mathrm{CB}}} = & \sum_{i=e(\alpha,\beta),t_2(\alpha,\beta)} h_{d_i} + h_{e_{\mathrm{CB}(\alpha)}} \\
& + \sum_{\substack{i,j=e(\alpha,\beta),t_2(\alpha,\beta) \\ i\neq j}} \langle \Psi_{d_i}(\mathbf{r}_1)\Psi_{d_j}(\mathbf{r}_2)|\frac{1}{\mathbf{r}_{12}}|\Psi_{d_i}(\mathbf{r}_1)\Psi_{d_j}(\mathbf{r}_2)\rangle \\
& + \sum_{i=e(\alpha,\beta),t_2(\alpha,\beta)} \langle \Psi_{d_i}(\mathbf{r}_1)\Psi_{e_{\mathrm{CB}(\alpha)}}(\mathbf{r}_2)|\frac{1}{\mathbf{r}_{12}}|\Psi_{d_i}(\mathbf{r}_1)\Psi_{e_{\mathrm{CB}(\alpha)}}(\mathbf{r}_2)\rangle \\
& - \sum_{\substack{i,j=e(\alpha),t_2(\alpha) \\ i\neq j}} \langle \Psi_{d_i}(\mathbf{r}_1)\Psi_{d_j}(\mathbf{r}_2)|\frac{1}{\mathbf{r}_{12}}|\Psi_{d_i}(\mathbf{r}_2)\Psi_{d_j}(\mathbf{r}_1)\rangle) \\
& - \sum_{i=e(\alpha),t_2(\alpha)} \langle \Psi_{d_i}(\mathbf{r}_1)\Psi_{e_{\mathrm{CB}(\alpha)}}(\mathbf{r}_2)|\frac{1}{\mathbf{r}_{12}}|\Psi_{d_i}(\mathbf{r}_2)\Psi_{e_{\mathrm{CB}(\alpha)}}(\mathbf{r}_1)\rangle,
\end{aligned} \tag{B.1}$$

$$\begin{aligned}
E^{\mathrm{AFM}}_{^4\mathrm{T}_1-e_{\mathrm{CB}}} = & \sum_{i=e(\alpha,\beta),t_2(\alpha,\beta)} h_{d_i} + h_{e_{\mathrm{CB}}(\beta)} \\
& + \sum_{\substack{i,j=e(\alpha,\beta),t_2(\alpha,\beta)\\ i\neq j}} \langle \Psi_{d_i}(\mathbf{r}_1)\Psi_{d_j}(\mathbf{r}_2)|\frac{1}{\mathbf{r}_{12}}|\Psi_{d_i}(\mathbf{r}_1)\Psi_{d_j}(\mathbf{r}_2)\rangle \\
& + \sum_{i=e(\alpha,\beta),t_2(\alpha,\beta)} \langle \Psi_{d_i}(\mathbf{r}_1)\Psi_{e_{\mathrm{CB}}(\beta)}(\mathbf{r}_2)|\frac{1}{\mathbf{r}_{12}}|\Psi_{d_i}(\mathbf{r}_1)\Psi_{e_{\mathrm{CB}}(\beta)}(\mathbf{r}_2)\rangle \\
& - \sum_{\substack{i,j=e(\alpha),t_2(\alpha)\\ i\neq j}} \langle \Psi_{d_i}(\mathbf{r}_1)\Psi_{d_j}(\mathbf{r}_2)|\frac{1}{\mathbf{r}_{12}}|\Psi_{d_i}(\mathbf{r}_2)\Psi_{d_j}(\mathbf{r}_1)\rangle \\
& - \langle \Psi_{d_e(\beta)}(\mathbf{r}_1)\Psi_{e_{\mathrm{CB}}(\beta)}(\mathbf{r}_2)|\frac{1}{\mathbf{r}_{12}}|\Psi_{d_e(\beta)}(\mathbf{r}_2)\Psi_{e_{\mathrm{CB}}(\beta)}(\mathbf{r}_1)\rangle, \qquad \text{(B.2)}
\end{aligned}$$

where h is the one-electron energy including kinetic energy and electron-nuclear Coulombic attractions. The exchange splitting is defined as the difference between Eq. (B.1) and Eq. (B.2),

$$\begin{aligned}
E^{s-d}_{^4\mathrm{T}_1-e_{\mathrm{CB}}} = & E^{\mathrm{AFM}}_{^4\mathrm{T}_1-e_{\mathrm{CB}}} - E^{\mathrm{FM}}_{^4\mathrm{T}_1-e_{\mathrm{CB}}} \\
\approx & \sum_{i=e(\alpha),t_2(\alpha)} \langle \Psi_{d_i}(\mathbf{r}_1)\Psi_{e_{\mathrm{CB}}(\alpha)}(\mathbf{r}_2)|\frac{1}{\mathbf{r}_{12}}|\Psi_{d_i}(\mathbf{r}_2)\Psi_{e_{\mathrm{CB}}(\alpha)}(\mathbf{r}_1)\rangle \\
& - \langle \Psi_{d_e(\beta)}(\mathbf{r}_1)\Psi_{e_{\mathrm{CB}}(\beta)}(\mathbf{r}_2)|\frac{1}{\mathbf{r}_{12}}|\Psi_{d_e(\beta)}(\mathbf{r}_2)\Psi_{e_{\mathrm{CB}}(\beta)}(\mathbf{r}_1)\rangle. \qquad \text{(B.3)}
\end{aligned}$$

where one-electron energies and electron-electron Coulombic interactions are considered the same in FM and AFM configurations. K_1 from Eq. (3.7) is the sum $\sum_{i=e(\alpha),t_2(\alpha)}^{4} \langle \Psi_{d_i}(\mathbf{r}_1)\Psi_{e_{\mathrm{CB}}(\alpha)}(\mathbf{r}_2)|\frac{1}{\mathbf{r}_{12}}|\Psi_{d_i}(\mathbf{r}_2)\Psi_{e_{\mathrm{CB}}(\alpha)}(\mathbf{r}_1)\rangle$; the second term of Eq. (B.3) takes on a similar spatial integral with summation over a different spin-state. Since

$$\begin{aligned}
& \langle \Psi_{d_e(\beta)}(\mathbf{r}_1)\Psi_{e_{\mathrm{CB}}(\beta)}(\mathbf{r}_2)|\frac{1}{\mathbf{r}_{12}}|\Psi_{d_e(\beta)}(\mathbf{r}_2)\Psi_{e_{\mathrm{CB}}(\beta)}(\mathbf{r}_1)\rangle \\
& \qquad \approx \frac{1}{4} \sum_{i=e(\alpha),t_2(\alpha)} \langle \Psi_{d_i}(\mathbf{r}_1)\Psi_{e_{\mathrm{CB}}(\alpha)}(\mathbf{r}_2)|\frac{1}{\mathbf{r}_{12}}|\Psi_{d_i}(\mathbf{r}_2)\Psi_{e_{\mathrm{CB}}(\alpha)}(\mathbf{r}_1)\rangle, \qquad \text{(B.4)}
\end{aligned}$$

for the $^4\mathrm{T}_1$-e_{CB} interaction, Eq. (B.6) follows.

$$E^{s-d}_{^4\mathrm{T}_1-e_{\mathrm{CB}}} \approx \frac{3}{4}K_1. \qquad \text{(B.5)}$$

Following a similar procedure, it is easy to show that

$$E^{s-d}_{^6\mathrm{A}_1-e_{\mathrm{CB}}} \approx K_2 \tag{B.6}$$

for $K_2 = \sum_{i=e(\alpha),t_2(\alpha)}^{5} \langle \Psi_{d_i}(\mathbf{r}_1)\Psi_{e'_{\mathrm{CB}}(\alpha)}(\mathbf{r}_2)|\frac{1}{\mathbf{r}_{12}}|\Psi_{d_i}(\mathbf{r}_2)\Psi_{e'_{\mathrm{CB}}(\alpha)}(\mathbf{r}_1)\rangle$. If the electron density distribution is the same at the conduction band edge and at a higher energy excited state ($|\Psi_{e_{\mathrm{CB}}}|^2 \simeq |\Psi_{e'_{\mathrm{CB}}}|^2$), K_1 and K_2 can be considered linearly dependent, $5K_1 \simeq 4K_2$, and Eq. (3.7) approaches equality. This assumption is valid in a bulk system where e_{CB} are associated with plane-wave type wave functions. However, in a quantized system, the electron wave function at the band edge and at the excited state may be very different.[34, 53] From the two-center kinetic-exchange mechanism point of view,[19, 225, 155] the largest contribution in K_1 and K_2 comes from hybridization of e_{CB} or e'_{CB} with Mn^{2+}-4s levels, and it is possible that the Mn^{2+}(4 s,p) hybridized levels are contributing in the case of e'_{CB}, due to the high energy of the e'_{CB} state. The exchange coupling constants for $^6\mathrm{A}_1$-e'_{CB} and $^4\mathrm{T}_1$-e_{CB} can be evaluated by,

$$J^{s-d}_{^6\mathrm{A}_1-e'_{\mathrm{CB}}} = \frac{V^2_{ss'}}{2(S_{^6\mathrm{A}_1}+1/2)} \cdot \frac{E_{4s(\alpha)} - E_{4s(\beta)}}{(E_{4s(\alpha)} - E_{e'_{\mathrm{CB}}}) \cdot (E_{4s(\beta)} - E_{e'_{\mathrm{CB}}})}, \tag{B.7}$$

$$J^{s-d}_{^4\mathrm{T}_1-e_{\mathrm{CB}}} = \frac{V^2_{s's}}{2(S_{^4\mathrm{T}_1}+1/2)} \cdot \frac{E_{4s'(\alpha)} - E_{4s'(\beta)}}{(E_{4s'(\alpha)} - E_{e_{\mathrm{CB}}}) \cdot (E_{4s'(\beta)} - E_{e_{\mathrm{CB}}})}, \tag{B.8}$$

where V is the transfer integral, related to the interaction strength between the Mn^{2+}-4s level and e_{CB} electron. In the case of Eq. (B.7), $V_{ss'}$ describes the interaction between Mn^{2+}(4s) level in the $^6\mathrm{A}_1$ configuration and the e'_{CB}, while corresponds to the interaction between Mn^{2+}(4s) levels in the $^4\mathrm{T}_1$ configuration and the e_{CB} (Eq. (B.8)). The ratio between Eq. (B.7) and Eq. (B.8) is

$$\begin{aligned}
\frac{J^{s-d}_{^6\mathrm{A}_1-e'_{\mathrm{CB}}}}{J^{s-d}_{^4\mathrm{T}_1-e_{\mathrm{CB}}}} =& \frac{(S_{^4\mathrm{T}_1}+1/2)V^2_{ss'}}{(S_{^6\mathrm{A}_1}+1/2)V^2_{s's}} \cdot \frac{(E_{4s(\alpha)} - E_{4s(\beta)})(E_{4s'(\alpha)} - E_{e_{\mathrm{CB}}})(E_{4s'(\beta)} - E_{e_{\mathrm{CB}}})}{(E_{4s'(\alpha)} - E_{4s'(\beta)})(E_{4s(\alpha)} - E_{e'_{\mathrm{CB}}})(E_{4s(\beta)} - E_{e'_{\mathrm{CB}}})} \\
=& A \cdot \frac{V^2_{ss'}}{V^2_{s's}} \cdot \frac{(E_{4s'(\alpha)} - E_{e_{\mathrm{CB}}})(E_{4s'(\beta)} - E_{e_{\mathrm{CB}}})}{(E_{4s(\alpha)} - E_{e'_{\mathrm{CB}}})(E_{4s(\beta)} - E_{e'_{\mathrm{CB}}})},
\end{aligned} \tag{B.9}$$

where all parameters that are intrinsic to the dopant center ($S_{^6\mathrm{A}_1}$, $S_{^4\mathrm{T}_1}$, E_{4s}, $E_{4s'}$) are replaced by a constant A. During the Auger de-excitation process, the total energy has to be conserved. Therefore, $E_{e'_{\mathrm{CB}}} = E_{e_{\mathrm{CB}}} + \Delta E(^4\mathrm{T}_1 \rightarrow {}^6\mathrm{A}_1)$ and the transition energy at the dopant center $\Delta E(^4\mathrm{T}_1 \rightarrow {}^6\mathrm{A}_1)$ can be considered as constant. This leads to a further reduction of Eq. (B.9) to

$$\frac{J^{s-d}_{^6\mathrm{A}_1 - e'_{\mathrm{CB}}}}{J^{s-d}_{^4\mathrm{T}_1 - e_{\mathrm{CB}}}} = A \cdot \frac{V^2_{ss'}}{V^2_{s's}}. \tag{B.10}$$

Eq. (B.10) gives a relationship between the two exchange coupling constants that contribute to the Auger de-excitation process in Mn^{2+}-doped semiconductors. In large nanocrystals or bulk, $V_{ss'}$ and $V_{s's}$ can be estimated using Harrison's tight-binding approach,[19, 94] and can be shown to approach constants. As a result, Eq. (B.10) becomes a constant as well, suggesting that $J^{s-d}_{^6\mathrm{A}_1 - e'_{\mathrm{CB}}}$ and $J^{s-d}_{^4\mathrm{T}_1 - e_{\mathrm{CB}}}$ are linearly dependent, and Eq. (3.7) takes on the equality form. If Eq. (B.10) approaches a constant as the size of the system increases, Eq. (3.7) becomes a good estimate for the exchange-type coupling in the Auger process, otherwise it represents the upper bound.

Appendix C

ERROR ANALYSIS OF MODIFIED MIDPOINT UNITARY TRANSFORMATION (MMUT) FOR THE DENSITY MATRIX PROPOGATION

The MMUT[131, 106] used to propagate the density matrix in RT-TDDFT was originally developed based on the "relax and drive" method proposed by Micha[157, 156, 158] for efficiently integrating time-dependent Hartree-Fock (TDHF) equations. Basically, the new density matrix is obtained in a two-step procedure. In the relax step, the approximation of the new density matrix is obtained from a unitary transformation of an old one,

$$\tilde{\mathbf{P}}^{(0)}_{t_{n+1}} = \mathbf{U}_{t_n}\mathbf{P}_{t_n}\mathbf{U}^{\dagger}_{t_n} = \exp(-i \cdot \Delta t \cdot \mathbf{K}_{t_n})\ \mathbf{P}_{t_n}\ \exp(i \cdot \Delta t \cdot \mathbf{K}_{t_n}). \tag{C.1}$$

Then, in the drive step, a first-order perturbation correction to the $\tilde{\mathbf{P}}^{(0)}_{t_{n+1}}$ is computed via

$$\begin{aligned} \Delta\mathbf{P}_{t_{n+1}} &= \int_{t_n}^{t_{n+1}} \mathrm{d}t' \mathbf{U}_{t'}\Delta'_{t'}\mathbf{U}^{\dagger}_{t'} \\ &\simeq \mathbf{U}_{t_n}\left(\int_{t_n}^{t_{n+1}} \mathrm{d}t' \left[(\mathbf{K}_{t'} - \mathbf{K}_{t_n}),\ \tilde{\mathbf{P}}^{(0)}_{t_{n+1}}\right]\right)\mathbf{U}^{\dagger}_{t_n}. \end{aligned} \tag{C.2}$$

The new density matrix is finally obtained through

$$\mathbf{P}_{t_{n+1}} = \tilde{\mathbf{P}}^{(0)}_{t_{n+1}} + \Delta\mathbf{P}_{t_{n+1}}. \tag{C.3}$$

Note that the change of the KS matrix $\mathbf{K}$ from t_n to t_{n+1} (due to the change of external field) is taken into account only in the drive step.

If the external field varies linearly during the time step, the "drive" correction done by Eq. (C.2) will be zero up to the first order in Δt. Then, the propagation of density matrix can be simply done by Eq. (C.1) with a slightly different propagator

$$\mathbf{P}_{t_{n+1}} \simeq \tilde{\mathbf{P}}^{(0)}_{t_{n+1}} = \exp(-i \cdot \Delta t \cdot \mathbf{K}_{t_n+\frac{\Delta t}{2}})\ \mathbf{P}_{t_n}\ \exp(i \cdot \Delta t \cdot \mathbf{K}_{t_n+\frac{\Delta t}{2}}). \tag{C.4}$$

Eq. (C.4) is equivalent to Eq. (4.2), *i.e.* the MMUT of density matrix.

To analyze the error of MMUT, one can first expand $\mathbf{P}_{t_{n+1}}$ around $\mathbf{P}_{t_n}$

$$\mathbf{P}_{t_{n+1}} = \sum_{m=0}^{\infty} \frac{1}{m!} \frac{\partial^m \mathbf{P}_{t_n}}{(\partial t)^m} (\Delta t)^m. \tag{C.5}$$

Then, applying Eq. (4.1) to Eq. (C.5) gives

$$\begin{aligned} \mathbf{P}_{t_{n+1}} &= \mathbf{P}_{t_n} - i\ [\mathbf{K}_{t_n}, \mathbf{P}_{t_n}]\,\Delta t - i\ \frac{1}{2}\left(\frac{\partial}{\partial t}[\mathbf{K}_{t_n}, \mathbf{P}_{t_n}]\right)(\Delta t)^2 - i\ \frac{1}{6}\left(\frac{\partial^2}{(\partial t)^2}[\mathbf{K}_{t_n}, \mathbf{P}_{t_n}]\right)(\Delta t)^3 + \cdots \\ &= \mathbf{P}_{t_n} - i\ [\mathbf{K}_{t_n}, \mathbf{P}_{t_n}]\,\Delta t - \frac{1}{2}[\mathbf{K}_{t_n}, [\mathbf{K}_{t_n}, \mathbf{P}_{t_n}]]\,(\Delta t)^2 - i\ \frac{1}{2}\left[\frac{\partial \mathbf{K}_{t_n}}{\partial t}, \mathbf{P}_{t_n}\right](\Delta t)^2 \\ &\quad - i\ \frac{1}{6}\left[\frac{\partial^2}{(\partial t)^2}\mathbf{K}_{t_n}, \mathbf{P}_{t_n}\right](\Delta t)^3 - \frac{1}{3}\left[\frac{\partial}{\partial t}\mathbf{K}_{t_n}, [\mathbf{K}_{t_n}, \mathbf{P}_{t_n}]\right](\Delta t)^3 \\ &\quad - \frac{1}{6}\left[\mathbf{K}_{t_n}, \left[\frac{\partial}{\partial t}\mathbf{K}_{t_n}, \mathbf{P}_{t_n}\right]\right](\Delta t)^3 + i\ \frac{1}{6}[\mathbf{K}_{t_n}, [\mathbf{K}_{t_n}, [\mathbf{K}_{t_n}, \mathbf{P}_{t_n}]]]\,(\Delta t)^3 + \cdots \end{aligned} \tag{C.6}$$

Note that Eq. (C.6) is the direct result of *Liouville-von Neumann* equation, and can be used as a reference for the error analysis of MMUT. For Eq. (C.4), switch to *Baker-Campbell-Hausdorff* expansion, which gives

$$\begin{aligned} \tilde{\mathbf{P}}_{t_{n+1}} &= \exp(-i \cdot \Delta t \cdot \mathbf{K}_{t_n+\frac{\Delta t}{2}})\ \mathbf{P}_{t_n}\ \exp(i \cdot \Delta t \cdot \mathbf{K}_{t_n+\frac{\Delta t}{2}}) \\ &= \mathbf{P}_{t_n} + \left[\mathbf{P}_{t_n}, i \cdot \Delta t \cdot \mathbf{K}_{t_n+\frac{\Delta t}{2}}\right] + \frac{1}{2}\left[\left[\mathbf{P}_{t_n}, i \cdot \Delta t \cdot \mathbf{K}_{t_n+\frac{\Delta t}{2}}\right], i \cdot \Delta t \cdot \mathbf{K}_{t_n+\frac{\Delta t}{2}}\right] \\ &\quad + \frac{1}{6}\left[\left[\left[\mathbf{P}_{t_n}, i \cdot \Delta t \cdot \mathbf{K}_{t_n+\frac{\Delta t}{2}}\right], i \cdot \Delta t \cdot \mathbf{K}_{t_n+\frac{\Delta t}{2}}\right], i \cdot \Delta t \cdot \mathbf{K}_{t_n+\frac{\Delta t}{2}}\right] + \cdots \\ &= \mathbf{P}_{t_n} - i\ \left[\mathbf{K}_{t_n+\frac{\Delta t}{2}}, \mathbf{P}_{t_n}\right]\Delta t - \frac{1}{2}\left[\mathbf{K}_{t_n+\frac{\Delta t}{2}}, \left[\mathbf{K}_{t_n+\frac{\Delta t}{2}}, \mathbf{P}_{t_n}\right]\right](\Delta t)^2 \\ &\quad + i\ \frac{1}{6}\left[\mathbf{K}_{t_n+\frac{\Delta t}{2}}, \left[\mathbf{K}_{t_n+\frac{\Delta t}{2}}, \left[\mathbf{K}_{t_n+\frac{\Delta t}{2}}, \mathbf{P}_{t_n}\right]\right]\right](\Delta t)^3 + \cdots . \end{aligned} \tag{C.7}$$

The $\mathbf{K}_{t_n+\frac{\Delta t}{2}}$ can be expanded around $\mathbf{K}_{t_n}$ via

$$\mathbf{K}_{t_n+\frac{\Delta t}{2}} = \sum_{m=0}^{\infty} \frac{1}{m!} \frac{\partial^m \mathbf{K}_{t_n}}{(\partial t)^m} (\frac{\Delta t}{2})^m. \tag{C.8}$$

Plugging Eq. (C.8) into Eq. (C.7) gives

$$\begin{aligned}\tilde{\mathbf{P}}_{t_{n+1}} = \mathbf{P}_{t_n} &- i\ \left[\mathbf{K}_{t_n}, \mathbf{P}_{t_n}\right] \Delta t - \frac{1}{2}\left[\mathbf{K}_{t_n}, \left[\mathbf{K}_{t_n}, \mathbf{P}_{t_n}\right]\right] (\Delta t)^2 - i\ \frac{1}{2}\left[\frac{\partial \mathbf{K}_{t_n}}{\partial t}, \mathbf{P}_{t_n}\right] (\Delta t)^2 \\ &- i\ \frac{1}{8}\left[\frac{\partial^2}{(\partial t)^2}\mathbf{K}_{t_n}, \mathbf{P}_{t_n}\right] (\Delta t)^3 - \frac{1}{4}\left[\frac{\partial}{\partial t}\mathbf{K}_{t_n}, \left[\mathbf{K}_{t_n}, \mathbf{P}_{t_n}\right]\right] (\Delta t)^3 \\ &- \frac{1}{4}\left[\mathbf{K}_{t_n}, \left[\frac{\partial}{\partial t}\mathbf{K}_{t_n}, \mathbf{P}_{t_n}\right]\right] (\Delta t)^3 + i\ \frac{1}{6}\left[\mathbf{K}_{t_n}, \left[\mathbf{K}_{t_n}, \left[\mathbf{K}_{t_n}, \mathbf{P}_{t_n}\right]\right]\right] (\Delta t)^3 + \cdots \end{aligned} \tag{C.9}$$

From Eq. (C.9) and Eq. (C.6), one can compute the local truncation error, τ^n, of MMUT propagation method,

$$\begin{aligned}\tau^n &= \frac{1}{\Delta t}\left(\mathbf{P}_{t_{n+1}} - \tilde{\mathbf{P}}_{t_{n+1}}\right) \\ &= -i\ \frac{1}{24}\left[\frac{\partial^2}{(\partial t)^2}\mathbf{K}_{t_n}, \mathbf{P}_{t_n}\right] (\Delta t)^2 - \frac{1}{12}\left[\frac{\partial}{\partial t}\mathbf{K}_{t_n}, \left[\mathbf{K}_{t_n}, \mathbf{P}_{t_n}\right]\right] (\Delta t)^2 \\ &\quad + \frac{1}{12}\left[\mathbf{K}_{t_n}, \left[\frac{\partial}{\partial t}\mathbf{K}_{t_n}, \mathbf{P}_{t_n}\right]\right] (\Delta t)^2 + O\left((\Delta t)^3\right). \end{aligned} \tag{C.10}$$

Thus, the local truncation error is $\mathcal{O}\left((\Delta t)^2\right)$, which means the MMUT propagation method is second order accurate.

Appendix D

THE IMPLEMENTATION OF CCSD AND EOM-CCSD IN GAUSSIAN

If CC with singles and doubles (CCSD) is considered, then the CC wave function is written as

$$|CCSD\rangle = e^{T_1+T_2}|0\rangle. \tag{D.1}$$

In Gaussian, the CCSD/EOM-CCSD and its low-scaling approximations are coded in **L913.F**. This section shows the subroutines used to compute CCSD/EOM-CCSD in **L913.F**. For CCSD, the energy and amplitudes equations can be written as

$$E^{CCSD} = \langle 0|H(1 + T_1 + \frac{1}{2}T_1^2 + T_2)|0\rangle, \tag{D.2}$$

$$\langle \mu_1|H(1 + T_1 + T_2 + \frac{1}{2}T_1^2 + T_1T_2 + \frac{1}{6}T_1^3)|0\rangle = 0, \tag{D.3}$$

$$\langle \mu_2|H(1 + T_1 + T_2 + \frac{1}{2}T_1^2 + T_1T_2 + \frac{1}{2}T_2^2 + \frac{1}{6}T_1^3 + \frac{1}{2}T_1^2T_2 + \frac{1}{24}T_1^4)|0\rangle = 0. \tag{D.4}$$

Its T_1 equation (using optimized HF orbitals) to get t_i^a is done in the following subroutines.

$$
\begin{aligned}
(\epsilon_i - \epsilon_a)t_i^a = & \sum_{j,b} \langle ib \| aj \rangle t_j^b && \textbf{in SS3.F} \\
& + \sum_{j,k,b,c} \langle jk \| bc \rangle t_k^c t_{ij}^{ab} && \textbf{in CCSDSS.F} \\
& - \sum_{j,k,b>c} \langle jk \| bc \rangle t_j^a t_{ik}^{bc} && \textbf{in UMP43.F} \\
& + \sum_{j,b>c} \langle aj \| bc \rangle (t_{ij}^{bc} + t_i^b t_j^c - t_i^c t_j^b) && \textbf{in SD4.F/DD1Drv.F} \\
& - \sum_{j>k,b} \langle jk \| ib \rangle (t_{jk}^{ab} + t_j^a t_k^b - t_j^b t_k^a) && \textbf{in SD5DS5.F} \\
& - \sum_{j>k,b,c} \langle jk \| bc \rangle t_i^b (t_{jk}^{ac} + t_j^a t_k^c - t_j^c t_k^a), && \textbf{in UMP42.F}
\end{aligned}
$$

The CCSD T_2 equation is done in the following subroutines.

$$
\begin{aligned}
(\epsilon_i + \epsilon_j - \epsilon_a - \epsilon_b)t_{ij}^{ab} = & \langle ij \| ab \rangle && \textbf{From IDB1-3} \\
& + P(ij) \sum_{c} \langle ab \| cj \rangle t_i^c && \textbf{in DS4.F} \\
& - P(ab) \sum_{k} \langle kb \| ij \rangle t_k^a && \textbf{in SD5DS5.F} \\
& - P(ij)P(ab) \sum_{k,c} \langle kb \| cj \rangle t_k^a t_i^c && \textbf{in CCDSS1.F} \\
& + P(ij)P(ab) \sum_{k,c} \langle kb \| cj \rangle t_{ik}^{ac} && \textbf{in DD3ZR.F} \\
& + \frac{1}{4} \sum_{k,l,c,d} \langle kl \| cd \rangle t_{ij}^{cd} t_{kl}^{ab} && \textbf{in UMP41.F(DD41R.F)} \\
& + \Bigg[P(ab) \sum_{k,c,d} \langle bk \| cd \rangle t_{ij}^{ac} t_k^d - \frac{1}{2} P(ab) \sum_{k,l,c,d} \langle kl \| cd \rangle t_{ij}^{ac} t_{kl}^{bd} && \\
& - P(ab) \sum_{k,l,c,d} \langle kl \| cd \rangle t_k^c t_l^a t_{ij}^{db} \Bigg] && \textbf{in UMP42.F} \\
& - \Bigg[\frac{1}{2} P(ij) \sum_{k,l,c,d} \langle kl \| cd \rangle t_{ik}^{ab} t_{jl}^{cd} + P(ij) \sum_{k,l,c,d} \langle kl \| cd \rangle t_k^c t_i^d t_{lj}^{ab} \Bigg] && \textbf{in UMP43.F}
\end{aligned}
$$

$$
\begin{aligned}
&+\left[\frac{1}{2}P(ij)P(ab)\sum_{k,l,c,d}\langle kl\|cd\rangle t_{ik}^{ac}t_{lj}^{db}+P(ij)P(ab)\sum_{k,l,c,d}\langle kl\|cd\rangle t_i^c t_{kj}^{ad}t_l^b\right.\\
&\left.+P(ij)P(ab)\sum_{k,c,d}\langle ak\|cd\rangle t_{kj}^{db}t_i^c-P(ij)P(ab)\sum_{k,l,c}\langle kl\|ic\rangle t_{lj}^{cb}t_k^a\right] \qquad \textbf{in UMP44.F and UMP4Ry}\\
&+\left[\sum_{c<d}\langle ab\|cd\rangle t_{ij}^{cd}+\frac{1}{2}P(ij)\sum_{c,d}\langle ab\|cd\rangle t_i^c t_j^d\right] \qquad \textbf{in DD1.F}\\
&-\left[\frac{1}{2}P(ab)\sum_{k,c,d}\langle ak\|cd\rangle t_{ij}^{cd}t_k^b+\frac{1}{2}P(ij)P(ab)\sum_{k,c,d}\langle ak\|cd\rangle t_i^c t_j^d t_k^b\right] \qquad \textbf{in SD5DS5.F}\\
&+\left[\sum_{k<l}\langle kl\|ij\rangle t_{kl}^{ab}+\frac{1}{2}P(ab)\sum_{k<l}\langle kl\|ij\rangle t_k^a t_l^b+\frac{1}{2}P(ij)\sum_{k,l,c}\langle kl\|ic\rangle t_{kl}^{ab}t_j^c\right.\\
&\quad+\frac{1}{2}P(ij)P(ab)\sum_{k,l,c}\langle kl\|ic\rangle t_k^a t_l^b t_j^c+\frac{1}{4}P(ij)\sum_{k,l,c,d}\langle kl\|cd\rangle t_i^c t_{kl}^{ab}t_j^b\\
&\quad\left.+\frac{1}{4}P(ab)\sum_{k,l,c,d}\langle kl\|cd\rangle t_k^a t_{ij}^{cd}t_l^b+\frac{1}{4}P(ij)P(ab)\sum_{k,l,c,d}\langle kl\|cd\rangle t_i^c t_k^a t_j^d t_l^b\right]. \qquad \textbf{in DD41R.F}
\end{aligned}
$$

For EOM-CCSD, the Jacobian is

$$
\mathbf{H}_{EOM-CCSD}=\begin{bmatrix}\bar{\mathbf{H}}^{SS} & \bar{\mathbf{H}}^{SD}\\ \bar{\mathbf{H}}^{DS} & \bar{\mathbf{H}}^{DD}\end{bmatrix}, \tag{D.5}
$$

in which,

$$\begin{aligned}
\bar{H}^{SS}_{ai} &= \langle \Phi^a_i | \hat{H}_N (1 + \hat{T}_1 + \hat{T}_2 + \frac{1}{2}\hat{T}_1^2) \hat{R}_1 | \Phi_0 \rangle \\
&= (\epsilon_a - \epsilon_i) r^a_i + \sum_{j,b} \langle aj \| ib \rangle r^b_j + \sum_{j,b,c} \langle aj \| bc \rangle (t^c_j r^b_i + t^b_i r^c_j) - \sum_{j,k,b} \langle jk \| ib \rangle (t^b_k r^a_j + t^a_j r^b_k) \\
&\quad - \frac{1}{2} \sum_{j,k,b,c} \langle jk \| bc \rangle t^{ac}_{jk} r^b_i - \frac{1}{2} \sum_{j,k,b,c} \langle jk \| bc \rangle t^{bc}_{ik} r^a_j + \sum_{j,k,b,c} \langle jk \| bc \rangle t^{ac}_{ik} r^b_j \\
&\quad - \sum_{j,k,b,c} \langle jk \| bc \rangle (t^b_i t^a_j r^c_k + t^b_i r^a_j t^c_k + r^b_i t^a_j t^c_k),
\end{aligned} \tag{D.6}$$

$$\begin{aligned}
\bar{H}^{SD}_{ai} &= \langle \Phi^a_i | \hat{H}_N (1 + \hat{T}_1) \hat{R}_2 | \Phi_0 \rangle \\
&= \frac{1}{2} \sum_{j,b,c} \langle aj \| bc \rangle r^{bc}_{ij} - \frac{1}{2} \sum_{j,k,b} \langle jk \| ib \rangle r^{ab}_{jk} \\
&\quad - \frac{1}{2} \sum_{j,k,b,c} \langle jk \| bc \rangle r^{ac}_{jk} t^b_i - \frac{1}{2} \sum_{j,k,b,c} \langle jk \| bc \rangle r^{bc}_{ik} t^a_j + \sum_{j,k,b,c} \langle jk \| bc \rangle r^{ac}_{ik} t^b_j,
\end{aligned} \tag{D.7}$$

$$\begin{aligned}
\bar{H}^{DS}_{abij} &= \langle \Phi^{ab}_{ij} | \hat{H}_N (1 + \hat{T}_1 + \hat{T}_2 + \frac{1}{2}\hat{T}_1^2 + \hat{T}_1 \hat{T}_2 + \frac{1}{6}\hat{T}_1^3) \hat{R}_1 | \Phi_0 \rangle \\
&= P(ij) \sum_{c} \langle ab \| cj \rangle r^c_i - P(ab) \sum_{k} \langle kb \| ij \rangle r^a_k + P(ij) \sum_{c,d} \langle ab \| cd \rangle r^c_i t^d_j + P(ab) \sum_{k,l} \langle kl \| ij \rangle r^a_k t^b_l \\
&\quad - P(ij)P(ab) \sum_{k,c} \langle kb \| cj \rangle (r^c_i t^a_k + t^c_i r^a_k) + P(ij)P(ab) \sum_{k,c} \langle ak \| cd \rangle r^c_i t^{db}_{kj} \\
&\quad - P(ij)P(ab) \sum_{k,l,c} \langle kl \| ic \rangle r^a_k t^{cb}_{lj} - \frac{1}{2} P(ab) \sum_{k,c,d} \langle ak \| cd \rangle r^b_k t^{cd}_{ij} + \frac{1}{2} P(ij) \sum_{k,l,c} \langle kl \| ic \rangle r^c_j t^{ab}_{kl} \\
&\quad + P(ab) \sum_{k,c,d} \langle bk \| cd \rangle r^d_k t^{ac}_{ij} - P(ij) \sum_{k,l,c} \langle kl \| jc \rangle r^c_l t^{ab}_{ik} - \frac{1}{2} P(ij)P(ab) \sum_{k,c,d} \langle kb \| cd \rangle r^a_k t^c_i t^d_j \\
&\quad + \frac{1}{2} P(ij)P(ab) \sum_{k,l,c} \langle kl \| ic \rangle r^c_j t^a_k t^b_l - P(ij)P(ab) \sum_{k,c,d} \langle kb \| cd \rangle r^c_i t^a_k t^d_j \\
&\quad + P(ij)P(ab) \sum_{k,l,c} \langle kl \| ic \rangle r^a_k t^c_j t^b_l + \frac{1}{2} P(ij) \sum_{k,l,c,d} \langle kl \| cd \rangle r^c_i t^d_j t^{ab}_{kl} + \frac{1}{2} P(ab) \sum_{k,l,c,d} \langle kl \| cd \rangle r^a_k t^b_l t^{cd}_{ij} \\
&\quad + P(ij)P(ab) \sum_{k,l,c,d} \langle kl \| cd \rangle r^c_i t^b_l t^{ad}_{kj} + P(ij)P(ab) \sum_{k,l,c,d} \langle kl \| cd \rangle r^b_l t^c_i t^{ad}_{kj} \\
&\quad - P(ij) \sum_{k,l,c,d} \langle kl \| cd \rangle (r^c_k t^d_i + r^d_i t^c_k) t^{ab}_{lj} - P(ab) \sum_{k,l,c,d} \langle kl \| cd \rangle (r^c_k t^a_l + r^a_l t^c_k) t^{db}_{ij} \\
&\quad + \frac{1}{2} P(ij)P(ab) \sum_{k,l,c,d} \langle kl \| cd \rangle (r^d_j t^b_l + r^b_l t^d_j) t^c_i t^a_k,
\end{aligned} \tag{D.8}$$

$$
\begin{aligned}
\bar{H}^{DD}_{abij} &= \langle \Phi^{ab}_{ij} | \hat{H}_N (1 + \hat{T}_1 + \hat{T}_2 + \frac{1}{2}\hat{T}_1^2)\hat{R}_2 | \Phi_0 \rangle \\
&= (\epsilon_a + \epsilon_b - \epsilon_i - \epsilon_j) r^{ab}_{ij} + \frac{1}{2}\sum_{c,d} \langle ab \| cd \rangle r^{cd}_{ij} + \frac{1}{2}\sum_{k,l} \langle kl \| ij \rangle r^{ab}_{kl} - P(ij)P(ab)\sum_{k,c} \langle kb \| cj \rangle r^{ca}_{ik} \\
&\quad + P(ij)P(ab)\sum_{k,c} \langle ak \| cd \rangle t^{c}_{i} r^{db}_{kj} - P(ij)P(ab)\sum_{k,l,c} \langle kl \| ic \rangle t^{a}_{k} r^{cb}_{lj} - \frac{1}{2}P(ab)\sum_{k,c,d} \langle ak \| cd \rangle t^{b}_{k} r^{cd}_{ij} \\
&\quad + \frac{1}{2}P(ij)\sum_{k,l,c} \langle kl \| ic \rangle t^{c}_{j} r^{ab}_{kl} + P(ab)\sum_{k,c,d} \langle bk \| cd \rangle t^{d}_{k} r^{ac}_{ij} - P(ij)\sum_{k,l,c} \langle kl \| jc \rangle t^{c}_{l} r^{ab}_{ik} \\
&\quad + \frac{1}{4}\sum_{k,l,c,d} \langle kl \| cd \rangle (r^{cd}_{ij} t^{ab}_{kl} + t^{cd}_{ij} r^{ab}_{kl}) + P(ij)P(ab)\sum_{k,l,c,d} \langle kl \| cd \rangle r^{ac}_{ik} t^{db}_{lj} \\
&\quad - \frac{1}{2}P(ij)\sum_{k,l,c,d} \langle kl \| cd \rangle (t^{ab}_{ik} r^{cd}_{jl} + r^{ab}_{ik} t^{cd}_{jl}) - \frac{1}{2}P(ab)\sum_{k,l,c,d} \langle kl \| cd \rangle (r^{bd}_{kl} t^{ac}_{ij} + t^{bd}_{kl} r^{ac}_{ij}) \\
&\quad + \frac{1}{4}P(ij)\sum_{k,l,c,d} \langle kl \| cd \rangle t^{c}_{i} t^{d}_{j} r^{ab}_{kl} + \frac{1}{4}P(ab)\sum_{k,l,c,d} \langle kl \| cd \rangle t^{a}_{k} t^{b}_{l} r^{cd}_{ij} + P(ij)P(ab)\sum_{k,l,c,d} \langle kl \| cd \rangle t^{c}_{i} t^{b}_{l} r^{ad}_{kj} \\
&\quad - P(ij)\sum_{k,l,c,d} \langle kl \| cd \rangle t^{d}_{i} t^{c}_{k} r^{ab}_{lj} - P(ab)\sum_{k,l,c,d} \langle kl \| cd \rangle t^{c}_{k} t^{a}_{l} r^{db}_{ij}.
\end{aligned}
\tag{D.9}
$$

The following shows the subroutines used to compute the above terms.

$$
\begin{aligned}
\bar{H}^{SS}_{ai} + \bar{H}^{SD}_{ai} = {} & (\epsilon_a - \epsilon_i) r_i^a && \textbf{EOMAB.F} \\
& + \sum_{j,b} \langle aj\|ib\rangle r_j^b + \sum_{j,b,c} \langle aj\|bc\rangle t_i^b r_j^c - \sum_{j,k,b} \langle jk\|ib\rangle t_j^a r_k^b + \sum_{j,k,b,c} \langle jk\|bc\rangle t_{ik}^{ac} r_j^b && \\
& - \sum_{j,k,b,c} \langle jk\|bc\rangle t_i^b t_j^a r_k^c && \textbf{ZDD3u.F} \\
& + \frac{1}{2} \sum_{j,b,c} \langle aj\|bc\rangle r_{ij}^{bc} && \textbf{SD4.F} \\
& + \sum_{j,b,c} \langle aj\|bc\rangle t_j^c r_i^b + \sum_{j,k,b} \langle jk\|ib\rangle t_k^b r_j^a - \frac{1}{2} \sum_{j,k,b,c} \langle jk\|bc\rangle t_{jk}^{ac} r_i^b - \frac{1}{2} \sum_{j,k,b,c} \langle jk\|bc\rangle t_{ik}^{bc} r_j^a && \\
& - \sum_{j,k,b,c} \langle jk\|bc\rangle t_i^b r_j^a t_k^c - \sum_{j,k,b,c} \langle jk\|bc\rangle r_i^b t_j^a t_k^c && \textbf{ZMP432.F} \\
& - \frac{1}{2} \sum_{j,k,b} \langle jk\|ib\rangle r_{jk}^{ab} && \textbf{ZSD5DS.F} \\
& - \frac{1}{2} \sum_{j,k,b,c} \langle jk\|bc\rangle r_{jk}^{ac} t_i^b && \textbf{RZMP42.F} \\
& - \frac{1}{2} \sum_{j,k,b,c} \langle jk\|bc\rangle r_{ik}^{bc} t_j^a && \textbf{RZMP43.F} \\
& + \sum_{j,k,b,c} \langle jk\|bc\rangle r_{ik}^{ac} t_j^b , && \textbf{ZSS3.F}
\end{aligned}
$$

and

$$
\begin{aligned}
&\bar{H}^{DS}_{abij} + \bar{H}^{DD}_{abij} \\
&\quad = (\epsilon_a + \epsilon_b - \epsilon_i - \epsilon_j) r^{ab}_{ij} && \textbf{EOMAB.F} \\
&\qquad + P(ij) \sum_{c,d} \langle ab \| cd \rangle r^c_i t^d_j && \textbf{DD1.F} \\
&\qquad - P(ij)P(ab) \sum_{k,c,d} \langle kb \| cd \rangle r^c_i t^a_k t^d_j && \textbf{ZiabcT.F} \\
&\qquad + \frac{1}{2} P(ij)P(ab) \sum_{k,l,c,d} \langle kl \| cd \rangle r^d_j t^b_l t^c_i t^a_k && \textbf{UZMP41.F} \\
&\qquad + P(ab) \sum_{k,l} \langle kl \| ij \rangle r^a_k t^b_l - \frac{1}{2} P(ij)P(ab) \sum_{k,c,d} \langle kb \| cd \rangle r^a_k t^c_i t^d_j + \frac{1}{2} P(ij)P(ab) \sum_{k,l,c,d} \langle kl \| cd \rangle r^b_l t^d_j t^c_i t^a_k \\
& && \textbf{ZDD2.F} \\
&\qquad + P(ij) \sum_{c} \langle ab \| cj \rangle r^c_i - P(ij)P(ab) \sum_{k,c} \langle kb \| cj \rangle r^c_i t^a_k + \frac{1}{2} P(ij)P(ab) \sum_{k,l,c} \langle kl \| ic \rangle r^c_j t^a_k t^b_l \\
& && \textbf{ZSD4.F} \\
&\qquad - P(ab) \sum_{k} \langle kb \| ij \rangle r^a_k - P(ij)P(ab) \sum_{k,c} \langle kb \| cj \rangle t^c_i r^a_k - \frac{1}{2} P(ij)P(ab) \sum_{k,c,d} \langle kb \| cd \rangle r^a_k t^c_i t^d_j . \\
& && \textbf{ZSD5DS.F}
\end{aligned}
$$

Appendix E

THE IMPLEMENTATION OF CC2 IN GAUSSIAN

The CC2 model is the second order approximation of CCSD,[48] whose amplitude equations are expressed as

$$\langle \mu_1 | e^{-\hat{T}_1-\hat{T}_2} H e^{\hat{T}_1+\hat{T}_2} | 0 \rangle = 0, \tag{E.1}$$

$$\langle \mu_2 | e^{-\hat{T}_1} H e^{\hat{T}_1} + [F, \hat{T}_2] | 0 \rangle = 0. \tag{E.2}$$

Here, H is defined as $H = F + U$, in which F is a one-electron operator, $F = \sum_P \epsilon_P a_P^\dagger a_P$, and U is a two-electron operator. Note that CC2 doesn't modify T_1 equation, but only T_2 equation. The elaborated CC2 T_2 equation to get t_{ij}^{ab} is

$$\begin{aligned}
(\epsilon_i + \epsilon_j - \epsilon_a - \epsilon_b) t_{ij}^{ab} = & \langle ij \| ab \rangle && \textbf{From IDB1-3} \\
& + P(ij) \sum_{c} \langle ab \| cj \rangle t_i^c && \textbf{in DS4.F} \\
& - P(ab) \sum_{k} \langle kb \| ij \rangle t_k^a && \textbf{in SD5DS5.F} \\
& - P(ij) P(ab) \sum_{k,c} \langle kb \| cj \rangle t_k^a t_i^c && \textbf{in CCDSS1.F} \\
& + \frac{1}{2} P(ij) \sum_{c,d} \langle ab \| cd \rangle t_i^c t_j^d && \textbf{in DD1.F} \\
& - \frac{1}{2} P(ij) P(ab) \sum_{k,c,d} \langle ak \| cd \rangle t_i^c t_j^d t_k^b && \textbf{in SD5DS5.F} \\
& + \left[\frac{1}{2} P(ab) \sum_{k<l} \langle kl \| ij \rangle t_k^a t_l^b + \frac{1}{2} P(ij) P(ab) \sum_{k,l,c} \langle kl \| ic \rangle t_k^a t_l^b t_j^c \right. \\
& \quad \left. + \frac{1}{4} P(ij) P(ab) \sum_{k,l,c,d} \langle kl \| cd \rangle t_i^c t_k^a t_j^d t_l^b \right]. && \textbf{in DD41R.F}
\end{aligned}$$

The difference between the EOM-CCSD Jacobian with the CC2 Jacobian comes from the double-single block and the double-double block.

$$\mathbf{H}_{EOM-CCSD} = \begin{bmatrix} \bar{\mathbf{H}}^{SS} & \bar{\mathbf{H}}^{SD} \\ \bar{\mathbf{H}}^{DS} & \bar{\mathbf{H}}^{DD} \end{bmatrix} \quad vs. \quad \mathbf{H}_{EOM-CC2} = \begin{bmatrix} \bar{\mathbf{H}}^{SS} & \bar{\mathbf{H}}^{SD} \\ \bar{\mathbf{H}}^{DS*} & \bar{\mathbf{H}}^{DD*} \end{bmatrix}$$

$$\begin{aligned}
\bar{H}^{DS}_{abij} &= \langle \Phi^{ab}_{ij} | \hat{H}_N (1 + \hat{T}_1 + \hat{T}_2 + \frac{1}{2}\hat{T}_1^2 + \hat{T}_1\hat{T}_2 + \frac{1}{6}\hat{T}_1^3)\hat{R}_1 | \Phi_0 \rangle \\
\bar{H}^{DD}_{abij} &= \langle \Phi^{ab}_{ij} | \hat{H}_N (1 + \hat{T}_1 + \hat{T}_2 + \frac{1}{2}\hat{T}_1^2)\hat{R}_2 | \Phi_0 \rangle \\
\Rightarrow \bar{H}^{DS*}_{abij} &= \langle \Phi^{ab}_{ij} | \hat{H}_N (1 + \hat{T}_1 + \frac{1}{2}\hat{T}_1^2 + \frac{1}{6}\hat{T}_1^3)\hat{R}_1 | \Phi_0 \rangle \\
\bar{H}^{DD*}_{abij} &= \langle \Phi^{ab}_{ij} | \hat{F}_N \hat{R}_2 | \Phi_0 \rangle
\end{aligned}$$

The following shows the subroutines used to compute $\bar{H}^{DS*}_{abij} + \bar{H}^{DD}_{abij}$.

$$\bar{H}^{DS*}_{abij} + \bar{H}^{DD}_{abij}$$

$$= (\epsilon_a + \epsilon_b - \epsilon_i - \epsilon_j) r^{ab}_{ij}$$

EOMAB.F

$$+ P(ij) \sum_{c,d} \langle ab \| cd \rangle r^c_i t^d_j$$

DD1.F

$$- P(ij)P(ab) \sum_{k,c,d} \langle kb \| cd \rangle r^c_i t^a_k t^d_j$$

ZiabcT.F

$$+ \frac{1}{2} P(ij)P(ab) \sum_{k,l,c,d} \langle kl \| cd \rangle r^d_j t^b_l t^c_i t^a_k$$

UZMP41.F

$$+ P(ab) \sum_{k,l} \langle kl \| ij \rangle r^a_k t^b_l - \frac{1}{2} P(ij)P(ab) \sum_{k,c,d} \langle kb \| cd \rangle r^a_k t^c_i t^d_j + \frac{1}{2} P(ij)P(ab) \sum_{k,l,c,d} \langle kl \| cd \rangle r^b_l t^d_j t^c_i t^a_k$$

ZDD2.F

$$+ P(ij) \sum_{c} \langle ab \| cj \rangle r^c_i - P(ij)P(ab) \sum_{k,c} \langle kb \| cj \rangle r^c_i t^a_k + \frac{1}{2} P(ij)P(ab) \sum_{k,l,c} \langle kl \| ic \rangle r^c_j t^a_k t^b_l$$

ZSD4.F

$$- P(ab) \sum_{k} \langle kb \| ij \rangle r^a_k - P(ij)P(ab) \sum_{k,c} \langle kb \| cj \rangle t^c_i r^a_k - \frac{1}{2} P(ij)P(ab) \sum_{k,c,d} \langle kb \| cd \rangle r^a_k t^c_i t^d_j$$

ZSD5DS.F

The benchmark test using both closed shell CC2 and open shell CC2 has been done for 18 molecules (see Fig. E.1) over 80 low-lying single excitations. The basis set used in the benchmark is TZVP basis set given the compromise between accuracy and cost. For all the molecules, the geometries have been optimized in the MP2/TZVP level. As can be seen, the CC2 excitation energies and corresponding oscillator strengths computed in this work agree pretty well with the previous reported values [187].

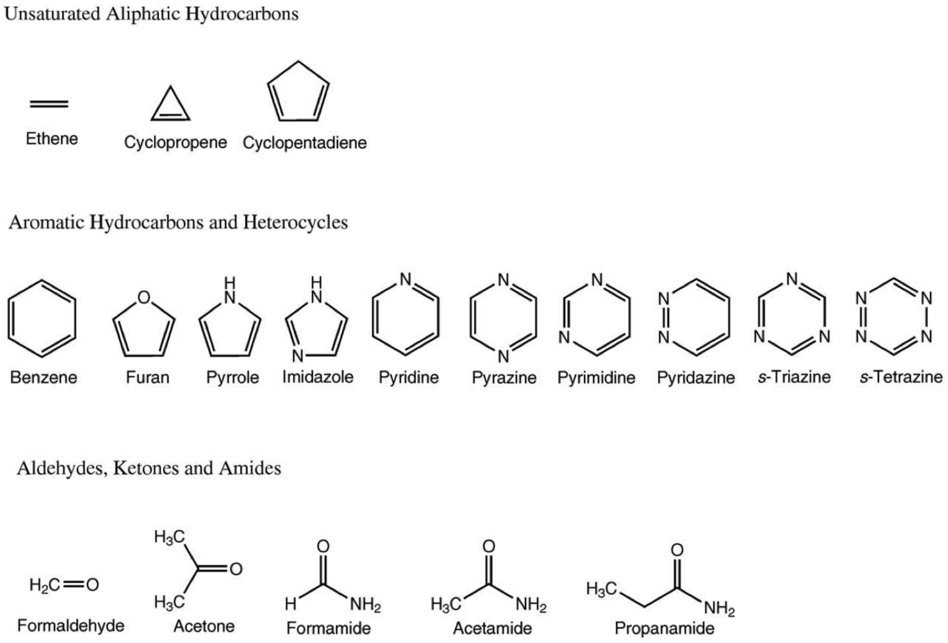

Figure E.1: Some organic molecules used for CC2 benchmark test.

Table E.1 shows the K-edge core excitation energies of some small molecules computed by energy specific CCSD (ES-CCSD) and its low-scaling approximations. As can be seen, as $\mathcal{O}(N^5)$ methods, CC2 significantly outperforms P-EOM-MBPT2 by 1∼3 eV for all the C, N, and O K-edge excitations studied in this test. Furthermore, CC2 can sometimes even outperforms CCSD as exemplified by the N K-edge excitation in NH_3 and all the O K-edge

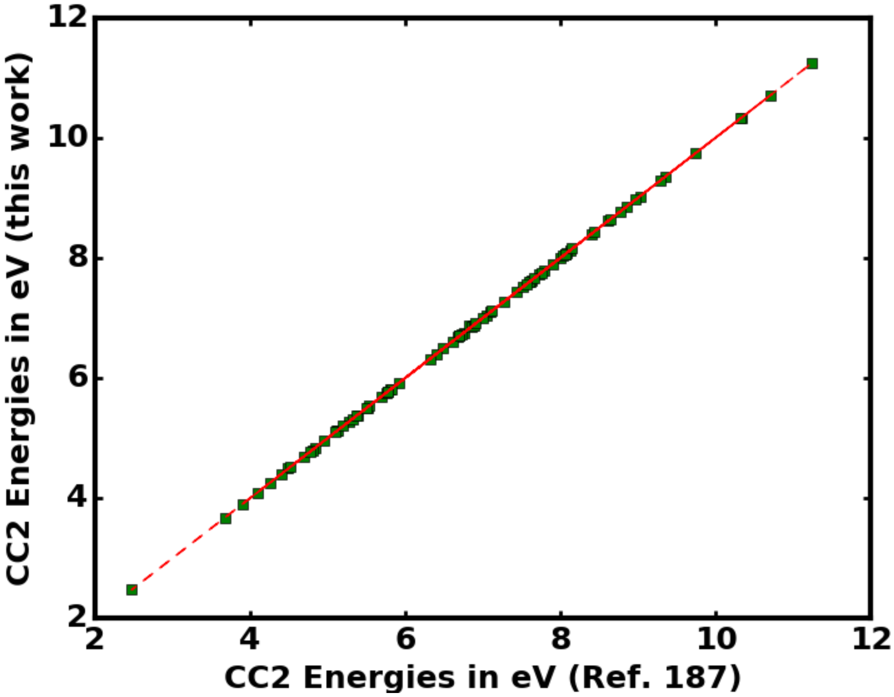

Figure E.2: CC2 vertical excitation energies computed in this implementation compared with literature values.

excitations studied in this test.

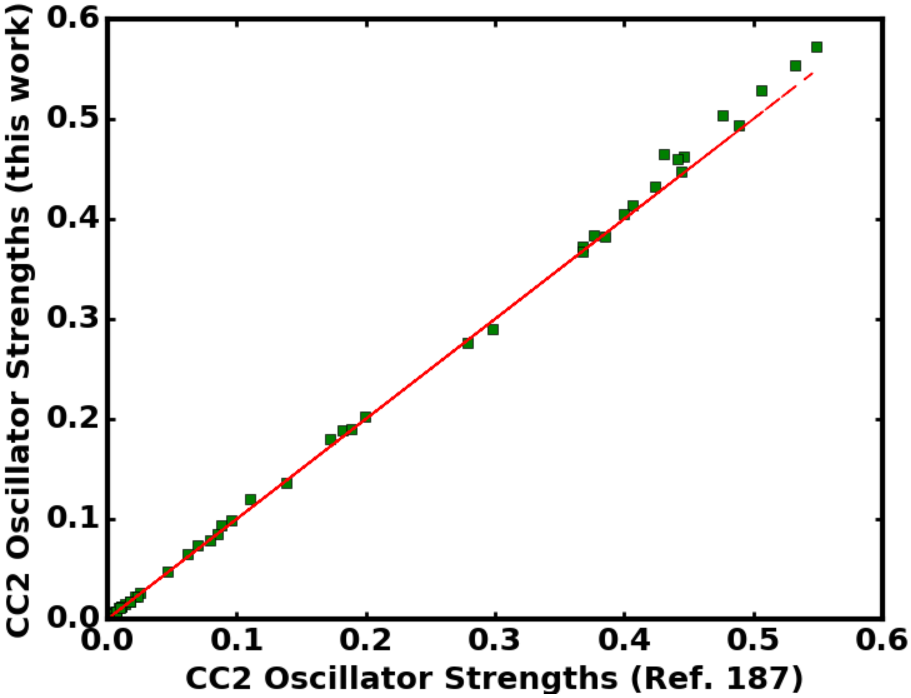

Figure E.3: CC2 dipole-allowed oscillator strengths computed in this implementation compared with literature values.

Table E.1: Calculated K-edge transition energies for some small molecules. The basis set used here is d-aug-cc-pCVDZ.

Molecules	Excitation		Calculated excitation (eV)				Experimental
	energy (eV)		ES-CC2	ES-P-EOM-MBPT2	ES-EOM-MBPT2	ES-EOM-CCSD	values (eV)
NH_3	N	1s → 3s	402.90	405.63	403.68	403.59	400.66 [185]
Formaldehyde	C	1s → π^*	289.52	290.83	288.54	288.21	285.59 [178]
	O	1s → π^*	534.03	536.59	534.47	534.43	530.82 [178]
CO	C	1s → 2pπ^*	290.57	291.81	289.88	289.46	287.40 [61]
	O	1s → π^*	536.76	539.71	537.74	537.70	534.21 [174]
N_2	N	1s → 2pπ_g	404.51	406.78	404.30	403.78	401.00 [193]
N_2O	N_T	1s → 3pπ^*	404.77	407.65	405.27	404.37	401.10 [1]
	N_C	1s → 3pπ^*	407.64	410.94	408.63	407.83	404.70 [1]
Ethene	C	1s → π^*	288.53	289.89	287.43	287.36	284.67 [216]
H_2O	O	1s → $4a_1$/3s	535.69	538.98	537.52	537.56	534.00 [185]